TESIS DE LA UNIVERSIDAD DE ZARAGOZA

2025 323

Juan Raúl Padrón Griffe

Modeling and Rendering of Multi-scale Materials

Director/es
Muñoz Orbañanos, Adolfo
Jarabo Torrijos, Adrián

ISSN 2254-7606

Prensas de la Universidad Universidad Zaragoza

Universidad de Zaragoza
Servicio de Publicaciones

ISSN 2254-7606

Universidad Zaragoza
1542

Tesis Doctoral

MODELING AND RENDERING OF MULTI-SCALE MATERIALS

Autor

Juan Raúl Padrón Griffe

Director/es

Muñoz Orbañanos, Adolfo
Jarabo Torrijos, Adrián

UNIVERSIDAD DE ZARAGOZA
Escuela de Doctorado

2025

Universidad Zaragoza
1542

Tesis Doctoral

Modeling and Rendering of Multi-scale Materials

Autor

Juan Raúl Padrón Griffe

Director/es

Dr. D. Adolfo Muñoz Orbañanos
Dr. D. Adrián Jarabo Torrijos

Facultad de Ingeniería y Arquitectura
Departamento de Ingeniería de Sistemas e Informática

2025

MODELING AND RENDERING OF MULTI-SCALE MATERIALS

JUAN RAUL PADRON GRIFFE

SUPERVISORS: Adolfo Muñoz, Adrián Jarabo

Tesis Doctoral - Ingeniería Informática
Departamento de Informática e Ingeniería de Sistemas
Escuela de Ingeniería y Arquitectura
Universidad de Zaragoza

Juan Raul Padron Griffe : *Modeling and Rendering of Multi-scale Materials*, Snake skin, cosmetic foundations and feathers, © January 2025

Dedicated to my parents, my siblings, my family and my friends

ABSTRACT

This dissertation explores the physically-based rendering of volumetric materials, focusing on the complex light interactions with their internal structures across multiple scales. Rendering such materials is inherently challenging due to the intricate interplay of absorption, scattering, interference, and diffraction, particularly in highly structured materials, potentially anisotropic and multilayered. Explicitly representing these multiscale structures and simulating full light transport is computationally intractable and impractical for computer graphics. Advancing the rendering of such materials accounting for their internal structure is important to enhance photorealism in virtual environments, which are becoming increasingly more prevalent in society. Moreover, multiscale modeling promises broader implications for predicting the appearance of complex materials in fields such as product development and manufacturing, material science and engineering, and biology, potentially reducing the need for costly and time-consuming physical experiments. To address some of the challenges, this dissertation introduces three specialized appearance models that balance realism and computational feasibility by statistically modeling chromatophores in reptile skin, cosmetic compounds, and hierarchical fiber structures in feathers.

The first contribution introduces a two-layer reflectance model for *snake skin* inspired by its unique anatomy and chromatophores. This model combines thin-film interference to simulate the reflective iridophores in the top layer with highly absorbing media in the bottom layer for the melanophores, effectively capturing both highly iridescent reflections and dark tones. The second contribution presents a multilayer reflectance model for *cosmetic foundations*. It characterizes the microscopic constituents of makeup with diffuse scatterers and specular platelets to replicate the glossy, matte, and velvety finishes observed in cosmetics. Lastly, the third contribution focuses on *feather appearance*, leveraging their hierarchical structure and intricate emerging light interactions. The approach implicitly models the individual fibers accounting for the ellipticity and multilayered cylindrical structure of barbs, along with a novel masking term for pennaceous feathers that analytically computes occlusions between barbs and barbules. Our reflectance models require no precomputation, and are able to reproduce the most prominent visual effects observed in reality, while being practical and expressive.

RESUMEN

Esta tesis explora el renderizado físico de materiales volumétricos, centrándose en las interacciones complejas de la luz con sus estructuras internas a múltiples escalas. La renderización de estos materiales presenta un desafío inherente debido a la intrincada combinación de absorción, dispersión, interferencia y difracción, especialmente en materiales altamente estructurados, potencialmente anisotrópicos y multicapas. Representar explícitamente estas estructuras multiescala y simular el transporte completo de la luz es computacionalmente inabordable e impráctico para los gráficos por ordenador. Avances en la representación de estos materiales considerando su estructura interna es fundamental para mejorar el fotorrealismo en entornos virtuales, que están adquiriendo cada vez mayor presencia en la sociedad. Además, el modelado multiescala promete tener implicaciones más amplias en la predicción de la apariencia de materiales complejos en campos como el desarrollo y la fabricación de productos, la ciencia e ingeniería de materiales y la biología, reduciendo potencialmente la necesidad de experimentos físicos costosos y que requieren mucho tiempo. Para abordar algunos de estos desafíos, esta disertación introduce tres modelos especializados de apariencia que mantienen el equilibrio entre el realismo y la viabilidad computacional mediante el modelado estadístico de cromatóforos en piel de reptiles, compuestos cosméticos y estructuras de fibras jerárquicas en plumas.

La primera contribución introduce un modelo de reflectancia de dos capas para *piel de serpientes*, que combina la interferencia de capa fina para simular los iridóforos reflectantes en la capa superior con un medio altamente absorbente en la capa inferior para los melanóforos. La segunda contribución presenta un modelo de reflectancia multicapa para *bases de maquillaje*, que caracteriza los componentes microscópicos del maquillaje mediante dispersores difusos y plaquetas especulares para replicar los acabados brillantes, mates y aterciopelados. Por último, la tercera contribución modela la apariencia de *plumas*, aprovechando su estructura jerárquica y sus complejas interacciones con la luz. El enfoque representa implícitamente las fibras individuales, considerando la elipticidad y la estructura cilíndrica multicapa de las barbas, junto con un nuevo término de enmascaramiento para las plumas pennáceas que calcula analíticamente las oclusiones entre barbas y bárbulas. Nuestros modelos de reflectancia no requieren precomputación y son capaces de reproducir los efectos visuales más prominentes observados en la realidad, manteniéndose prácticos y expresivos.

MEASURABLE CONTRIBUTIONS

This dissertation led to the following contributions (see Section 1.3 for more details):

- Two journal publications presented in international conferences [89, 121]
- One peer-reviewed conference paper [120]

Two research stays (four months in total) at the Denmark Technical University (DTU) hosted by Prof. Jeppe Revall Frisvad.

ACKNOWLEDGEMENTS

Every achievement in my professional career and life has rarely been possible alone. Many people have supported me throughout this journey, and I am deeply grateful to all of them. While I apologize that this acknowledgment cannot be exhaustive, I extend my heartfelt thanks to everyone who contributed to my PhD journey.

First and foremost, I would like to express my sincere gratitude to my advisors *Adolfo Muñoz* and *Adrian Jarabo* for their support, patience and guidance throughout my PhD. Thanks for sharing your knowledge and giving me the opportunity to dive into rendering and at the same time explore my interests and curiosity. Your dedication, mentorship, and constructive criticism has been invaluable in navigating the challenges of my research and in shaping me as both a researcher and a person.

I am also deeply thankful to the coauthors of my publications for their collaboration and hard work. *Dario Lanza*, your talent, knowledge and effort were instrumental to the success of our projects. Counting on someone who supports me and motivates me, especially in tight deadlines or when I ran out of energy, was crucial to overcome the challenges. *Alina Pranovich*, your enthusiasm and expertise in material capture greatly contributed to the success of the cosmetic research project.

My gratitude extends to the Visual Computing Group at DTU, particularly to my host *Jeppe Frisvad* for welcoming me and hosting me twice during my PhD. Thanks for sharing your knowledge and enthusiasm for rendering and optics. A special thanks to *Bojja Venu* for your kindness, support and shared excitement about multi-scale materials.

I would also like to acknowledge the members of the Graphics and Imaging Lab for their help during the tight deadlines, collaborative mindset, and insightful discussions. Special thanks to *Julia Guerrero-Viu*, *Pablo Luesia*, *Diego Royo*, *Edurne Bernal-Berdun*, *Daniel Subias* and *Néstor Monzón* for their support during difficult times and unforgettable memories. To *Belen Masia*, I am grateful for your knowledge, vision, and, above all, your generosity and willingness to help others. A special mention to *Mateo Vallejo*, *Maria Peña*, *Jorge Pina Colás*, *Óscar Pueyo Ciutad*, *Jorge García*, *Santiago Jimenez* and *Sergio Cartiel* for the good times and excitement you brought to every conversation. Thanks also to *Sandra Malpica*, *Daniel Martín*, *Ana Serrano* and *Julio*

Marco for your help, constructive feedback and positive attitude. Finally, my thanks *Mercedes Fatas* for your patience and assistance with administrative and personal matters and to *Diego Gutierrez* for inspiring a new generation of researchers and fostering a great research environment.

I am also grateful to the members of the PRIME ITN for the memorable experiences and stimulating discussions, both technical and non-technical. In particular, I would like to thank my fellow ESRs *Loïc Lachiver*, *Mohcen Hafidi*, *Henrik Philippi*, *Arthur Firmino*, *Misa Korac*, *Philippe Weier*, *Timotei Ardelean*, *Animesh Karnewar*, *Thomson TG*, *Wen Cao*, *Behnaz Ghafi* and *Emilie Nogue*. I would also like to thank *Eva Šauerová* and *Markéta Tomková* for their invaluable help with administrative and personal matters.

I want to thank the students I had the opportunity of supervising, *Diego Bielsa* and *Adam Bosak*. Thanks for the trust and hard work. I hope you have learned and had fun as much as I had with your research projects.

I am fortunate to have met many wonderful people in Zaragoza, including *Benedetta Fantaci*, *Elena Redaelli*, *Manuel Lagunas*, *Salvador Rodríguez*, *Quercus Hernández*, *David Morilla*, *Fernando Peña*, *Víctor Martínez* and *Inés Noguero*. Thank you for your company, support, and the good moments that made this journey even more special.

Finally, I want to express my deepest gratitude to my family for their unconditional love and endless encouragement. To my beloved parents, who have been my greatest role models and a constant source of inspiration. Thanks for teaching me the importance of perseverance and resilience. You have sparked my curiosity and nurtured my passion for learning. I am profoundly grateful for your wisdom, generosity, and unwavering support at every step of my life.

This dissertation would not have been possible without the generous funding from the European Union's Horizon 2020 research and innovation program under the Marie Skłodowska-Curie grant agreement No. 956585 (PRIME).

Part I

INTRODUCTION AND OVERVIEW

1 INTRODUCTION

Rendering has been a critical technology in a number of applications, including media production for movies and videogames, advertising and visualization, product design, cultural heritage, or emerging technologies such as augmented reality (AR) and virtual reality (VR). Figure 1.1 shows two remarkable examples of product visualization and visual effects.

Figure 1.1: Two examples of rendering applications: product visualization (IKEA catalogue) and high-fidelity visual effects (*Dawn of the Planet of the Apes, Weta Digital*).

The fundamental advances in photorealistic rendering in the last three decades were possible by taking into account the physical laws of ray optics, including accurate simulation of light transport and scattering models able to precisely predict the appearance from real objects. Today, Monte Carlo-based path tracing is the industry standard for light transport simulation in many worldwide known production offline renders [18, 24, 37, 45]. Path tracing as a rendering algorithm is not enough, and accurately modeling how light locally interacts with materials via physical processes like absorption and scattering is crucial to accurately depicting the real world.

Describing accurately the intensity and the distribution of the light interacting with specific materials is also essential for realistic rendering. This distribution of the light we observe at macro-scale is the result of the interaction of light with the microscopic details of the object surface or the interaction with microscopic particles inside volumes. The micro-scale irregularities of a given surface can drastically change the overall appearance from a perfect mirror when the surface is perfectly regular and the light distribution is mostly focused around one direction to a rough surface with an overall look more matte where the distribution of light is more uniform. The composition of the microscopic particles in a volume including their shape, orientation and correlation affect the light paths inside the volume

due to scattering and absorption of the particles, ultimately affecting its final appearance. Statistical models such as the Microfacet theory [11, 25] for surfaces or the Microflake theory [73] for volumes have been proven to be successful in abstracting the complexity at the microscopic scale, by stochastically modeling the structure and scattering of microscopic matter.

Complex materials have unique ways of interacting with light depending on their intricate micro-scale features, internal composition, and optical properties. These unique interactions cannot be accurately and efficiently represented by general reflectance models. For this reason, many reflectance models have been proposed for specific complex materials such as skin [3, 31, 70, 139], human hair [23, 103], textiles [2, 187, 188], wood [94, 104], leaves [5], or granular media [108, 113], to mention some of them. The light transport inside the internal multilayered structure beneath some materials in biological tissues such as human skin or plants, where light penetrates and escapes in a different position, gives these materials their characteristic organic and translucent appearance. Human hair, textiles, and wood are examples of materials made of fibers with different compositions and structures that lead to their distinct appearance. For example, the growth rings in wood cause noticeable anisotropic reflections, or the different arrangement and density of the twisted fibers in fabrics and the multiple scattering between them result in the intricate details that differentiate one kind of fabric from another. The size of the medulla inside the human hair and fur fibers is one of the main factors underlying the visual difference between them. Ultimately, achieving realism for complex materials confronts many challenges inherent to their particular structure and the behavior of the light transport interacting with them.

In this dissertation, we focus on three multi-scale materials with complex and fascinating appearances: reptile skin, cosmetics and feathers. The vivid colors of biological tissues such as scales and feathers are driven by its intricate structure at multiple scales, from the mesoscale to the nanoscale. Understanding the optical mechanisms and structures involved is fundamental for biologically-inspired appearance models.

1.1 STRUCTURAL COLORATION

For centuries, nature's beauty and complexity have captivated and fascinated humans (see Figure 1.2), sparking scientific discoveries and innovations. The colorful appearance of animals, plants, and minerals is fundamentally produced by two mechanisms or a combina-

tion of both: pigmentation and structural coloration. Pigments create color by absorbing and reflecting specific wavelengths of light, such as chlorophyll that absorbs red and blue, or eumelanin absorbing a broader range of visible light producing dark tones. In contrast, *structural coloration* arises from the scattering of light with microscopic and nanoscale structures, creating stunning and vibrant appearances. Ancient civilizations admired the iridescent colors in peacock feathers, beetles, and opals, but it was Robert Hooke in the 17th century who first linked the iridescent colors of peacock feathers to structural ridges rather than pigments, paving the way for seminal discoveries for foundational theories in optics, such as the Corpuscular theory of light (light made up of small particles) by Isaac Newton [115] and the wave theory of light by Thomas Young [182]. Advances in electron microscopy have later revealed the intricate structures behind the fascinating appearance of feathers, butterfly wings, and beetle exoskeletons, deepening our understanding of the optical phenomena and inspiring technological innovations. KolourOptik's anti-counterfeiting technology for banknotes and personal documents and Sparxell's eco-friendly cellulose-based structural colors in textiles, cosmetics, and paints, showcase some of the applications of multiscale structures in appearance.

Figure 1.2: Examples of biological tissues exhibiting structural coloration: feathers (left) and reptile scales (right). Feathers come in a variety of colors and shapes. Their stunning appearance arises partly from the scattering of light by their multiscale structure [62]. The rapid color change in a panther chameleon is achieved by actively tuning photonic nanocrystals within their scales [148].

Scattering plays a fundamental role in the appearance of objects and phenomena, influencing how light interacts with biological and synthetic materials. The way light is scattered depends on whether the underlying structures are organized or disorganized. Organized structures, such as thin films, diffraction gratings, and photonic crystals, create directional scattering effects that often result in iridescence. Thin films generate iridescent colors through wave interference, as seen in the highly iridescent green and gold colors of Chrysochroa beetles caused by a multi-layered stack of up to 120 layers. The vivid

blue colors of the Morpho butterflies [85] come from light interference with shelf-like chitin layers with irregular ridge heights acting as a diffraction grating. Pigments below these tree-like structures absorb the remaining colors, intensifying the blue color. Photonic crystals are periodic structures that selectively scatter specific wavelengths based on their lattice spacing. This effect contributes to vivid colors in nature, such as the bright hues of peacock feathers caused by a 2D lattice of melanin rods inside the barbules and the dynamic color shifts in panther chameleons [148] driven by the compression or expansion of cubic guanine nanocrystal lattices in their dermal chromatophores. In contrast, disordered or quasi-ordered structures scatter light evenly, producing non-iridescent colors that remain consistent regardless of the observer's perspective. A notable example is the spongy keratin-air matrix inside feather barbs, which predominantly scatters blue light to create the characteristic hues of blue birds [118]. Similar scattering mechanisms are also relevant in synthetic materials, such as cosmetics and coatings, where the shape, size, and distribution of the particles influence the appearance. The balance between scattering and absorption determines whether a material appears matte, glossy, or translucent.

In this dissertation, we examine the role of multi-scale structures in optical effects for three complex materials. In Chapter 3, we study the striking iridescent patterns in snakes due to their particular anatomical structure and approximate them with a thin-film structure. In Chapter 4, we develop a reflectance model that accounts for the shape and optical properties of the key constituents in cosmetic foundations. Finally, Chapter 5, we propose an appearance model that combines pigmentation with noniridescent structural effects produced by the spongy structure made of keratin and air inside the feather barbs.

1.2 GOAL AND OVERVIEW

The aim of this dissertation is to take a small step to fill the existing gap between the current reflectance models in computer graphics and the complex light scattering mechanisms found in organic materials such as biological tissues (human skin, scales, feathers) and human-made materials like makeup. The fundamental question is how the research and insights from other fields like biology and material science could be explored and exploited to push the state of the art of photorealistic image synthesis trying to keep at the same time the rendering algorithms and reflectance models as practical as possible. The key idea is carefully considering the multi-scale structure of these materials and proposing practical representations for efficient light transport simulation. In cosmetics and reptile scales, the challenge is

how to represent in an accurate and practical manner the scatterers inside them and how to incorporate them in a layered material framework to reproduce their particulate appearance effects. For feathers, the challenge is not only the modeling of the individual fibers with different optical properties but also the aggregated behavior of the multi-scale structure. In Figure 1.3 we show results created by our reflectance models.

Figure 1.3: Rendering examples for the three reflectance models proposed in this work: snake skin (Chapter 3), cosmetic foundations (Chapter 4) and feathers (Chapter 5).

Overview This dissertation is divided into two parts. The first part introduces the fundamental concepts, equations and techniques behind the rendering of surfaces and volumes with special emphasis on fibers and layered structures. The second part presents the reflectance models that we propose for snake skin, cosmetic foundations and pennaceous feathers. In Chapter 3, we propose a multilayered appearance model based on the particular anatomy of a snake skin and the particular light scattering effects behind the dark appearance and highly iridescent scales caused by the melanophores and iridophores inside the skin respectively. In Chapter 4, we introduce a multi-layered reflectance model for foundation cosmetics where each individual cosmetics layered is represented as a stochastic participating medium composed of the microscopic particulates such as diffuse scatteres and platelets commonly found in cosmetic foundations responsible for the appearance variation from matte finish to glossy looks depending on the specific configuration. Finally, Chapter 5 presents a far field reflectance model for pennaceous feathers that takes into account the hierarchical structure of a feather and the view-dependent aggregation behaviour of its biological components with an analytical masking term specially designed to take advantage of the regular structure of pennaceous feathers. In addition, we propose a reflectance model for the individual feather fibers that represent the anatomical structure more accurate and allow the model to represent different coloration mechanisms including pigmentation and diffuse structural coloration.

I am the first author of two of the three research projects discussed in this dissertation. These projects have been developed in collaboration with other colleagues and for this reason, I will write at the beginning of each chapter which are my specific contributions to the corresponding projects.

1.3 CONTRIBUTIONS AND MEASURABLE RESULTS

In this section, we summarize the research experience and outcomes of the dissertation in terms of publications, presentation in conferences, secondments and supervision.

1.3.1 *Publications*

All of the research projects presented in this dissertation have been published as papers in the Computer Graphics Forum journal, two international conferences (EGSR 2024, Pacific Graphics 2024) and a Spanish conference (CEIG 2023).

- A Biologically-Inspired Appearance Model for Snake Skin (Chapter 3)
  - Authors: **Juan Raúl Padrón-Griffe**, Diego Bielsa, Adrian Jarabo and Adolfo Muñoz.
  - Presentation at the Congreso Español de Informática Gráfica (CEIG 2023) of 2023 in Mallorca (Spain).
- A Practical Appearance Model for Cosmetic Foundations (Chapter 4)
  - Authors: Dario Lanza, **Juan Raúl Padrón-Griffe**, Alina Pranovich, Adolfo Muñoz, Jeppe Revall Frisvad and Adrian Jarabo.
  - Publication in the Computer Graphics Forum. This journal has an impact factor of 2.7 and its position in the JCR index is 44th out of (Q2) in the category of Computer Science, Software Engineering (data from 2023).
  - Presentation by Dario Lanza at the Eurographics Symposium on Rendering (EGSR) of 2024 in London (United Kingdom).
- A Surface-based Appearance Model for Pennaceous Feathers (Chapter 5)
  - Authors: **Juan Raúl Padrón-Griffe**, Dario Lanza, Adrian Jarabo and Adolfo Muñoz.
  - Publication in the Computer Graphics Forum. This journal has an impact factor of 2.7 and its position in the JCR index

is 44th out of (Q2) in the category of Computer Science, Software Engineering (data from 2023).

- Presentation at the 32th Pacific Conference on Computer Graphics and Applications (Pacific Graphics 2024) in Huangschan (China).
- Paper was presented as a poster before publication at SIGGRAPH 2024 in Denver (United States).

1.3.2 *Research Visits*

During my PhD I had the pleasure to carry out two research projects in collaboration with other researchers at the Technical University of Denmark:

- March 2024 - April 2024: Visiting student at the Visual Computing section, Technical University of Denmark. Host: Prof. Dr. Jeppe Revall Frisvad. The research visit leads to the supervision of Adam Bosák's master thesis on reconstruction of microstructures.
- June 2022 - July 2022: Visiting student at the Visual Computing section, Technical University of Denmark. Host: Prof. Dr. Jeppe Revall Frisvad. Our research project on an appearance model for foundation cosmetics started with this research visit.

1.3.3 *Supervision*

I was also lucky to supervise one Bachelor thesis and one Master thesis during my PhD studies:

- 2024: Adam Bosák. *Learning Procedural 3D Representation of Material Microgeometry*. Co-supervised with Prof. Dr. Jeppe Revall Frisvad and Bojja Venu.
- 2022: Diego Bielsa. *A Physically-based Appearance Model for Reptile Skin*. Co-supervised with Prof. Dr. Adolfo Muñoz and Adrian Jarabo.

2 BACKGROUND

In this chapter, we introduce the key concepts and theory that serve as a foundation for the reflectance models we propose in Part II of the thesis. First, we briefly introduce the optical models and radiometric quantities. Next, we discuss the basis for surface reflection and volumetric materials. Finally, we describe how Monte Carlo integration can be used to solve the light transport equations. For a comprehensive overview of rendering and its fundamental components, we refer the reader to other sources [125].

2.1 OPTICAL MODELS

Understanding and modeling light in nature depend on the scale of interaction, the required level of accuracy, and the specific phenomena under consideration. *Ray optics* or *geometric optics* provides the simplest and most widely used model in computer graphics, representing the propagation of light as rays. *Electromagnetic optics*, the most sophisticated classical optics model, describes light as an electromagnetic wave, capturing critical effects such as diffraction or interference when interactions involve matter on scales comparable to the wavelength of light. *Quantum optics*, the most comprehensive and complex optical model, quantizes light into photons, oscillating quanta of energy that interact with molecules and atoms. In Figure 2.1, we show some visual phenomena explained by these optical models.

Figure 2.1: Increasingly complex visual phenomena from ray optics to quantum optics. The Fresnel effect on a lake (left), where strong refractions are most noticeable near the observer's viewpoint due to the steep angle of incidence, while strong reflections dominate at greater distances where the incident angle is shallower. Vivid, shifting colors in a soap bubble (center) caused by wave interference. The radiation of a Willemite (right), appearing as a bright and prolonged green phosphorescence.

Ray optics represent light as rays and ignore its wave and particle nature. This approximation is accurate for modeling light interactions with objects that are significantly larger than its visible wavelength range (380–700 nanometers). Ray optics can predict some of the most common optical phenomena such as reflection, refraction, absorption, scattering, or emission that explain the appearance of most of the materials and phenomena that we observe regularly in our lives accurate enough for rendering. Reflection and refraction occur at surface interfaces, governed by principles like Snell's law and Fresnel equations, which explain the behavior of mirrors or the distortion of a pen in a glass of water. Absorption and scattering take place in a volume of particles, described by the Beer-Lambert law for the attenuation of a homogeneous medium and characterized by the absorption and scattering coefficients, explaining the color of human hair by the absorption of pigments like eumelanin and pheomelanin, or the color of the sky by the scattering of small particles like water droplets or dust. In Sections 2.3 and 2.4, we introduce the rendering and volume rendering equations that provide the mathematical foundation to describe the interaction of light with surfaces and volumes respectively.

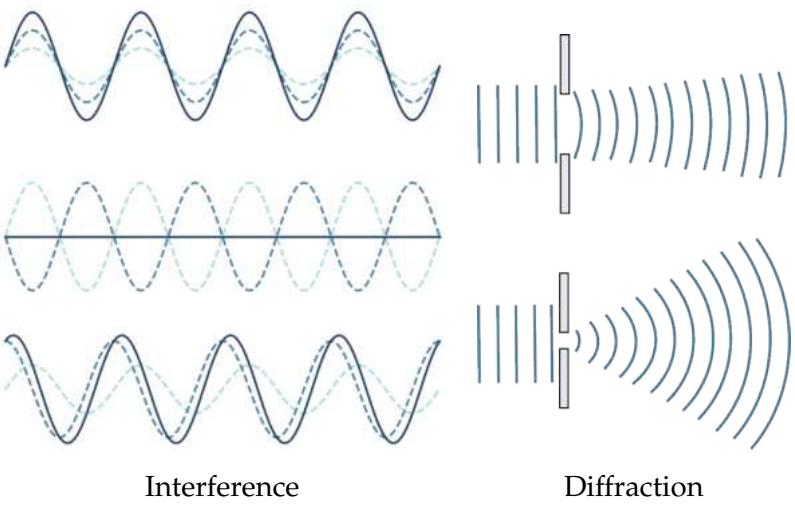

Figure 2.2: Interference examples between two waves (dashed lines) producing a resulting wave illustrated with a solid line. The first two cases illustrate pure constructive (top) and destructive (middle) interference, occurring when the incoming waves are completely in phase or out of phase respectively. The general case (bottom) shows a mix of both types of interference. The second illustration demonstrates diffraction through a single aperture. A wide aperture (top) results in minimal diffraction, while a narrow aperture (bottom) causes significant diffraction.

In *electromagnetic optics*, light is represented as an electromagnetic wave that travels in space in the form of two vector fields (electric field and magnetic field) mutually perpendicular and perpendicular

to the direction of the wave propagation. The propagation of the electric and magnetic fields is governed by Maxwell's equations. Representing light as an electromagnetic wave accounts for the same effects as ray optics, but it can additionally explain phenomena such as interference, diffraction, or polarization. *Interference* occurs when light waves combine into a single wave according to the superposition principle (see Figure 2.2, left), where constructive interference increases the wave amplitude when the waves are in phase, while destructive interference reduces the amplitude when the waves are out of phase. This phenomenon sometimes creates colorful patterns in thin films, like soap bubbles or oil slicks, due to phase differences from multiple reflections within the film. *Diffraction* (see Figure 2.2, right), a phenomenon explained by the Huygens-Fresnel principle stating that each point on a wavefront is a source of secondary spherical wavelets, describes light bending around obstacles or interacting with periodic structures, such as diffraction gratings that separate light into colors based on periodic spacing and the incident wave. Common examples of diffraction are the rainbow patterns on CDs/DVDs caused by light diffraction from their grooves and some spectrometers using diffraction gratings as dispersive elements to measure the spectra of materials. Rough surface reflection models based on wave optics can be approximated by using the Beckmann-Kirchoff [11] and Harvey-Shack theories [55, 87].

Quantum optics not only explains all the phenomena from classical optics mentioned above but also uniquely explains phenomena such as black-body radiation, fluorescence, or phosphorescence. *Black-body radiation* is the thermal radiation emitted by an idealized opaque object that absorbs all incoming light and re-emits energy based purely on its temperature computed by the Planck's law. In practice, the thermal radiation of nonperfect black bodies common in our daily lives, such as the glow of a red-hot stove or the Sun, can be approximated more accurately by Kirchhoff's law. *Fluorescence* occurs when a substance absorbs light and re-emits it almost instantly, while *phosphorescence* involves delayed re-emission. Fluorescent examples can be found in UV-reactive substances such as scorpion exoskeletons, parrot feathers, and Willemite minerals. Phosphorescence, in contrast, is typically observed in synthetic materials like glow-in-the-dark paints and emergency signs.

In this dissertation, we do not consider quantum optics effects, and we focus on ray optics and specific wave optics effects, such as thin-film interference, incorporated into our reflectance model for snake skin (Chapter 3) by modifying the Fresnel term. Nevertheless, interesting related effects such as phosphorescence and fluorescence are

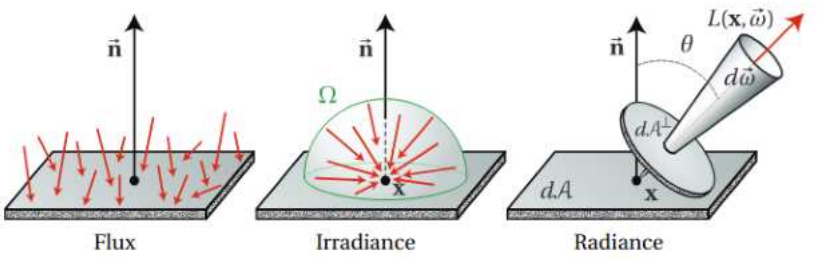

Figure 2.3: Common radiometric quantities used in computer graphics: flux, irradiance and radiance. Flux quantifies the total amount of light reaching a surface from all directions over a finite area. Irradiance represents the total light incident at a single point, integrated over the entire hemisphere. Radiance, on the other hand, measures the light arriving at a single point from a specific differential solid angle. Image source Jarosz's PhD thesis [78].

prevalent in nature, including fluorescent feathers and reptile skin.

2.2 RADIOMETRY

Radiometry is a mathematical tool to measure electromagnetic radiation, including visible light. Radiance is the basic quantity that determines how much light hits the final pixels in a synthetic image. In this section, we introduce the basic radiometric quantities (radiant flux, irradiance and radiance) fundamental for rendering algorithms. In Table 2.1, we list the radiometric quantities, their symbols, and units.

Radiant Flux, also know as radiant power,is the total amount of energy flowing at a surface per unit time. For this quantity Φ we can measure the infinitesimal change of light at an instant time under the steady-state assumption, i.e., energy does not change over time, as follows:

$$\Phi = \frac{dQ}{dt}\left[\frac{J}{s}\right]. \tag{2.1}$$

Its units shown inside the brackets are J/s or Watts (W). All the basic quantities introduced in this section represent different ways of measuring how many photons arrive or leave a region of space. The amount of energy carried by a photon oscillating with a wavelength λ is:

$$Q = \frac{hc}{\lambda}, \tag{2.2}$$

where c and h are the speed of light and Planck's constant respectively.

Quantity	Symbol	Units
Flux	Φ	W
Irradiance	E	$W \cdot m^{-2}$
Radiance	L	$W \cdot m^{-2} \cdot sr^{-1}$

Table 2.1: Fundamental radiometric quantities with their associated symbols and units. W denotes Watts and sr steradians.

Irradiance is the amount of radiant flux arriving at a surface per unit area. The irradiance denoted by E, also known as radiant flux density, can be computed using the following formula:

$$E = \frac{d\Phi}{dA}\left[\frac{W}{m^2}\right], \tag{2.3}$$

where dA is the infinitesimal differential area of the incident radiant flux. Irradiance is a surface property and it is measured in W/m^2.

Radiance is the radiant flux per unit area per unit solid angle. The solid angle, measured in *steradians* sr is an extension of the two dimensional angle concept on a plane to three dimensional angle on a sphere. A solid basically measures how large is the field of view of some particular point with respect to the center of a sphere. The radiance L is computed with the following formula:

$$L = \frac{d^2\Phi}{d\omega dA^{\perp}}\left[\frac{W}{m^2 sr}\right], \tag{2.4}$$

where $dA^{\perp}$ denotes the projection of the infinitesimal surface dA over the differential solid angle $d\omega$. Radiant flux and irradiance can be computed in terms of integrals of radiance over areas and directions respectively. In the next section, we formally discuss the interaction of light with surfaces.

2.3 LIGHT TRANSPORT IN SURFACES

The Rendering Equation (RE) together with the *Bidirectional Scattering Distribution Function* (BSDF) form the mathematical foundations for the simulation of light transport in a scene composed of surfaces under ray optics approximation.

2.3.1 *Rendering equation*

Jim Kayiya [82] introduced the rendering equation, also known as the light transport equation (LTE), to describe the radiance equilibrium at a single surface point on a surface as the combination of the radiance emitted and the light reflected or transmitted from other

surfaces. This equilibrium can be mathematically described as an integral equation over all incoming light directions:

$$L_o(\mathbf{x}, \omega_o) = L_e(\mathbf{x}, \omega_o) + \int_\Omega f(\mathbf{x}, \omega_i, \omega_o) L_i(\mathbf{x}, \omega_i) |\mathbf{n} \cdot \omega_i| d\omega_i. \quad (2.5)$$

$L_o(\mathbf{x}, \omega_o)$ is the outgoing radiance or the amount of light reaching the camera or viewer's eye. $f_r(\mathbf{x}, \omega_i, \omega_o)$ and $L_i(\mathbf{x}, \omega_i)$ are the BSDF and incoming radiance respectively. $L_e(\mathbf{x}, \omega_o)$ is the emitted radiance from a light source such as a light bulb or any glowing material. The cosine term $\mathbf{n} \cdot \omega_i$ accounts for the shortening following the Lambert's cosine law. As the incident angle increases, the amount of projected area of light on the surface becomes smaller.

2.3.2 *Surface Interaction*

A BSDF abstracts the local interaction of light with a surface, representing the amount and directional distribution of scattered light based on the surface's composition and internal volumetric structure. Formally, the BSDF is a 4D function over the incident and outgoing directions that describes how much incident light along ω_i (unit sphere) is scattered (reflected and transmitted) in the direction ω_o at an incident point x:

$$f(x, \omega_i, \omega_o) = \frac{dL_o(x, \omega_o)}{dE(x, \omega_i)} = \frac{dL_o(x, \omega_o)}{L_i(x, \omega_i)|\cos(\theta_i)|d\omega_i}, \quad (2.6)$$

A physically-based BSDF is measured in inverse steradians sr^{-1} and has the following properties:

- **Reciprocity (Helmholtz's Law of Reciprocity)**: For all pairs of incident and outgoing directions, the phase function satisfies:

$$f(x, \omega_i, \omega_o) = f(x, \omega_o, \omega_i) \quad (2.7)$$

- **Energy Conservation (Normalization)**: For all incident directions ω_i, the phase function must satisfy the following integral:

$$\int_\Omega f(x, \omega_i, \omega_o)\, n \cdot \omega_o \leqslant 1 \quad (2.8)$$

In computer graphics, the reciprocity property has been important for global illumination algorithms that reverse the light paths like classic light path tracing algorithms. The energy conservation property states that the total amount of energy reflected at a particular surface point should be less than or equal to the incident energy arriving at that point, i.e., the BSDF cannot scatter more light than it receives. A BSDF is a function that combines both the reflectance

and transmittance properties of a surface in a single function, individually described by a *Bidirectional Reflectance Distribution Function* (BRDF) and *Bidirectional Transmission Distribution Function* (BTDF) respectively. In this dissertation, we model the BSDF for three materials based on their unique structures such as cromatophores in snake skin (Chapter 3), the constituents of cosmetic foundations (Chapter 4) and the hierarchical fibers in feathers (Chapter 5).

2.4 LIGHT TRANSPORT IN VOLUMES

We have described so far how the interaction of the light with surfaces in a vacuum can be formalized with the rendering equation and solved with an algorithm like Monte Carlo-based path tracing. In many scenarios in real life, the space between surfaces is not empty, but it is filled with many small particles that participate in the light transport process by absorbing, scattering and emitting light. This host medium with many particles is known as a participating medium in computer graphics and can accurately represent appearance such as gaseous phenomena (fog, smoke, cloud, godrays), colorful liquids (milk and wine) and subsurface scattering for solid translucent materials like soap, human skin or jade. For instance, a cloud with a particular shape like a bunny can be rendered with a volumetric media as the example shown in Figure 2.4.

Figure 2.4: Volumetric media version of the Stanford Bunny model with a cloud-like appearance. Source: PBRT version 4 scenes [125].

In this section, we focus on the foundations behind light transport simulation in participating medium. We start with the phase function and its properties, which play an analogous role to the BSDF in the rendering equation for volumes. Next, we introduce the vol-

ume rendering equation, which is the equation that must be solved in order to render images with volumes. Finally, we briefly mention some of the light transport algorithms to solve the volume rendering equation.

2.4.1 *Radiative Transfer Equation*

Unlike rendering surfaces, where light bounces off opaque surfaces, the light transport simulation in participating medium requires accounting for additional interactions such as scattering, absorption, and emission of light by the particles within the volume illustrated in Figure 2.5. The *Radiative Transfer Equation* (RTE) [20] considers these interactions and describes the distribution of radiance in a participating medium for a point x and outgoing direction ω_o:

$$\begin{aligned} \omega_o \nabla L(x, \omega_o) &= -\sigma_a L(x, \omega_o) - \sigma_s L(x, \omega_o) + S(x, \omega_o) + Q(x, \omega_o), \\ S(x, \omega_o) &= \sigma_s \int_\Omega f_p(x, \omega_i, \omega_o) L(x, \omega_i) d\omega_i, \\ Q(x, \omega_o) &= \sigma_a L_e(x, w). \end{aligned} \tag{2.9}$$

The first two terms describe the fraction of the incoming radiance along the direction ω_o that is absorbed and scattered out specified by the absorption σ_a and scattering coefficients σ_s respectively. The in-scattering term $S(x, \omega_o)$ accounts for the radiance arriving at the point (increase in radiance) from the scattering of light from particles from other directions. Finally, the emission term $Q(x, \omega_o)$ represents the increase in radiance due to the emission from luminous particles.

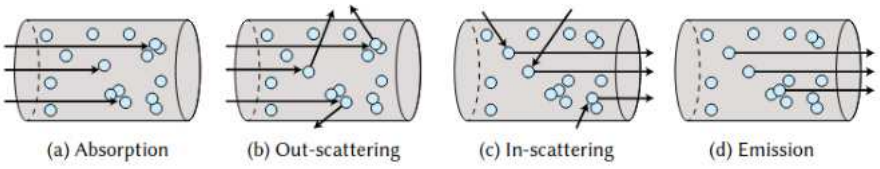

Figure 2.5: A light ray interacting with a participating medium can involve four fundamental physical processes. The particles inside the medium can absorb (a) or emit (d) light. Out-scattering (b) results in a loss of radiance as light is scattered away from its original direction, while in-scattering (c) increases radiance as light is redirected into the current path. Image source Vicini's PhD dissertation [157].

The phase function $f_p(x, \omega_i, \omega_o)$ is the volumetric analogous of a BSDF for a participating medium. This function describes the angular distribution of light scattering at a given point x in a volume and play an essential role in the in-scattered radiance process in volume ren-

dering. Similar to BSDFs, phase functions have two important physical properties: reciprocity and normalization. Phase functions respect the Helmholtz's law of reciprocity (see Equation 2.7) meaning the incident and outgoing directions can be interchange without affecting the final scattering distribution. In addition, they must also adhere to the energy conservation law meaning phase functions always must integrate to exactly one when the integration domain is the sphere of directions:

$$\int_{S_2} f_p(x, \omega_i, \omega_o)\, d\omega_o = 1. \tag{2.10}$$

In Computer Graphics, the phase function is typically normalized so its integral over the sphere equals 1, treating it like a probability density function. In contrast, astrophysics and atmospheric science often normalize phase functions so that their integral equals $\frac{1}{4\pi}$, which reflects a different baseline for isotropic scattering. Similar to BRDF models, there are many phase functions from parametrized approximated models (Henyey-Greenstein phase function [60]) to analytical models derived from first principles for known shape and material like spherical water droplets (Lorenz-Mie theory [97, 110] or Rayleight Scattering [68]). In this dissertation, we adopted the Henyey-Greenstein phase function due to its simplicity and anisotropic scattering behaviour. In Appendix C, we formally introduce this phase function and in Chapter 4 we model the scattering from diffusers inside the cosmetics foundation layer using a mixture of two Henyey-Greenstein phase functions.

This equation can be further simplified and restructured. First, the emission term can be ignored if the participating medium does not contain luminous particles, .ie., there is no volumetric light source $Q(x, \omega_o) = 0$. Second, we can combine the absorption and out scattering terms into a single term using the extinction coefficient $\sigma_t = \sigma_a + \sigma s$. The extinction coefficient specifies the density of the volume. Another quantity important for describing the appearance of the participating medium is the single scattering albedo $\alpha(x, \omega) = \sigma_s(x, \omega)/\sigma_t(x, \omega)$, which intuitively controls the color of the medium. Finally, the mean free path represents the average distance that a ray travel in a medium before colliding with a single particle.

Considering the two simplifications above the RTE can be rewritten as follow:

$$\omega_o \nabla L(x, \omega_o) = -\sigma_t L(x, \omega_o) + \sigma_s \int_\Omega f_p(x, \omega_i, \omega_o) L(x, \omega_i) d\omega_i \tag{2.11}$$

Jakob et al. [73] generalize the RT framework for an anisotropic participating medium by considering non-spherical particles known as microflakes as the phase functions and deriving the corresponding physical constraints for reciprocity and energy conservation. Microflake

theory can be seen as analogous to the microfacet theory introduced in the previous section for volumes. One of the key assumptions of the classical RTE formulation is that the volume is composed of statistically independent particles (white noise), .i.e, the formulation is not considering any kind of correlation between the particles. Jarabo et al [77] adopts the non-exponential generalized Boltzman equation for rendering spatially-correlated media based on local optical parameters.

In this dissertation, we do not consider the spatial correlation of particles but we consider the anisotropy of the media. In Chapter 4, we use the microflake theory to represent the specular platelets found in cosmetic foundation products.

2.4.2 *Volume Rendering Equation*

The differential form introduced above describes only local light effects. The equation needs to be transformed to its integral form in order to consider global light effects and compute the light transport simulation. Let us begin with the differential equation for the attenuation term:

$$\frac{dL(x,\omega)}{dt} = -\sigma_t(x,\omega)L(x,w). \tag{2.12}$$

This differential equation can be solved with an integral that account for the transmittance between two points x and x' using the ray parametrization $x + t\omega$:

$$\begin{aligned} T_r(x- > x') &= e^{-\tau(x,x')}, \\ \tau(x,x') &= \int_0^d \sigma_t(x+t\omega,\omega)dt. \end{aligned} \tag{2.13}$$

τ is known as the optical thickness between two points. $d = \|x - x'\|$ is the distance between the initial point and end point. The transmittance gives the fraction of the light attenuated by absorption or out scattering between two points. If the medium is homogeneous (σ_t is constant), the optical thickness can be computed analytically leading to Beer–Lambert law for the transmittance $T_r(x- > x') = e^{-\sigma_t d}$. We use this law to compute the absorption in the snake skin and feather appearance models presented later in Chapter 3 and 5 respectively.

A similar strategy applied to the full RTE equation leads to the *Volume Rendering Equation*:

$$\begin{aligned} L(x,\omega_o) = T_r(x- > x_t)L(x,w_o)+ \\ \int_0^t T_r(x- > x')\sigma_t(x,\omega_o)\left(\int_\Omega f_p(x,\omega_i,\omega_o)L(x,\omega_i)d\omega_i\right)dx', \end{aligned} \tag{2.14}$$

$x_t = x + t\omega_o$ and t is the depth of the medium. Similar to the rendering equation we introduced in the previous section, the evaluation of the volume rendering equation is recursive in its formulation. This global dependence on the radiance values at other locations in the participating medium makes the computation of this equation computationally expensive and challenging.

2.5 MONTE CARLO INTEGRATION

Solving the rendering and volume rendering equations is one of the primary tasks in photorealistic rendering of general scenes including surfaces and volumes. Analytical integration for general scenarios is not possible and in practice approximated solutions are computed with numerical integration. The recursive nature of these integration problems results in high-dimensional integrals, as solving the equation for an incident radiance at a given point involves considering the light energy distribution across multiple surfaces starting from the light sources. Monte Carlo integration techniques for estimating integrals using random sampling are particularly effective for solving high-dimensional integration problems avoiding the curse of dimensionality suffered by quadrature numerical integration techniques, where the number of samples typically increases exponentially with the number of dimensions. In contrast to deterministic quadrature techniques, the convergence rate of Monte Carlo techniques depends only on the number of random samples, not on the dimensionality of the integral.

Given an arbitrary integral $f(x)$ over a multidimensional domain D:

$$I = \int_D f(x)dx \tag{2.15}$$

The Monte Carlo estimator approximates the integral I using a set of random samples $x_1, x_2, \ldots, x_N$ drawn from a probability distribution $p(x)$ associated with the random variable X_i:

$$F_N = \frac{1}{N}\sum_{i=1}^{N}\frac{f(x_i)}{p(x_i)} \tag{2.16}$$

Notice that $p(x)$ must be nonzero for all the samples where $|f(x)|$ is larger than 0. The expected value F_N is equal to the integral I making the Monte Carlo estimator an unbiased estimator. This implies that the estimator will converge to the true value of the integral given enough samples, as it can be shown with the following proof using the definition of expection and its fundamental properties:

$$
\begin{aligned}
E[F_N] &= E\left[\frac{1}{N}\sum_{i=1}^{N}\frac{f(x_i)}{p(x_i)}\right], \\
&= \frac{1}{N}\sum_{i=1}^{N} E\left[\frac{f(x_i)}{p(x_i)}\right], \\
&= \frac{1}{N}\sum_{i=1}^{N}\int_D \frac{f(x_i)}{p(x_i)}p(x_i), \\
&= \frac{1}{N}\sum_{i=1}^{N}\int_D f(x_i), \\
&= \int_D f(x_i).
\end{aligned}
\tag{2.17}
$$

The convergence rate in error reduction for this estimate is $O(\sqrt{N})$, which can be easily derived by applying the variance definition to the estimate and its fundamental properties. Increasing the number of samples will reduce the error (manifested as noisy images) in a predictable way, but the computational cost and time might be too high for practical scenarios. One of the most powerful variance reduction strategies is *importance sampling*, where the samples are drawn from a pdf $p(x)$ that closely resembles the function $f(x)$ in the integrand. Intuitively, the idea is to treat the set of random samples carefully and place them where the absolute value of the integrand is large in order to reduce the error more quickly. However, finding a proper pdf might be challenging or too expensive to compute to be practical.

Over the years, several Monte Carlo-based algorithms have been developed by the computer graphics community, including path tracing [82], bidirectional path tracing [88, 156], photon mapping [79] and Metropolis light transport [155]. Path tracing solves the light transport equations with Monte Carlo integration by randomly tracing individual light paths from the camera to the light source. At each interaction, we obtain the new event by sampling the scattering function (e.g., the BSDF or phase function), and throwing a new ray in the sampled direction. In this dissertation, we focus on scattering models for complex materials and we used Monte Carlo path tracing to solve the light transport equations and render the images in this thesis. We adopt some of the variance reduction strategies mentioned above such as BSDF sampling via the pdf being particularly important for noise reduction as all Monte Carlo-based methods require the scattering model to implement an evaluation function, as well as a sampling routine.

Part II

REFLECTANCE MODELS

In this part, we present the *reflectance models* of the complex multi-scale materials we consider in this dissertation: snake skin, cosmetics and feathers. First, we study the intricate anatomy and chromatophores found in *snake skin* in Chapter 3 and propose a two-layered reflectance function to reproduce its dark tones and potential iridescent effects. Next, we shift our focus to *cosmetic foundations* in Chapter 4 and how they can be represented as a stochastic participating medium of specular platelets and diffuse scatterers. Finally, we investigate the multi-scale structure of *pennaceous feathers* in Chapter 5 and introduce a reflectance model that considers both the interaction of light inside the feather fibers and the occlusion between them.

3

A BIOLOGICALLY-INSPIRED APPEARANCE MODEL FOR SNAKE SKIN

Simulating light transport on biological tissues poses a significant challenge due to their intricate multilayered structures. The scattering models for cosmetic foundations in Chapter 4) and pennaceous feathers in Chapter 5 also exhibit multilayered planar and cylindrical structures, respectively. Among such tissues, the scales covering reptile skin stand out as remarkable examples, combining photonic structures and pigmentation. This chapter introduces a novel multilayered appearance model inspired by the anatomy of snake skin, which exhibits striking, highly iridescent scales caused by light interference. Our model captures this complexity by representing snake skin as a two-layered reflectance function: a thin, specular top layer producing iridescent reflections, and a dark, highly absorbing bottom layer that enhances the vibrancy of the iridescent colors.

We demonstrate the versatility of the layered material across a wide range of appearances and show that our model is able to qualitatively match the appearance of a specific specimen (Xenopeltis Unicolor). As first author, I led the writing of the manuscript and the modeling of the reflectance model. I presented this work at the Spanish Conference in Computer Graphics (CEIG) 2023.

J. Padrón, D. Bielsa, A. Jarabo & A. Muñoz
A Biologically-Inspired Appearance Model for Snake Skin
Congreso Español de Informática Gráfica (CEIG 2023)

3.1 INTRODUCTION

Photo-realistic rendering of biological tissues and structures, like feathers, fur or reptile skin, is still an open problem. The structural complexity at multiple scales of these biological elements result into complex light-matter interactions, manifested as intriguing appearances at macroscopic scale. One of the most remarkable and studied examples of biological tissues are the scales that cover the skin of reptiles, which present a combination of photonic structures and pigmentation. Unfortunately, current appearance models in computer graphics mostly ignore the complex anatomic structure of scales and its coloration mechanisms. In general, these appearances are modeled using time-consuming appearance matching by skilled artists. This limits the applicability of computer generated images in areas be-

yond movies and videogames, such as predictive rendering in paleontology [101, 106], meta-material prototyping, or data-generation for machine learning. In these fields, a predictive physically-grounded appearance model is a must.

In this work, we propose a practical biophysically-inspired appearance model for the skin of snakes. Skin snakes present a wide range of appearances, from simple diffuse ones to highly iridescent. Such complex appearance is the result of the underlying structure of reptile skin, roughly divided in three parallel layers: The first layer is like a platelet-like photonic glass responsible of iridescence, the second layer is a purely absorbing layer due to the concentration of melanophores, and the bottom layer is a diffuse layer (see the layered material inset Figure 3.1).

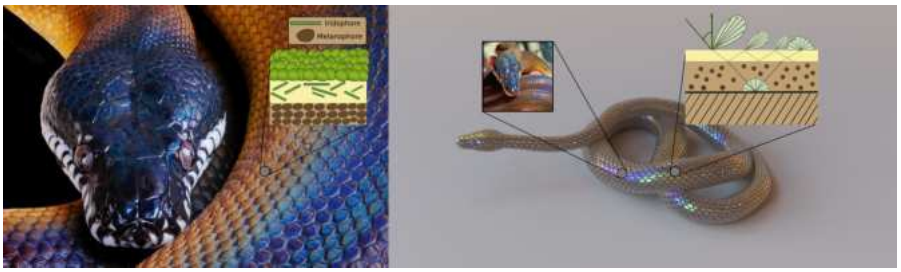

Figure 3.1: **Left:** Real photograph of a white lipped python [137]. A reptile scale is a biological tissue composed of multiple layers of chromatophores (see right inset) like irodophores (platelets) and melanophores (irregular ellipses). **Right:** A rendering of a snake 3D model using our practical reptile skin reflectance model roughly matching the general appearance. The snake skin is represented as a multilayered material with two layers (right inset): a thin film layer responsible of the iridescent patterns and a diffuse substrate surrounded by an absorbing media responsible of the darkening of the final appearance.

We build our model on top of the position-free model proposed by Guo et al. [52], where the top layer is modeled as a thin-film with parametrizable height, and the bottom absorbing layer accounts for both volumetric absorption and diffuse surface reflection. Then we demonstrate that our model is able to predict the appearance on real-world snakes, generalizes to other appearances, and it is practical and easy to incorporate in any RGB physically-based renderer. The source code and scenes are available on the project website (`https://graphics.unizar.es/projects/SnakeSkinAppearance_2023/`).

3.2 RELATED WORK

The complexity of real-world appearance is in part due to its underlying layered structure and the optical mechanisms involved in its coloration and scattering. Here we review the most relevant works related to our model, and refer the reader to other sources for a broader survey [43].

BIOLOGICALLY-INSPIRED APPEARANCE MODELS The modeling of biological models is not new in graphics, though most existing works have focused on accurately representing human skin [30, 31, 70] or hair [65, 103]. Other works have generalized hair to other keratin-based structures including fur [172, 173], feathers [66], or the Morpho butterfly wings [146]. Closest to ours, Dhillon et al. [28] modeled snake-skin surface appearances accounting for the diffraction due to grating-like photonic nanostructures in the scales. Later, Dhillon and Ghosh [29] proposed a Chebyshew approximation in order to reduce the runtime memory footprint of the surface nanostructure's lookup tables obtained by atomic force microscopy. However, their model requires capturing the surface nanostructure and performing a Fourier transform of the resulting height field, making the approach expensive and difficult to generalize. In contrast, our model simplifies the photonic behaviour of the skin by means of an easy-to-parametrize thin layer, making it easy to author and practical in render time.

VOLUMETRIC MATERIALS Light transport simulations of volumetric materials typically consists of solving the radiative transfer equation (RTE) [20], and its generalizations to anisotropic [73] and non-exponential [15, 77] media. We refer the reader to [119] for more details. In our work, we model the dark appearances of the reptile skin with a diffuse subtract surrounded with an homogeneous absorbing media.

WAVE OPTICS-AWARE APPEARANCE MODELS Wave optics phenomena generally manifests in two main phenomena: Diffraction and thin-film interference. Diffraction accounts for the Huygens principle, and it is generally based on the first-order Born approximation (the Kirschhoff equation) [26, 36, 47, 138, 171]. A particular case of wave-phenomena occurs in thin films, where interference between light paths of different path length result into colorful appearance. These works are the basis for Sun et al. [146] and Dhillon et al.'s [28] Morpho butterfly and snake skin models, respectively. On the other

hand, Smits and Meyer [136] introduced the first model accounting for such thin film. More recently, Belcour and Barla [13] extended the microfacet model to account for thin-film interfaces. This approach was leveraged by Huang et al. [66] to represent the iridescent appearance of the rock dove neck feathers, while pearlescent materials [50] are generally modeled by embedding thin-film platelets inside a clear media. In this chapter, we leverage thin-film interference to model the iridescent appearance of snake skin.

LAYERED MATERIALS Hanrahan and Kruger [54] introduced the first analytical single scattering model for layered materials. Donner and Jensen[30] developed a significantly faster solution for diffuse materials based on the multipole diffusion approximation. A similar approach was followed by Jakob et al. [76], and later Zeltner and Jakob [184], generalizing it to materials with any scattering frequency. However, these works require precomputation and significant storage. A more practical approach was the approximation by Weidlich and Wilkie [166] which represented each layer by using multiple BSDF lobes (one for each layer), by introducing several approximation and ignoring multiple scattering. Belcour [12]'s model followed a similar approach, but was able to account for multiple scattering and more complex phenomena. The most general approach is the one by Guo et al. [52], which leverages the position-free nature of BSDFs, and solves their appearance by using multiple importance sampling of bidirectional Monte Carlo paths inside the stacked volumes. We use this formulation in this work to efficiently compute the light transport simulation of our multilayered reptile skin material.

3.3 BACKGROUND

In nature, colours can be produced by pigments selectively absorbing some wavelengths of light, or by constructive and destructive wave interference on (partially) ordered structures at micro- and nacoscopic scale (structural coloration), or a combination of both mechanisms [133]. Some spectacular examples of structural coloration are the brilliant blue color in the wings of Morpho butterflies, the metallic reflection from the Japanese jewel beetles' wings, or the highly iridescent colors of the peacock feathers [181]. In reptiles, and more particularly in snakes, structural coloration can be found, for example, in the scales of the Xenopeltis unicolor snake. In this work, we are interested in snake scales, and in particular on how the epidermis structure and material properties of the skin affect the appearance at macroscopic scale. In the following, we first describe the anatomy of the snake skin; then, we briefly describe thin-film interference, a structural coloration phenomenon we leverage in this work.

3.3.1 *Snake skin anatomy*

The snake skin exhibits features that are structurally different from other living beings, in particular its scales and underlying skin layers. At a macroscopic level, the most relevant aspect for appearance is the scales pattern. There is a wide range of patterns depending on the different snake species.

At a micro-structure level, the skin is divided in multiple roughly parallel layers (see Figure 3.3a), where the most relevant for appearance is the outermost epidermis layer (the *oberhäutchen*). This layer can also be divided in multiple sublayers, as shown in Figure 3.3b. While scanning electron microscopy (SEM) of skin cross sections [86, 179] reveal a significant variation in the epidermis structure between species, most light interactions occur at the outermost layer. At the top of this *oberhäutchen* we can find the *iridophores*, which is a photonic structure made of small thin platelets, which interact with light as small thin-film elements. Depending on whether these iridophores are ordered or not, they result into more or less visible iridiscense. Below these iridophores there is a dark pigment layer, dominated mostly by eumelanin. This layer of pigments can be divided into two layers: the top one is a pigmented layer with disordered melanocites that absorb light, while the bottom one is a soft tissue that acts as a diffuse reflector.

3.3.2 *Thin-film interference*

The iridophores inside the *oberhäutchen* produce iridescence by a mechanism generally called *thin-film interference*. Thin-film interference is the result of multiple reflections inside a parallel dielectric film, of thickness in the order of the visible light wavelength.

Let us consider a parallel thin film with thickness δ and index of refraction (IOR) η_1, between two media with IOR η_0 on the top and η_2 on the bottom. As an incident light with wavelength λ and incidence angle θ interacts with the dielectric thin, it might be either reflected or refracted following the Fresnel equations. When transmitted inside the thin film, light might suffer several reflections inside it before it is transmitted back, either from the top to the medium with IOR η_0 or the bottom to the medium with IOR η_2 (see Figure 3.2, left). Everytime it interacts with the surface of the film, light is attenuated by the Fresnel term by a factor $r_{i|j} = \text{Fresnel}(\theta, \eta_i, \eta_j)$ if reflected at the interface between media with IOR η_i and η_j respectively, or $t_{i|j} = 1 - r_{i|j}$ if transmitted. In addition, as light travels inside the thin film, it suf-

fers a phase delay proportional to the traveled distance.

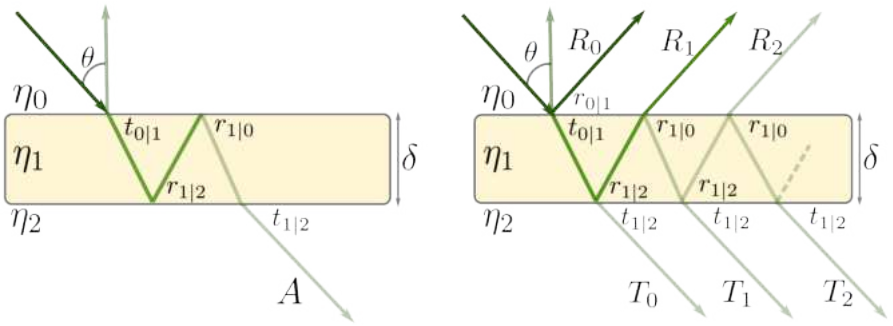

Figure 3.2: Illustration of the optical path length difference for light reflected from the upper and lower boundaries of a thin-film interference. **Left:** A particular light path, where $r_{i|j}$ and $t_{i|j}$ denotes the amplitude of the reflection and transmission from layer i to layer j. **Right:** General scenario for a single thin-film scenario. The dashed lines implies the path continues indefinitely.

As light emerges from the thin film, either from the top (reflection term R) or the bottom (transmission term T) with different phases depending on the traveled optical depth (see Figure 3.2, right), it might interact constructively or destructively, and this interference is dependent on the light's wavelength λ. This results in a rainbow-like color, which is dependent on the angle of incidence.

Assuming that the IOR of the thin film η_1 is real (there is no absorbption inside the thin film), we can compute the total reflected energy I_R using the Airy summation, as

$$I_R(\lambda, \theta) = \left(\frac{n_2 \cos\theta_2}{n_0 \cos\theta_0}\right) \frac{|t_{0|1} t_{1|2}|^2}{|r_{1|0} r_{1|2}|^2 - 2 r_{1|0} r_{1|2} \cos\phi + 1}, \tag{3.1}$$

with ϕ the phase delay between two consecutive reflected paths, computed as

$$\phi = \frac{4\pi}{\lambda} \eta_1 \, \delta \cos(\theta_1)) + \Delta, \tag{3.2}$$

with θ_1 the refracted angle in the thin-film layer, and Δ the phase change due to Fresnel interaction, computed as

$$\Delta_{i|j} = \begin{cases} 0 & \text{if } \eta_i > \eta_j, \\ \pi & \text{if } \eta_i < \eta_j. \end{cases} \tag{3.3}$$

Similarly, we can compute the transmitted energy I_T as $I_T(\lambda, \theta) = 1 - I_R(\lambda, \theta)$ A thorough derivation of this formula can be found in multiple sources (e.g. [178]).

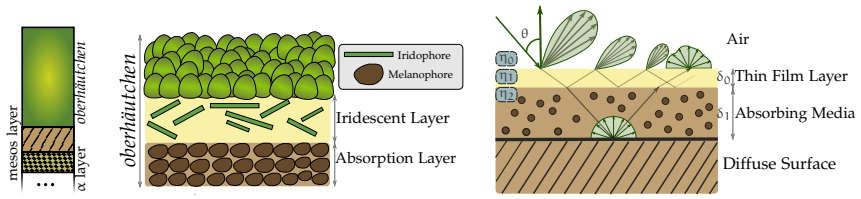

(a) Anatomy (b) Snake skin outer layer (c) Our layered material

Figure 3.3: Illustration of the multilayered model for snake skin. **(a)** A sketch of the snake skin anatomy, which is, essentially multilayered. **(b)** The outer layer (epidermis) of the snake skin is fundamental for the appearance beyond the scales (depicted in green), as it contains different types of chromatophores such as iridophores and melanophores. **(c)** Our multi-layered material representation is composed of a thin-film layer responsible of the iridescent effects and a diffuse substrate surrounded by an absorbing media mimicking the appearance of the melanophores' layer.

3.4 OUR APPEARANCE MODEL

We model the appearance of snakes skin using a multilayered BSDF that represents the outermost *oberhäutchen*. The first layer reproduces the iridescent effects via thin-film interference (see Section 3.4.2). The second layer consists of a diffuse surface surrounded by an absorbing media, modeling the darkening and saturation of the final appearance (Section 3.4.3). Our model is summarized in Figure 3.3c, while the parameters of our model can be found in Table 3.1.

Parameter	Definition
δ_0	thickness of the thin film layer (nm)
η_0	refractive index of the top layer
η_1	refractive index of the intermediate layer
η_2	refractive index of the bottom layer
σ_a	absorption coefficient of the absorbing media
δ_1	thickness of the absorbing media layer (nm)
k_d	albedo of the diffuse surface

Table 3.1: Parameters used in our snake skin BSDF. The thickness of the layers are given in nanometers. We set $\eta_0 = 1.0$ and $\eta_1 = 1.53$ to the air and keratin IOR respectively.

3.4.1 *Scales mesogeometry*

We model the scales of the snake skin as a mesogeometry, using a tileable bump mapping. In our examples, we simulate the scales of the *Xenopeltis unicolor*, which roughly follow a uniform hexagonal grid, as shown in Section 3.4a. In our case, we manually create the bump map texture; creating a procedural model similar to Voronoi cells of a blue noise distribution of points for the skin's scales is left as future work.

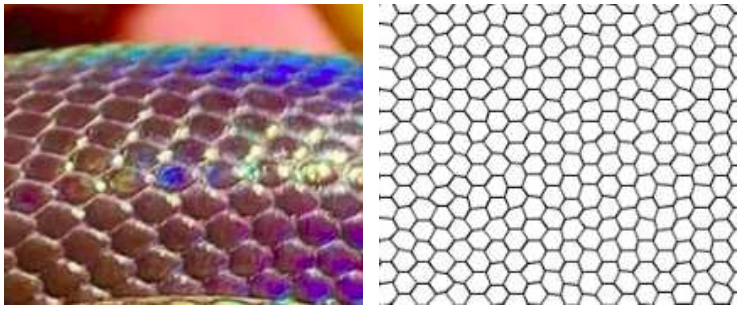

(a) Real scales (b) Bump map texture

Figure 3.4: Modelling snake scales as a bump map. **Left:** Prominent iridescent scales from a Xenopeltis Unicolor (close-up photography[1]). **Right:** The scale patterns can be faithfully approximated by a hexagonal grid texture.

3.4.2 *Iridescent layer*

The outermost layer in the skin of snakes is the so-called iridescent layer, which is a dielectric non-absorbing layer with a quasi-regular photonic structure consisting of several (potentially oriented) iridescent platelets (see Section 3.3). While volumetric models in the spirit of Guillén et al.'s [50] could be used for modeling this layer, we opted for a simpler approximation at the cost of potentially reducing our model expressivity.

We assume that the aggregated effect of the platelets can be approximated well by a single thin iridescent layer, following the Airy reflectance described in Equation 3.1 (and its analogous for transmittance). Thus, we model the reflectance and transmission of this first layer as the BSDF

$$f_0(\omega_i, \omega_o) = \delta(\omega_o - \omega_r) I_R(\theta) \tag{3.4}$$

$$+ \delta(\omega_o + \omega_i)(1 - I_R(\theta)), \tag{3.5}$$

with ω_r the reflected direction. For clarity, we omit the wavelength dependency of the BSDF. This approximation has been shown to be

accurate for oriented iridescent platelets [34] as Belcour and Barla work [13] shown in their Figure 21, and assuming a fixed IOR allows for changing the appearance of the skin by using a single parameter (the layer thickness), instead of the multiple parameters required by the model of Guillén et al.[50].

3.4.3 *Absorbing layer*

The second layer in our model is an absorbing diffuse layer, modeling the dielectric volumetric layer with melanosomes in snake skin, and the diffuse reflector behind that volumetric layer. As mentioned before, a pigmented layer behind the iridescent layer is crucial for enhancing the structural coloration of snakes.

We model the absorbing layer using the classical Beer-Lambert exponential transmittance, on top of a diffuse reflector. For quick evaluation, we combined these two effects together in a single BRDF as follows:

$$f_1(\omega_i, \omega_o) = \frac{k_d}{\pi} e^{-\sigma_a \frac{\delta_1}{|\mathbf{n}\cdot\omega_i||\mathbf{n}\cdot\omega_o|}}, \tag{3.6}$$

with k_d the albedo of the diffuse surface, σ_a and δ_1 are the absorption coefficient thickness of the absorbing layer, and $\mathbf{n}$ the normal of the surface.

3.4.4 *Implementation*

We implemented our reflectance model as a BSDF plugin in Mitsuba [72], on top of the position-free Monte Carlo (PFMC) framework of Guo et al. [52]. It allows us to easily compute the multiple interactions between the iridescent and absorbing layer, by explicitly modeling the light transport inside the multilayered material. PFMC assumes that each layer is horizontally infinite, which allows to remove the horizontal position at the layered material, which is crucial for performing next-event estimation under smooth dielectric boundaries. We also leverage the bidirectional multiple importance sampling estimator in PFMC for further reduce variance when evaluating and sampling our model.

Despite the wavelength dependency of thin-film-based iridiscense, we opt for a traditional RGB rendering pipeline, using three representative wavelengths for the computations roughly representing RGB (650, 510 and 475 nm, respectively). While this is prone to spectral aliasing [13] we found that the results were reasonable, and made

our implementation and integration in Mitsuba simpler.

3.5 ANALYSIS AND RESULTS

We now present the evaluation of our method, which consists of an ablation study of our final appearance model and an analysis of the appearance range of our thin film materials. Next, we perform a performance study, where we compare the rendering time for different image resolutions and composition.

3.5.1 *Validation*

We validate our model qualitatively by comparing renders with real photographs of the *Xenopeltis unicolor* snake. The renderings were obtained by creating a similar scene in Mitsuba, where the snake geometry and texture scales coarsely matched the snake. As shown in Figure 3.1, our renders qualitatively match the general appearance of the photographs under comparable lighting and viewing conditions. Notice the similarity of the iridescent patterns.

3.5.2 *Appearance Analysis*

We first demonstrate our model by exploring the range of appearances that our model is able to generate. Figure 3.5 shows the results of this study: We fix the index of refraction of the top layer and intermediate layer to $\eta_0 = 1$ (air) and $\eta_1 = 1.56$ (keratin), respectively, and render a snake scene varying the thickness of the thin film layer δ_0 (rows) and the refraction index of the bottom layer η_2 (column). As we can see in the figure, the appearance changes drastically in both scenarios.

3.5.3 *Ablation studies*

In Figure 3.6 we analyze the contribution of each component of our appearance to the final overall appearance. In addition to the snake model, we also leverage two additional geometries (a sphere and a toroid). We demonstrate the importance of the mesoscopic bump-based detail, the iridescent layer, and the bottom absorbing layer. This ablation study shows that each component of our appearance model is indeed important for the final appearance.

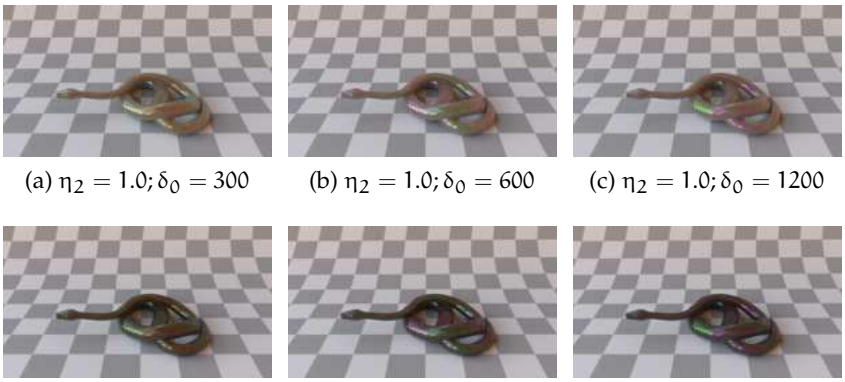

(a) $\eta_2 = 1.0; \delta_0 = 300$ (b) $\eta_2 = 1.0; \delta_0 = 600$ (c) $\eta_2 = 1.0; \delta_0 = 1200$

(d) $\eta_2 = 2.0; \delta_0 = 300$ (e) $\eta_2 = 2.0; \delta_0 = 600$ (f) $\eta_2 = 2.0; \delta_0 = 1200$

Figure 3.5: Appearance range study of our thin-film layer. Default parameters: thin-film layer ($\eta_0 = 1$ and $\eta_1 = 1.56$), absorption layer ($\sigma_a = 0.7$, $\delta_1 = 2$ nm, $k_d = 0$). **Top:** varying the thickness of the thin film layer; **Bottom:** varying the index of refraction of the bottom layer η_2.

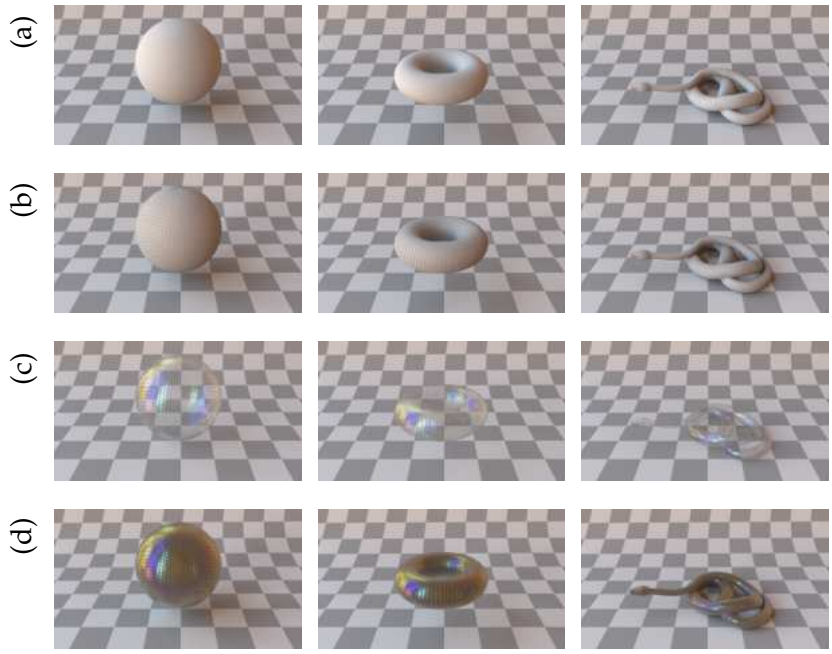

Figure 3.6: Ablation studies of our BSDF model for reptile skin. **(a)** Geometric models with diffuse material ($k_d = 0.3$). **(b)** Adding bump mapping on top of the underlying surface in order to model the macroscopic appearance of the scales. **(c)** Replacing the diffuse material with our rough thin-film interference ($\eta_0 = 1$, $\eta_1 = 1.56$, $\eta_2 = 1.0$, $\delta_0 = 900$nm). **(d)** Adding an absorption layer ($\sigma_a = 0.7$, $\delta_1 = 2$ nm, $k_d = 0.0$) in order to darker the final appearance.

3.5.4 *Performance*

We create all our renders using the position-free Monte Carlo integrator in Mitsuba 0.6 on an Intel Core i9-10900KF CPU with 20 cores.

Fig.	Time (sphere)	Time (torus)	Time (snake)
3.6 (a)	2.3 min	2.6 min	2.5 min
3.6 (b)	2.3 min	2.6 min	2.6 min
3.6 (c)	3.1 min	3.5 min	3.5 min
3.6 (d)	4.5 min	4.0 min	3.5 min

Table 3.2: Rendering time for our ablation studies (Fig. 3.6) using 1024 spp and a HD image resolution (1280×720).

A render of a 3D snake geometry with 1024 spp takes 3.1 min and 7.5 min for HD (1280×720) and full HD (1920×1080) image resolutions respectively. We report the rendering time in Table 3.2 on the same machine for our ablation studies experiment. Our multi-layer material is only 1.5 times slower than a traditional diffuse material.

3.6 DISCUSSION AND CONCLUSIONS

We have introduced a practical reflectance model for efficient rendering of skin of snakes. Our appearance model is built as a multilayered material composed of two layers: The irodophores layer (top layer) responsible of the highly iridescent colors is represented as a thin-film layer, while the bottom layer responsible for the dark pigments is modelled as a diffuse substrate surrounded by an absorbing media. We verify visually that our appearance model can qualitatively match the appearance of a real snake (the *Xenopeltis unicolor*).

LIMITATIONS AND FUTURE WORK Our model is based on several assumptions, which allows a practical and easy to integrate model, but that departs slightly from the real phenomena in the skin of snakes. First of all, our model is based on the BSDF, and ignores all non-local effects existing in organic materials due to subsurface scattering. However, given the structure of the snake skin, where most of the appearance is dominated by specular reflection in the epidermis, is reasonable to think that translucency will likely play a minor role in appearance.

The second approximation is on the iridescent layer: As discussed above, we simplify the modeling of the layer as a simple global thin-layer on top of a diffuser. This is practical and efficient, but a coarse simplification of the actual structure. Including a platelet-based iridescent model, potentially with a distribution of platelets orientation, might likely increase the expressivity of our model, at the cost of making it more expensive.

Additionally, while our structural coloration model (thin-film interference) is one of the main sources of structural coloration, others such as diffraction gratings due to the regular nanoscopic structure of the epidermis [28] have been omitted in our case. Nevertheless, we have shown how thin-film interference provides a versatile and expressive tool, that is very efficient and suitable for multilayered material representations (as opposed to diffraction gratings) and provides a wide range of snake skin appearances. In terms of parameter tuning, our appearance model is more compact and practical as the final appearance is only defined with 7 global parameters (see Table 3.1) and it does not require measured data by a complex capture process neither an expensive precomputation. Finding a practical way to include surface grating nanostructures to our appearance model might be one step closer to the underlying physical light transport happening at reptile skin.

Finally, the light transport itself is rather limited in our renders, reducing light interactions to tristimulus ray-optics-based models. Generalizing our model to account for the full spectrum is trivial. Including more advanced light transport effects, such as the effect of coherence [142] in a physical light transport simulation would require additional development, but would bring our model closer to an actually-predictive simulation of appearance.

Our appearance model is potentially capable of generating a wide range of appearances. Nevertheless, only a relatively small subset corresponds to real snakes' appearances. Exploring a wider range of snakes, as well as a broader set of reptiles and fishes that present comparable structure in their skin, is an interesting avenue of future work.

4

A PRACTICAL APPEARANCE MODEL FOR COSMETIC FOUNDATIONS

This chapter presents a novel scattering model for digitally reproducing the appearance of cosmetic foundation products mimicking a wide range of cosmetic appearances, from glossy to matte to velvety looks. The model consists of a volume represented by a multilayered BSDF similar to Chapter 3, but unlike the snake skin case, it allows the stacking of multiple cosmetic layers instead of a fixed two-layer configuration. Each cosmetic layer consists of a stochastic participating medium filled with two types of scatterers such as spherical diffusers and specular platelets inspired by the most prominent microscopic particles inside cosmetic foundations in terms of shapes and optical properties. Light transport inside the layered BSDF is simulated by solving the RTE Equation 2.9 using the position-free Monte Carlo framework, which accounts for arbitrary layers and multiple scattering.

Validation against real reflectance data shows its accuracy, while its flexibility is demonstrated thoroughly by appearance exploration tests. As second author, I helped the first author with the writing of the manuscript, the implementation, and experiments of the reflectance model. In addition, I lead the optimization behind the model fitting to reflectance measurements. This work has been accepted for publication in the Computer Graphics Forum and presented by the first author at the 35th Eurographics Symposium on Rendering.

D. Lanza, **J. Padrón**, A. Pranovich, A. Muñoz, J. Frisvad & A. Jarabo
A Practical Appearance Model For Cosmetic Foundations
Computer Graphics Forum (EGSR 2024)

4.1 INTRODUCTION

Since ancient times, decorative cosmetics have been used in virtually all existing cultures around the globe. From the prehistoric mineral-based pigments [165] to modern sophisticated chemical makeup, cosmetics have been used for enhancing appearance and hiding imperfections, for ritual painting, theatrical purposes, or most recently, visual effects. However, despite their ubiquity, cosmetics have not been explored much in graphics, most likely because they are generally baked into the look-development process for virtual humans. Rendering of cosmetics has received little attention, limited to image-

space [116, 170, 174] or texture-space manipulation [131, 177], or simplistic physical models [64, 91, 92]. Existing models either directly manipulate an image or describe how cosmetics modify the parameters of conventional analytic shading models. Our approach models the light-scattering particles in the cosmetic layer and computes the effect of such a layer using position-free Monte Carlo simulation.

Several types of cosmetics exist with different areas of application and intended goals. In the case of facial makeup, one or more relatively thin layers of cosmetics are applied on top of the skin, resulting in a multilayered structure. Facial makeup cosmetics, including *foundation*, *concealers*, *rougers* (*blusher*), *bronzers* and *highlighters*, consist of a combination of microscopic colored diffusers and platelets, either suspended in a water-based host medium, or presented as powder that sticks to the outermost sebum layer of the skin. At a macroscopic level, the diffusers and platelets interact with light as a scattering medium.

In this chapter, we focus on the base layer or *foundation*. A foundation aims to provide a uniform skin hue over the whole face upon which other makeup layers can be stacked. A key visual attribute of a foundation layer is its *finish*: Different foundation products exhibit distinct visual characteristics ranging from a *matte* finish that results in a non-shiny, velvety appearance; to a *dewy* finish that aims for a more natural appearance making the skin brighter and shinier to evoke an impression of a healthy skin.

Based on the observed types of appearance existing in foundation cosmetics, we propose an intuitive empirical appearance model for foundation makeup, where we model each cosmetic layer as a finite volumetric scattering layer, and where the bulk scattering properties are derived from a mixture of spherical-like and platelet-like scatterers. This enables us to stack an arbitrary number of makeup layers, resulting in a single bidirectional scattering distribution function (BSDF). We implement our model using the position-free Monte Carlo formalism [52], allowing for multiple scattering and arbitrary distributions.

Our model is able to reproduce a wide variety of appearances, from dewy to matte. We compare our model against measurements of real-world cosmetics, and show that our model closely fits such measurements, while reproducing the main visual features of cosmetics when applied on top of digital human skin. In addition, we show that our model can be used to model other types of cosmetics (e.g., blusher) and enables the stacking of multiple makeup layers as exemplified in

Figure 4.1.

Figure 4.1: We propose a practical appearance model for foundation cosmetics that can be stacked on top of human skin. Left: Rendering of a white female character skin without makeup. Middle: We apply a *foundation* layer with a matte finish, which reduces the specular highlights, especially visible in the eye region and next to the nose, and slightly changes the skin color. Right: We apply an additional *shinier* layer adding a reddish tint to the cheek.

4.2 RELATED WORK

VOLUMETRIC MATERIALS. Simulation of light scattering in a volume generally involves solving the radiative transfer equation [20] or its variants for anisotropic [73] or correlated media [15, 77]. Based on this theoretical framework, numerous appearance models have been proposed for materials such as skin [3, 31, 70, 139], paper [123], cloth [187, 188], leaves [5], special pigments [50], ice [42], wood [94, 104], or granular media [108, 113]. This chapter follows this line of work and models foundation makeup as a combination of isotropic and anisotropic scatterers inside a scattering medium.

MULTILAYERED MATERIALS. Early work on rendering of multilayered materials simulated the reflection and transmission by the multilayered structure of skin and leaves using subsurface scattering [30, 54], being limited to diffuse reflectance. Later work proposed using the adding-doubling method on spatio-angular scattering representations of thin slabs for stacks of isotropic [76] and anisotropic layers [184]. These methods require expensive precomputation and large storage requirements. On the other hand, approximate models have been successful in practice, due to their efficiency and simplicity [12, 166, 167]; these methods follow the microfacets formalism, which makes them very suitable for integration in modern offline and real-time renderers, at the cost of reduced fidelity of the underlying light transport. A more accurate precomputation-free solution was proposed by Guo et al. [52] based on Monte Carlo random-walks inside the layered material; they leveraged a position-free formula-

tion of light transport for providing bidirectional estimators of the BSDF, leveraging variance reduction via multiple importance sampling. This work was later extended to support more advanced sampling estimates [44, 169]. Previous work [160] proposed a different formulation for multilayered materials, by proposing index-matched layers. This significantly simplified the layer stacking, allowing for closed-form solutions for the single-scattering BRDF, and allowing simple learning-based multiple scattering approximations. This learning strategy was recently further explored for all components of the BRDF [51]. In this chapter, we leverage multilayer material formulations for the modeling of our makeup BSDF. Specifically, we implement our model on top of position-free Monte Carlo [52], following the index-matched simplifications that previous work proposed [160] in the context of layered materials.

VISUAL REPRODUCTION OF COSMETICS. A considerable body of work on visual reproduction of cosmetics has focused on image-space makeup transfer [21, 27, 81, 93, 95, 96, 147, 159, 170, 174, 176]. Such works do not aim at characterizing the underlying properties of cosmetics but rather transfers an example of makeup from an input photograph to a target image, as in style-transfer methods. The facial appearance of a 3D model is usually described by textures. One way to encode makeup is to model how texture layers like diffuse, specular, and scattering albedo change when the cosmetic is applied [131, 177]. While these methods are useful for setting parameters in an analytic spatially-varying BRDF, like the conventional microfacet model [151], they do not enable us to compute the appearance of an applied cosmetic based on the constituents of the makeup material. With reflectance measurements from a gonioreflectometer one can fit a microfacet model to the data and use this to analyze the appearances of different cosmetics. This has been done for liquid foundation cosmetics [111, 150], and the researchers found that a data-driven model based on principal component analysis (PCA) provided a better representation of the data than the Torrance-Sparrow model. However, a data-driven BSDF does not lend itself to editing and representation of related materials. Closer to our work, Huang et al. [64] and Li et al. [91, 92] reproduced the appearance of a liquid foundation by modeling a cosmetic layer using Kubelka-Munk theory for the diffuse reflectance and transmittance of the layer and a microfacet model for its specular reflectance. However, as found in the PCA study, the conventional analytic microfacet BRDF model cannot accurately capture the directional distribution of the scattered light and the Kubelka-Munk theory is diffuse, .ie, there is no directional dependency. In contrast, we model the appearance of foundation makeup by computing the directional distribution of the light due to scattering by the different

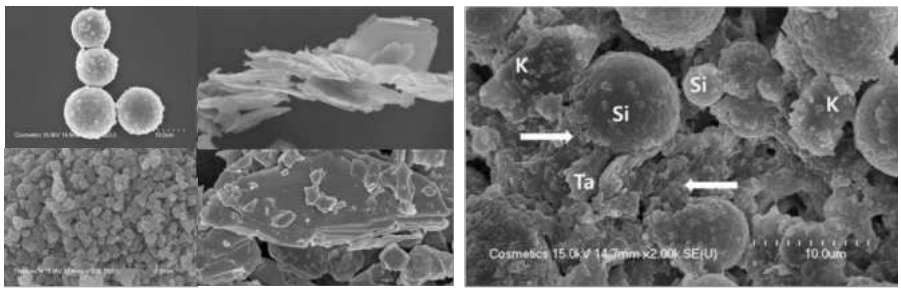

Natural State Product Powder Mixed

Figure 4.2: Scanning electron microscope (SEM) image of different minerals in their natural state (left, in clockwise order): Silica, Talc, Kaolin and Titanium Dioxide. Note how Talc and Kaolin have a polygonal and plate-like geometry, while Silica and Titanium Dioxide have a more round or cubic shape. SEM image of the product powder mixed with the Sebum stratum (right). Courtesy of Jeon and Chang [80].

types of particles inside the layer.

4.3 FOUNDATION COSMETICS

Foundation cosmetics, as well as other types of cosmetics (e.g., eyeshadows, lipsticks or primer), are generally made from a combination of colorants, minerals, vitamins and other chemicals included for skin health reasons [164]. A fundamental distinction between foundations is the base used for dispersing these constituents. *Liquid-based foundations* typically disperse these particles within a host medium such as water or silicone. As the majority of the particles are not soluble in the host medium (talc is not water-soluble, for example) the final system is colloidal, meaning that tiny particles are dispersed within the host medium. In contrast, *powder-based foundations* use the sebum stratum to bind these materials together, forming a layer in which cosmetic particles are mixed with the sebum [80]. Common colorants include minerals such as talc, kaolin, silica, or titanium dioxide, which are present as small powder-like particles with different shapes [80]. While minerals like kaolin and talc have flake-like polygonal geometry, titanium dioxide or silica tend to have spherical or cuboidal shapes (Figure 4.2). This difference in shape results in radically different scattering behaviour, leading to a different *finish* of the makeup. The color and finish are thus the two most important visual attributes for a correct reproduction of the appearance of a foundation layer.

COLORATION Since foundation layers are used to create an even layer, the color and hue of the foundation have to roughly match

the underlying skin hue, making colorants a key aspect of a foundation layer. Colorants can be categorized into two types: dyers, derived synthetically, and pigments, which have a biological origin. As colorants can have an impact on human health, efforts have been intensified to develop new technologies to ensure a stringent control of colorant concentration in cosmetic products [48, 49]. The main source of coloration is scattering and absorption, since regulations [19] do not allow coloration through photoluminescence or other chemical reactions. In addition, diffractive particles are allowed to be used as colorants in effect pigments [102], though these are not common due to the need for running extra safety studies. We focus on the most common scattering-based colorants.

FINISH Different foundations exhibit distinct visual characteristics ranging from a *matte* finish, resulting in a non-shiny, velvety appearance, to a *dewy* finish, aiming to achieve a more natural appearance that makes the skin brighter and shinier to evoke an impression of a healthy skin. The finish of a foundation layer is mainly caused by the concentration and shape of the different particles that constitute the bulk properties of the material, which directly affects the scattering behaviour. While flake-like particles scatter light more coherently, spherical particles scatter light in a more isotropic fashion, leading to a more matte appearance.

SUMMARY The appearance of foundation cosmetics is the result of multiple scattering by a thin scattering medium, modeled by the combination of two types of scattering behaviour: On one hand, we can assume that diffusers are responsible for the diffusive look and incoherent backscattering in matte appearances, while more directional scatterers (such as platelets) model the more coherent scattering reflection responsible for the highlights prominent in dewy foundations. These are somewhat aligned with different types of particles used to produce foundation cosmetics. Based on these different types of observed type of scattering, in the following we present our model, defined using radiative transfer theory as a mixture of different scatterers in a scattering medium.

4.4 A BSDF FOR FOUNDATION COSMETICS

As described in Section 4.3, foundation cosmetics are applied as a layer on top of the skin, and its appearance is the result of the volumetric scattering in the layer. We model the layer statistically, as the combination of two uncorrelated scatterers uniformly distributed in

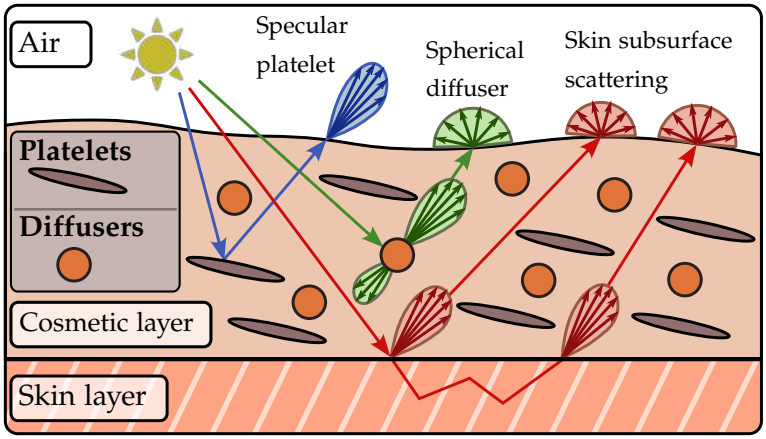

Figure 4.3: We model a single thin foundation layer as a medium filled with two types of particles (platelets and spherical diffusers) ignoring lateral scattering. Platelets generate specular lobes, using a more anisotropic phase function. In contrast, spherical diffusers generate rougher finishes, due to a more isotropic phase function. We account also for the subsurface scattering due to the underlying skin model.

the medium: spherical diffusers and anisotropic reflective platelets. Figure 4.3 shows a diagram of our model for a single foundation layer over the skin.

We assume elastic scattering, i.e., both the energy and scatterers numbers are conserved, and negligible wave-optical coherence in the multiple scattering component. In addition, given the small thickness of foundation layers, we assume no horizontal scattering, and therefore that light exits at the same position as it enters. Thus, we represent the foundation layer using a BSDF, defined as the result of all light-matter interactions occurring in the cosmetic for a ray of incident light at direction ω_i and exiting the surface at direction ω_o. Following Guo et al. [52] we model $f(\omega_i, \omega_o)$ using a position-free variant of the path integral as

$$f(\omega_i, \omega_o) = \int_{\Omega(\omega_i, \omega_o)} \Phi(\mathbf{x}) d\mu(\mathbf{x}), \tag{4.1}$$

with $\Omega(\omega_i, \omega_o)$ the space of light paths entering and exiting the differential surface at directions ω_i and ω_i respectively, $\Phi(\mathbf{x})$ the contribution of the path $\mathbf{x} \in \Omega(\omega_i, \omega_o)$ as the sequence of scattering and absorption events inside the foundation volumetric layer, and $\mu(\mathbf{x})$ the measure of path $\mathbf{x}$. By construction, the BSDF modeled by Equation (4.1) is energy conserving and reciprocal only if the scattering events conserve energy and are reciprocal. Table 4.1 lists all the parameters used in our model (BSDF), including both bulk and user parameters.

4.4.1 *Optical properties of the foundation layer*

We model the foundation layer as a statistical volumetric scattering plane-parallel layer with thickness t. To account for specular-like scattering, we describe light transport using the anisotropic radiative transfer framework [73], and describe radiance L in the direction of observation ω_o following

$$(\omega_o \cdot \nabla)L(\omega_o) + \sigma_t(\omega_o)L(\omega_o) = \sigma_s(\omega_o) \int_\Omega f_p(\omega_o \to \omega)L_i(\omega)\, d\omega, \tag{4.2}$$

with $\sigma_t(\omega_o)$ and $\sigma_s(\omega_o)$ the direction-dependent extinction and scattering coefficients, Ω the unit sphere of directions, $f_p(\omega_o \to \omega)$ the phase function, and $L_i(\omega)$ the incoming radiance in direction ω. Note that we omit the spatial and spectral dependencies for clarity, and assume that the source term is outside the scattering layer.

We assume a match of the indices of refraction of the particle host medium and the outside medium (as in powder-based foundations). The resulting absence of scattering and refraction at the interface allows for a simpler evaluation at render time and simplifies the parameterization of our model. Even liquid foundations tend to form a semi-dry film once applied. Most of the appearance is thus the result of the interaction with only the minerals and colorants. In Section 4.5 we validate this choice.

Parameter	Definition
η	Complex refractive index (=1)
t	Layer thickness
c_d	Diffuser particles concentration
Λ_d	Single scattering albedo for spherical diffusers
g_1, g_2	Anisotropy of diffuser's lobes
w_g	Weighting factor of diffuser's lobes
Λ_p	Single scattering albedo for platelets
α_p	Platelets roughness value
θ_p	Platelets rotation along the tangent direction

Table 4.1: Parameters of our cosmetics model for a single layer.

MODELING THE OPTICAL PARAMETERS The anisotropic RTE (4.2) is characterized by the extinction and scattering coefficients, $\Sigma_t(\omega_o)$ and $\Sigma_s(\omega_o)$, and the phase function $f_p(\omega \to \omega_o)$. We assume that the host medium has negligible effect on these optical properties, and

thus only spherical diffusers and platelets are responsible for the appearance. This is reasonable since the thickness of foundation layers is usually small, and the layer is in a semi-dry state.

Building on top of the spatial uncorrelation assumption, we model the extinction coefficient as the combined probability of extinction for both diffusers $\sigma_d(\omega_o)$ and platelets $\sigma_p(\omega_o)$, following

$$\sigma_t(\omega) = \sigma_d(\omega) + \sigma_p(\omega) = N_d\, C_d + N_p\, C_p(\omega), \tag{4.3}$$

with N_d and N_p the number density of spherical diffusers and platelets in m^{-3}, respectively, and C_d and $C_p(\omega)$ their extinction cross sections in m^2. For simplicity, we set $C_d = \max C_p(\omega) = 1$. Note that the extinction cross-section of the spherical diffusers has no dependency on the direction. To find practical user parameters, we model extinction as a function of a base extinction

$$\sigma_{base} = \sigma_d + N_p \max_{\omega} C_p(\omega) \tag{4.4}$$

representing the non-directional part of the extinction coefficient for all the scattering particles in the material. To include the directional dependency, we use

$$\sigma_t(\omega) = \sigma_{base} \left(c_d + (1 - c_d)\, \hat{C}_p(\omega)\right), \tag{4.5}$$

with $\hat{C}_p$ the normalized version of the extinction cross-section of the platelets and c_d the relative concentration of spherical diffusers out of the total concentration of particles:

$$\hat{C}_p(\omega) = \frac{C_p(\omega)}{\max_\omega C_p(\omega)} \quad \text{and} \quad c_d = \frac{\sigma_d}{\sigma_{base}}. \tag{4.6}$$

Since we do not include absorption in our model for computing the extinction cross-section and assume that all chromatic effects are due to absorption, our $C_p(\omega)$ has no spectral dependency. To introduce practical parameters for specifying the part not being absorbed, we use non-directional spectral single-scattering albedos for the spherical diffusers Λ_d and the platelets Λ_p. The single-scattering albedo is defined by $\Lambda(\omega) = \sigma_s(\omega)/\sigma_t(\omega)$, so we use the factors for diffuse and directional extinction in Equation 4.5 to model this:

$$\Lambda(\omega) = \frac{\Lambda_d\, c_d + \Lambda_p\, (1 - c_d)\, \hat{C}_p(\omega)}{c_d + (1 - c_d)\, \hat{C}_p(\omega)}. \tag{4.7}$$

Finally, we build our phase function as a linear blend of the phase functions of diffusers and platelets f_d and f_p, weighted by the total scattered light by each of the particles following:

$$f(\omega \to \omega_o) = \frac{\Lambda_d\, c_d\, f_d(\omega \to \omega_o) + \Lambda_p\,(1-c_d)\,\hat{C}_p(\omega)\, f_p(\omega \to \omega_o)}{\Lambda_d\, c_d + \Lambda_p\,(1-c_d)\,\hat{C}_p(\omega)}. \quad (4.8)$$

This phase function is normalized if both f_d and f_p are normalized. The phase function is not reciprocal, but reciprocity is achieved due to $f(\omega \to \omega_o)\sigma_s(\omega) = f(\omega_o \to \omega)\sigma_s(\omega_o)$. Thus, our BSDF (4.1) is energy-conserving and reciprocal. In the following, we detail the scattering behaviour of both diffusers and platelets, and the implementation of our model.

4.4.2 *Scattering by Diffusers*

Following the measurements by Wang et al. [161], who analyze colloidal systems made of nanoscopic titanium dioxide particles, we use a mixture of phase functions to model the scattering of diffusers. This is common practice in computer graphics and related areas [32, 46, 193]. In particular, we model the scattering from diffusers using a mixture of two Henyey-Greenstein lobes $f_{HG}(\omega \to \omega_o|g)$ each parameterized by the mean cosine of the scattering angle g [60]. This is similar to previous work modeling the scattering of sunscreen lotions [117]. The resulting phase function is

$$f_d(\omega \to \omega_o) = w_g f_{HG}(\omega \to \omega_o|g_1) + (1-w_g) f_{HG}(\omega \to \omega_o|g_2), \quad (4.9)$$

with $w_g \in [0,1]$ the blending parameter between the two lobes.

4.4.3 *Scattering by Platelets*

To reproduce the glossy appearance required by a dewy finish, we use platelet particles, i.e., flat particles suspended in the medium that generate a glossy reflection. Platelets are purely reflective microflakes [73] suspended in the medium, following the SGGX distribution of normals $D_{SGGX}(\omega_m)$ [59], with ω_m the microflake normal. We assume a disk-like distribution of platelets, and parametrize $D_{SGGX}(\omega_m)$ by a roughness α_p parameter along the distribution's mean direction, and a rotation angle θ_p that rotates the mean direction of the distribution with respect to the tangent direction of the surface, so that the distribution does not need to be aligned with the surface normal.

The distribution of normals $D_{SGGX}(\omega_m)$ directly enables us to compute the projected area of the platelets, which we, as in previous work [58, 73], assume equal to $\hat{C}_p(\omega)$. As phase function, we opt for

a specular SGGX phase function without Fresnel effects, so that the phase function for platelets is defined by

$$f_p(\omega \to \omega_o) = \frac{D_{SGGX}(\omega_h)}{4\hat{C}_p(\omega)}, \tag{4.10}$$

with $\omega_h = (\omega + \omega_o)/\|\omega + \omega_o\|$ the half vector.

4.4.4 *Implementation & Properties*

We implemented our model in PBRT v4 [125] on top of the position-free Monte Carlo framework from Guo et al. [52]. This allows us to compute multiple scattering as an average of random walks inside the layer with next-event estimation for variance reduction, and to easily stack multiple layers of cosmetics. The source code, scenes and reflectance measurements are available on the project page `https://graphics.unizar.es/projects/CosmeticsAppearance_2024/`.

We compute Equation (4.1) using a Monte Carlo estimate, by randomly sampling paths starting at direction ω_i. We build the random walk by using exponential mean free path sampling with $\text{pdf}(s) = \sigma_t(\omega)\exp(-\sigma_t(\omega)\,s)$. A collision is found as long as the sampled distance s remains inside the layer. Otherwise, we move to the contiguous layer (the skin or outside). At each interaction inside the medium, we select a lobe (platelet or one of the two Henyey-Greenstein lobes) using Shirley's remapping [134] (with probabilities driven by c_d and w_g). Then, platelets are sampled using SGGX visible normals sampling [58], while Henyey-Greenstein phase functions are sampled using the usual CDF-inversion-based routine. Absorption is handled by multiplying the throughput by the single-scattering albedo (Equation 4.7) at each bounce. To reduce variance, we only use Russian Roulette as a path termination criterion after 128 bounces. The sampling routines and PDF functions are evaluated following PFMC [52], using a forward path sampling inside the medium, with PDF the probability density of generating the path.

4.5 ANALYSIS AND EVALUATION

In this section, we validate our model against measurements of cosmetics reflectance. We capture the reflectance from four liquid-based foundations from *Clarins*, with varying colors and finishes, from dewy to matte. In particular, we select *Skin Illusions 105 Nude* (Dewy 1), *Skin Illusions 112 Nude* (Dewy 2), *Skin Illusions Velvet 103 Nude* (Matte 1) and *Skin Illusions Velvet 108* (Matte 2). We show samples for each of them in Figure 4.4, top row.

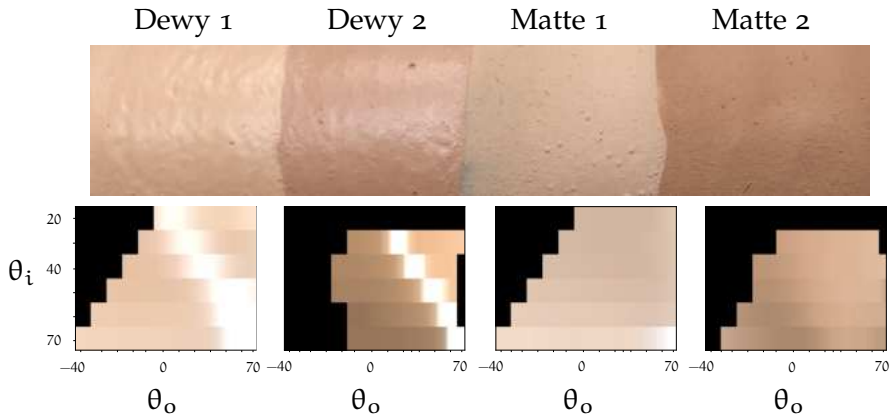

Figure 4.4: Measured samples (top row), wrapped around a cylinder for demonstration purposes. Reflectance profile measured with our setup (bottom row), with angles of observation θ_o on the horizontal axis and angles of incidence θ_i on the vertical axis. Negative angles of observation represent retro-reflectance configurations. Black pixel areas indicate that no information was available.

4.5.1 *Sample Preparation*

We captured the reflectances using a home-built setup, consisting of a gonioreflectometer, a light source (Xenon lamp emitting in about 6200K temperature), and an Ocean Optics spectrometer with fibre input and an attached collecting lens, as shown in Figure 4.5.

We directed a collimated beam with a diameter of 4 mm onto the sample. The direction of incidence was explored by rotating the sample holder, and the direction of observation by independently rotating the receiver's arm. Reflectance values were estimated by dividing the received spectral values by the signal reflected from a white reference, a 99% spectralon by Labsphere. Calibration with spectralon additionally compensates for the geometrical foreshortening [163]. We collected our measurements on a flat black slab made of matte polymer, which we found easier to calibrate than synthetic skin, and that simplified the layer beneath the cosmetic, which was useful for optimization. We could not directly measure the thickness of the samples, however, we performed several measurements on a silicon plate (mirror) to validate that we were in the multiple scattering regime. We added thin layers of the cosmetic product until we found no difference in measurements with respect to the number of layers.

In preparation for our samples, we applied a thick layer of cosmetic product on a black substrate. This is different from previous work [111], where measured cosmetics were applied on top of synthetic skin that might interfere with the cosmetic's reflectance data. We measure our samples in a semi-dry state, leaving them resting for an hour to allow

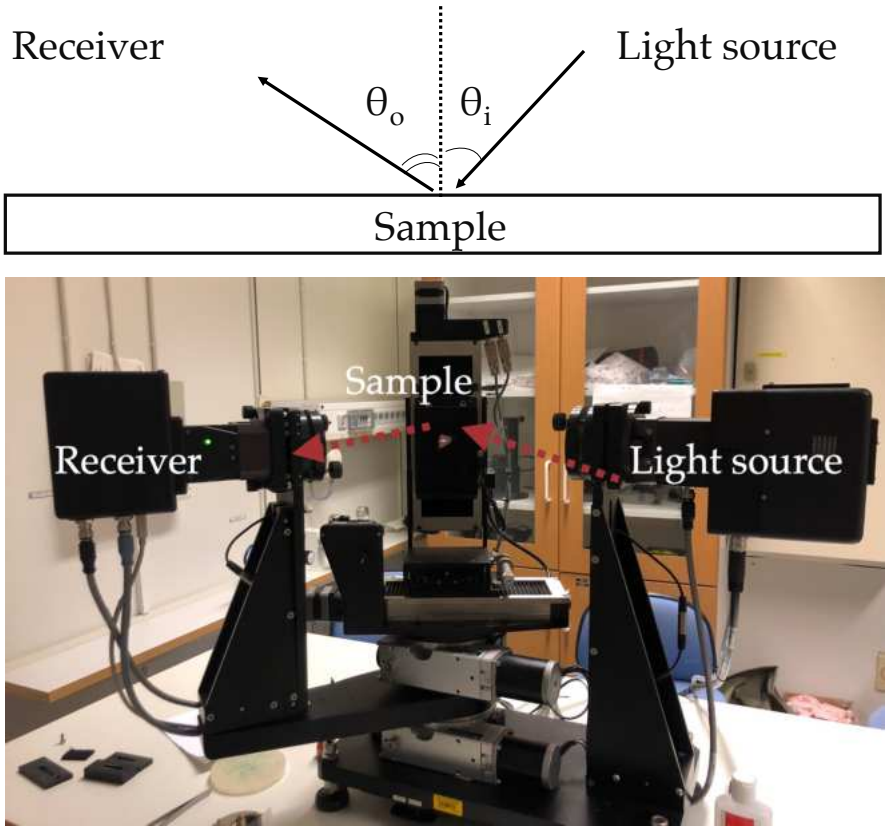

Figure 4.5: Experimental setup for measuring reflectance. We modify a commercial gonioreflectometer to collect spectral reflectance in non-specular directions.

the formation of a homogeneous layer. This resembles better the condition of a product when it is applied since usually a small quantity of product is spread over a comparatively large surface. Air exposition is likely to evaporate the product into a semi-dry state. This mechanism might also impact the hue of the product [175].

4.5.2 *Captured Data*

Figure 4.4 shows the captured data for our four liquid foundations. We plot measured data as sRGB- colored patches to better visualize the color and highlight shape changes. As we sparsely gather measurements we linearly interpolate between measurements and leave black pixels to represent lack of data. We measure both forward and backscattering for all products, although our setup does not allow us to measure for all light-view configurations, in some cases due to low a signal-to-noise ratio.

We only capture the inclination angle and not azimuthal data as our setup did not allow it. However, we believe that this is not a major issue since cosmetics are often applied on the skin without following any precise stroke direction, but rather in a circular manner, precisely to hide any anisotropy. Therefore, it is reasonable to assume that a small amount of reflectance changes occurs in the azimuthal plane and that most of the changes in appearance happen along the inclination angle.

As seen in Figure 4.4, the selected samples exhibit different reflectance behaviors: Dewy 1 and Dewy 2 displays a dewy finish, characterized by sharp highlights. Matte 1 can be considered an intermediate foundation, similar to a velvet finish, showing highlights for only grazing angles. In contrast, Matte 2, is clearly matte (absence of highlights). In all cases, we found some backscattering, in agreement with previous work [111].

4.5.3 *Comparison between model and captured data*

To analyze how accurately our model can represent the actual appearance of cosmetics, we fit our model to the measured data for each of the four samples, by solving

$$\underset{\boldsymbol{\pi}_i}{\operatorname{argmin}} \sum_{(\theta_i,\theta_o)\in M} d\left(I\left(\theta_i,\theta_o\right), f_s\left(\theta_i,\theta_o,\boldsymbol{\pi}_i\right)\right), \tag{4.11}$$

where $\boldsymbol{\pi}_i$ is the appearance model parameters (see Section 4.4), $I(\theta_i,\theta_o)$ is the measured data in linear RGB space at incoming angle θ_i and

outgoing angle θ_o, $f_s(\theta_i, \theta_o, \boldsymbol{\pi}_i)$ is our BSDF, and $d(\cdot,\cdot)$ is the L_2 distance metric. Our model is evaluated using Monte Carlo integration as described in Section 4.4. We use a derivative-free optimizer (modified Powell algorithms from the SciPy library); since this approach is sensitive to initialization we first perform a manual selection of the parameters and then use the optimizer to refine the solution. We use the L2 distance function in linear RGB space, although we show the results in sRGB space. We prepared the digital replica by setting the underlying layer as a black Lambertian surface and set the foundation layer thickness to 16 optical depths to enforce the multiple scattering conditions in which samples were taken. Computation-wise, we limit the number of bounces to 512, we then sample each direction 128 times. We evaluated this setup with preliminary experiments and found that it offered a good trade-off between time of execution and energy loss. We run the optimization described, allowing the model to optimize also for the IoR (initialized with 1.5) and surface roughness parameters (using the Trowbridge-Reitz distribution). At the end of the optimization cycle, we found values close to 1.0 for the index of refraction, thus supporting the validity of our interface-free simplification of the medium, which allows us to further reduce the number of parameters and reduces the computational cost by removing an interface from the computations.

Figure 4.6 shows the results of the optimization process for the four samples (last column), among the error measured under the L2 loss function. Our model captures the general behavior of the measured data in terms of reflected energy, color and highlight shapes. Some small differences are present in the intensity gradients of the diffuse part of the darker samples at grazing angles (Matte 2 and Dewy 2). We discuss these differences in Section 4.7.

Ablation study. We ran an ablation study of our model to examine the effect of its various components. Using the approach discussed above, we optimized three incremental versions of our proposed model: One composed of spherical diffusers only (Diffusers Only), one that is composed of platelets only (Platelets Only), and one that uses both particles but with a single lobe for the spherical diffuser particles (Full, Single Lobe). We initialize the optimization of each variation using the fitted parameters of our full model (Full, Two Lobes).

Figure 4.6 shows the results of this ablation study: It demonstrates that a model with only one particle type, either diffusers or platelets, is unable to properly reproduce the highlights of glossy appearances (Dewy 1 and Dewy 2). The reason is that one type cannot simultaneously generate highlights at grazing angles and in near-specular directions. In contrast, the combination of both particles with single-

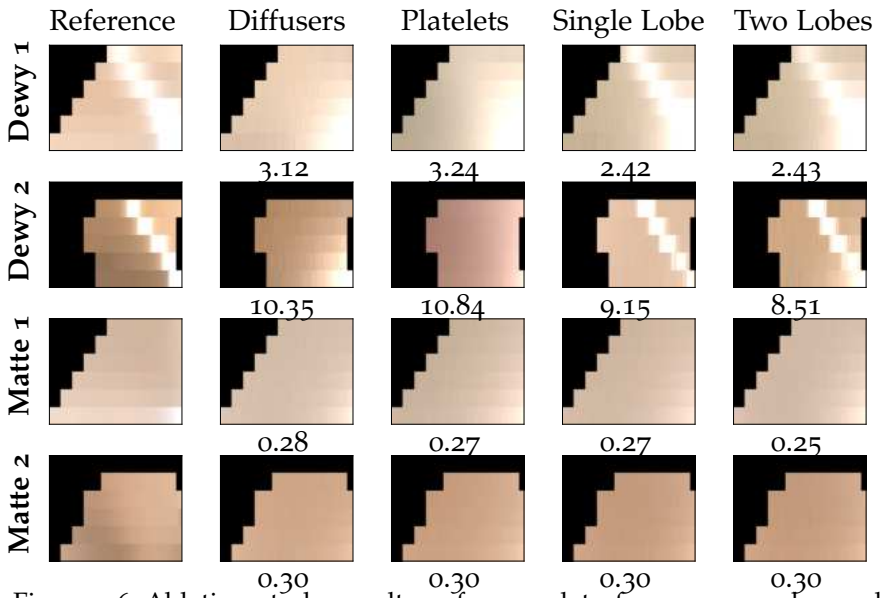

Figure 4.6: Ablation study results: reference data from measured samples (first column), media composed only of diffuser particles (second column), media made of only platelet particles (third column), media with both types of particles (diffusers and platelets) with a single lobe phase function and our full model (last column). For each configuration, we report the error under the L2 distance. Notice how the models using only one type of particle cannot approximate well both types of appearances (matte and dewy) and the full model overall exhibits the lowest error across all the products.

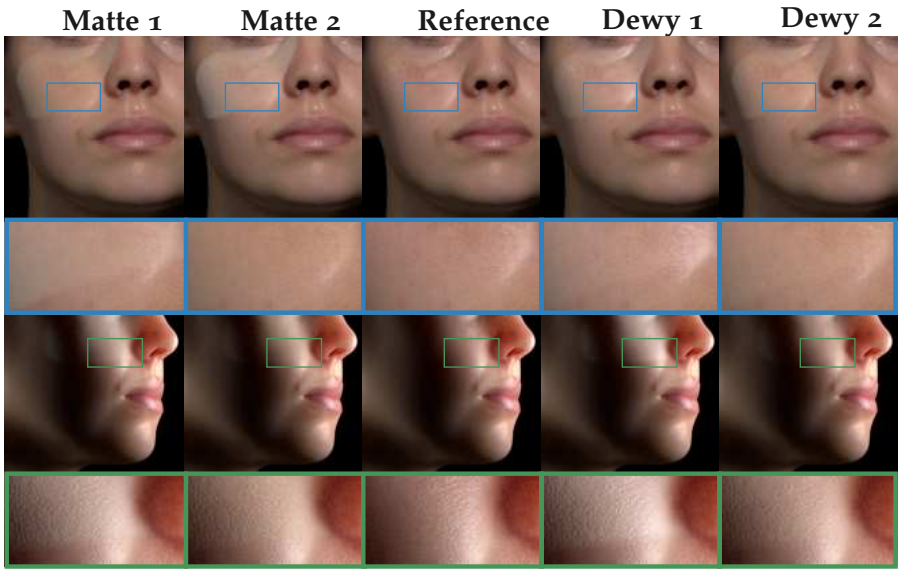

Figure 4.7: Analysis of our model applied over realistic skin. In the first row, we show the effect that cosmetics have on highlights. As can be seen in the insets (blue boxes), the matte cosmetics tend to reduce the brightness of highlights, while the two dewy products enhance them. In the second row, we show how a layer of cosmetics affects the subsurface scattering of the underlying skin. In each column, we apply the optical parameters retrieved for each product.

lobe diffusers generates results that are comparable with our full model, except for minor hue differences in Dewy 2. This suggests that a model with single-lobe diffusers could be sufficient to represent some real-world cosmetics, at the cost of losing expressivity, as we show in the next section.

4.6 RESULTS

In this section, we visually analyze our model in realistic use cases. We implemented our model as a layered material in PBRT v4 [125]. For the base skin, we use the random-walk-based default PBRT skin model. We first demonstrate our model using the realistic materials captured in the previous section; then we analyze the appearance space defined by the parameters of our model.

We report rendering times and sample counts, in addition to the user parameters obtained through optimization of the measured foundations, in Appendix A.

Figure 4.8: We compare renderings obtained with our model (right) with photographs (left) of cosmetics applied over bare skin on the forehead. In both renderings and pictures, we apply the cosmetic on the left side of the forehead, leaving the right side with bare skin for reference. Our model captures the subtle increase in reflectance when Dewy 1 is applied (central area of the forehead). On the other hand, the model is also capable of generating a matte appearance for grazing angles when Matte 2 is applied.

CAPTURED DATA Figure 4.7 shows our model with the parameters obtained from captured data, applied on top of the PBRT skin model. As expected, while the two dewy foundations enhance the highlights, matte foundations remove the highlights. Note how both dewy and matte foundations also slightly reduce the effect of skin subsurface scattering.

In Figure 4.8, we qualitatively evaluate our model against pictures of cosmetics applied on real skin. Our model reproduces the trends shown in the pictures: an increase in reflection when Dewy 1 is applied to the skin, and a more matte appearance, especially at grazing angles, for Matte 2.

APPEARANCE EXPLORATION Figure 4.9 (a) explores the effect of the concentration of diffusers c_d and the thickness t (in mean-free-path units). In this experiment, we use a single phase function for the spherical diffusers. Increasing the thickness reduces the effect on the appearance of the underneath layer, while increasing the concentration of platelets (smaller c_d) increases the glossiness of the skin. In contrast, when increasing c_d the appearance shifts to matte, as expected. The reason for brighter highlights with increasing thickness in dewy foundations was observed by Yoshida et al. [180], where the authors explained that multiple applications of cosmetics lead to an increase in the reflected light. We have to clarify that this is not necessarily a general characteristic of all cosmetics, but rather a behavior

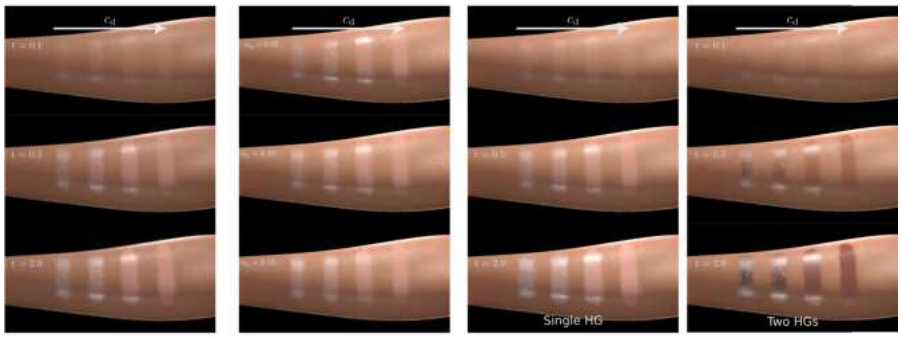

(a) Thickness vs Concentration (b) Roughness vs Concentration (c) single lobe vs two lobed

Figure 4.9: Appearance exploration: we investigate the influence of the parameters of our model on the final appearance. In (a) we show the influence of thickness t and concentration of diffusers c_d. Thickness has a major impact on perceived reflectance. In (b) we explore the visual impact of α_p, the roughness of platelets, and c_d on the shape and brightness of highlights. α_p mainly affects the shape of the highlights, while c_d alters their intensity. In (c) we study the effect of using a single or a two-lobed phase function for diffusers. Two-lobed phase functions generate darker and more saturated appearances.

that is shown by a certain subset of products.

In Figure 4.9 (b), we investigate the influence of c_d and α_p, the concentration of diffusers and the roughness of the platelets. We see that both parameters alter the perception of glossiness, although in different ways. While c_d affects the intensity of the highlights, α_p alters the shape of the highlights, going from sharper to broader highlights. Similar to before, these phenomena can be explained by observing that increasing c_d only decreases the chances of hitting a platelet, without altering the scattering behavior of the particle itself. On the other hand, α_p affects the scattering behavior of the particle, with rougher appearances obtained for bigger particles. We believe that these two parameters, c_d, and α_p can be helpful during editing, as they allow artists to edit two different dimensions of gloss perception, contrast, and sharpness of the highlight [124].

We investigate the influence of using one or two-lobed phase functions in Figure 4.9 (c) to see how t and c_d alter the appearance when diffusers are modeled with different phase functions. We observe that when diffusers are defined with a two-lobed phase function, the same parameters yield darker and more saturated colors. This can be explained by noting that when having two strongly anisotropic lobes, light tends to be either forwarded or backscattered, thus resulting in a darker appearance, since less light gets scattered horizontally.

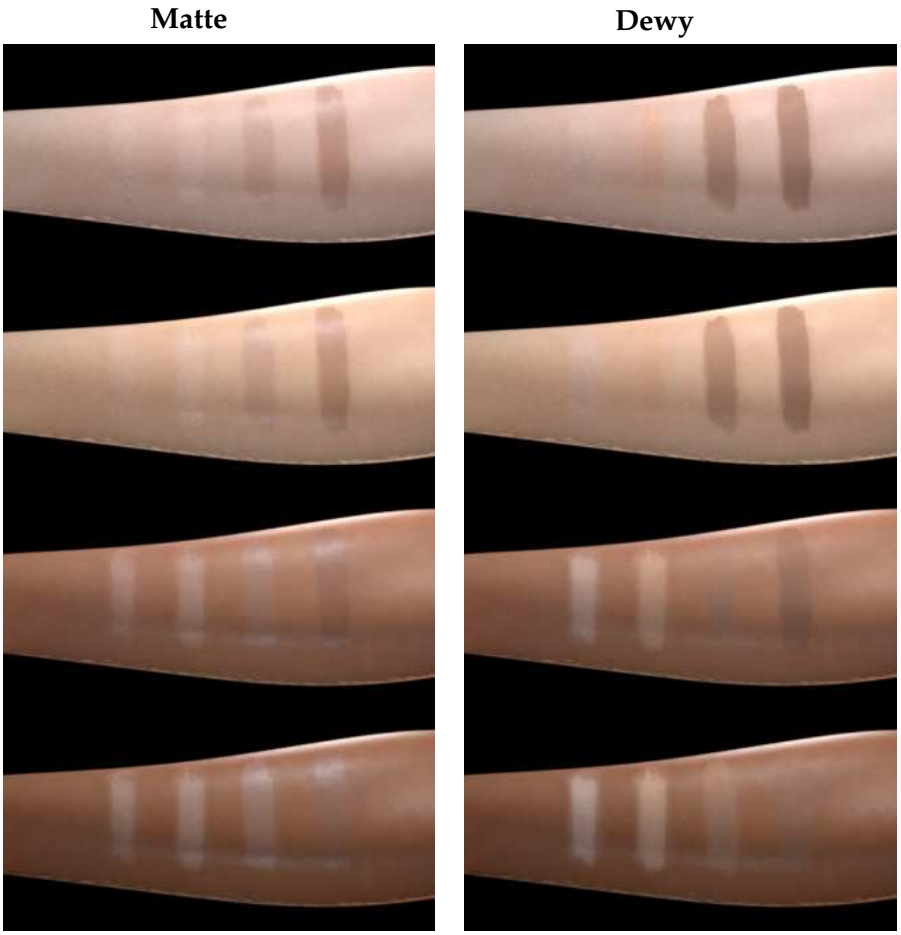

Figure 4.10: Experiment matching the hue of different skin types. In each row, we simulate different cosmetic strips aimed to match the hue of different skin types. We apply the same cosmetics to all rows changing the underneath skin type. Note how incorrect hues can be easily spotted if not applied to the correct skin type. We repeat this experiment for the two categories of matte and dewy cosmetics. All results are obtained using $t = 0.5$.

As expected, the influence of the skin layer is greater for small thickness values, while for higher values the appearance converges to a similar result, regardless of the appearance of the skin.

In Figure 4.10, we explore the capabilities of our model to reproduce the adequate hue for different skin types, for different product types. In each row, we apply four cosmetics strips, with only one of them matching the hue of the underlying skin type. This illustrates how a cosmetic product that does not match the hue of the underlying skin can be easily spotted. We run this experiment for both dewy and matte foundations, showing that our model is capable of generating an adequate hue for the different types of products. Matte cosmetics, as expected, provide a closer color match, while dewy foundations

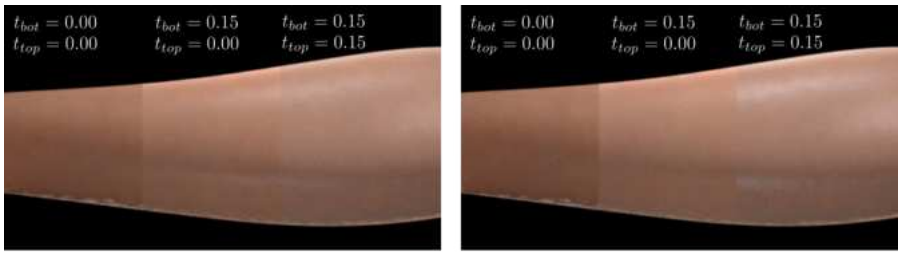

(a) bottom: dewy - top: matte (b) bottom: matte - top: dewy

Figure 4.11: Effect of stacking two layers of foundation. (a) The bottom layer uses a dewy foundation, while the top layer is composed of a matte foundation. In (b) the bottom layer uses a matte foundation, while the top layer is a dewy foundation. Note how the top-most material dominates the final appearance.

provide more desaturated colors in exchange for increased highlights. We also observe that the effect of glossiness is more prominent for darker skin tones, as observed in previous work on glossiness perception [124]. This is a key aspect that has to be considered for different skin types.

Finally in Figure 4.11, we explore the results of applying layers of foundations characterized by different final appearances. We run this experiment by taking dewy and matte foundation cosmetics and observing how they interact with each other depending on the order in which they are applied. We observe that the topmost layer dominates the final appearance. This is expected as the brightness of highlights is dominated by the first bounce, therefore the first few bounces are key in determining the final appearance.

4.7 CONCLUSIONS

We proposed a scattering model for characterizing cosmetic material using colored volumetric spherical diffusers and platelet particles. We demonstrated that this model is capable of reproducing the main characteristics of foundation layers by fitting the model to measured bidirectional reflectance data of sample products. We investigated the appearance space that our model spans, confirming that it is possible to achieve believable results with our model. As opposed to previous work, we offer a model that can be easily edited and used to predict different appearances without necessarily being entangled with the skin type on which it was applied. We believe that our model offers promising results, but additional work is required to capture all the subtle nuances of cosmetic materials.

Strictly speaking, our model focuses on foundation makeup, and we have only validated it against this type of cosmetics. However, as

shown in Figure 4.1, we can use our model to replicate the look of other types of makeup, which shows the versatility of our approach. Nevertheless, a more thorough analysis against measurements would be required for validating other ranges of cosmetics. Note also that the foundation samples are specific for light skin; however, as shown in Figure 4.10 our model is able to qualitatively capture the appearance of cosmetics targeting other skin types. Particularly interesting for future work is to investigate reflectance models for foundation layers that incorporate glittering effects. However, measuring this class of materials can prove to be a challenging task, as it is not clear how to measure the reflectance of a material that glitters if not by taking the aggregated behavior.

An additional limitation is that our model builds upon pure ray optics, and thus it ignores diffraction effects occurring due to the powder-like nature of the scatterers. That might explain why our model is not able to fully reproduce the reflectance behavior exhibited by Dewy 2, which we hypothesize is caused by the interference caused at grazing angles observed in previous work for different materials [35, 98]. Adding a diffraction reflection lobe [63] could help our model better fit the captured data and appearance behavior at grazing angles, and we think it is an interesting research direction for future work.

Studying the effect of heterogeneous and correlated scatterers is an interesting avenue for future work as concurrent work shows that varying pigments radius and mass fraction can have a significant impact on the colored appearance of cosmetics [152]. Nevertheless, we found that using the classical RTE formulation for uncorrelated media fits well with measurements, while it also reduces the additional complexity of specifying non-exponential mean-free-paths.

In terms of implementation, our model is based on the PFMC framework, which requires several samples to converge to a noise-free solution. Implementing our model using faster position-free strategies [16] or using the SpongeCake model [160] should be trivial, and would likely significantly reduce the overhead of our method. Finally, our model focuses on the local microscopic appearance of cosmetics, and thus does not account for the mesoscopic effects of cosmetics masking small crevices or pores which should change the normal or displacement mapping modeling of the skin mesogeometry.

5

A SURFACE-BASED APPEARANCE MODEL FOR PENNACEOUS FEATHERS

The appearance of a real-world feathers results from complex light interactions with their multi-scale biological structures, including the central shaft, branching barbs, and interlocking barbules. This chapter introduces a novel surface-based appearance model that captures these interactions using a BSDF that implicitly accounts for the far-field scattering effects of the shaft, barbs, and barbules. Each fiber is represented by Bidirectional Curve Scattering Distribution Function (BCSDF), incorporating the distinctive properties of barbs, such as their non-cylindrical cross sections and scattering media. To account for the occlusions between barbs and barbules, we derive an analytical masking term that computes their relative visibility based on the differential projected areas of their microgeometry. Unlike previous works, this approach employs a lightweight 2D texture representation, avoiding the need for explicit curve-based geometry for the fibers.

We show the flexibility and potential of the reflectance model to reproduce the most important visual features of several pennaceous feathers, including pigmentation, noniridescent structural coloration, and view-dependent effects. As a first author, I led the writing of the manuscript, modeling, implementation, and experiments of the reflectance model. This work first has been presented as a poster to SIGGRAPH 2024, and later has been accepted for publication in the Computer Graphics Forum and presented at the 32th Pacific Conference on Computer Graphics and Applications (Pacific Graphics 2024).

J. Padrón, D. Lanza, A. Jarabo & A. Muñoz
A Surface-based Appearance Model for Pennaceous Feathers
Computer Graphics Forum (PG 2024)

5.1 INTRODUCTION

Feathers are the distinctive characteristic from birds, and are unique structures not shared with any other animal. They are crucial for flying, but also allow birds to control their body temperature, camouflage, and they are fundamental for communication in mating, aggression and dominance [61].

The appearance of feathers is varied and rich, different among species, and is partially explained by the geometrical complexity of their structure at several levels: Each feather is composed of a central shaft, called the rachis, with its base (the calamus) is inserted to the skin. Serial fiber-like branches (barbs) emerge from both sides of the rachis. A second level of branching emerges from the barbs (the barbules), which in pennaceous feathers become attached to adjacent barbs, forming a flattened surface (the vane). Depending on the structure formed by barbules, feathers can have both pennaceous and plumulaceous sections. When barbules are interlocked to adjacent barbs, they create a tense and semi-rigid surface, characteristic of pennaceous areas. When barbules are loose, they form a fluffy, irregular volume typical of plumulaceous sections. Each of the barbs and barbules components possesses a scattering microstructure and nanostructure that greatly affects appearance: Different pigments (carotenoids and melanin) produce coloration through spectral absorption, while barbs have a multilayered structure with an inner scattering medulla which in some species have a quasi-ordered nanoscopic structure producing diffuse structural coloration. Photonic glass-like special nanostructures (e.g., grids of melanin rods) are responsible for the spectacular iridescent patterns in feathers of birds such as the peacock or the bird of paradise. It is only the aggregated behavior of light-matter interactions at these scales that produce the complex appearance of feathers. Beyond direct applications for traditional computer graphics applications, the appearance of feathers has also been studied for ornithology [61], paleontology for color reconstruction of extinct dinosaur feathers [185], or fabrication of new biomimetic materials [38].

Compared to other biological appearances such as skin [31, 70, 139], hair [103] or fur [172, 173], rendering of feathers, and in particular pennaceous feathers, is a relatively unexplored area in computer graphics, with some notable exceptions that either oversimplify the appearance [144], bake it in a Bidirectional Texture Function (BTF) [22], focus on specific bird species [66], or use expensive curve-based representations for the barbs with simplified fiber scattering functions [6]. While modeling the barbs as curves [6, 66] is flexible, allows for a very fine-detailed representation of the feathers, and explicitly accounts for geometric effects such as visibility, it might become very expensive when representing many feathers, quickly becoming impractical in most applications.

In this work we propose a far-field surface-based appearance model for pennaceous feathers, that encodes the geometric complexity of the feather by using lightweight textures, and that it is able to correctly predict the geometric attenuation that so far could only be modeled with explicit curve-based feathers. At the core of our model is a new

BSDF that accounts for the scattering of barbs and barbules stochastically, based on their density and orientation, as well as their relative visibility. Inspired by previous works [6, 66, 195], we model the individual scattering of both barbs and barbules using a fiber-based BCSDF. However, as opposed to these previous works, our BCSDF accounts for the ellipticity of the fibers and the effect of the internal non-centered scattering medulla, which are crucial for the appearance of most feathers, specially bright colored feathers.

We demonstrate our work representing a wide baseline of feather appearances, including pure white feathers, blue feathers due to diffuse structural coloration, or feathers with color resulting from hybrid coloration. None of these can be represented with previous models. In particular, our contributions are:

- A flexible BSDF that models the far-field appearance of non-iridescent pennaceous feathers,
- an elliptical BCSDF that generalizes previous curve scattering models by accounting for both elliptical cross-section and the presence of a non-centered scattering medulla,
- and an analytic masking term that combines the relative contribution between barbs, barbules, and transparency based on their differential projected areas.

Figure 5.1: A rendering of the wing of an *Amazon parrot*. **Left:** Bird model with a baked texture from a reference photograph of an Amazon parrot. Notice how the baked texture looks flat. **Center:** A surface-based rendering of the wing feathers, using a hair model [103] for representing the scattering from the microscopic structures of the wing, similar to previous approaches [6, 53]. **Right:** The same scene with feathers rendered using our model accounting for accurate masking and complex medulla using our BCSDF. Our far-field reflectance model represents more accurately the feather substructures and coloration mechanisms, given a closer appearance match with the baked texture overall appearance, including features such as the diffuse look of feathers, and the subtle goniochromatism due to visibility changes between barbs and barbules.

Figure 5.1 shows a practical example with a feather wing and a comparison to previous work. The source code and scenes are available on the project website together with an interactive comparison (https://graphics.unizar.es/projects/FeathersAppearance_2024/).

5.2 RELATED WORK

FEATHER APPEARANCE The modeling of the appearance of feathers remains a relatively unexplored area of research. Most of previous works focus on the modeling of the geometry of the feather, defining parametrical models that simulate the geometrical structure of each feather. Rachis and barbs have been modeled using NURBS and structured in feathers using L-Systems [22], and Bezier curves both for the structure of feathers and for individual barbs [22, 144]. Data-driven approaches based on images of real feathers have been able to model not only rachis and barbs but also barbules [7, 8]. Lately, a generative algorithm based on the biological growth of feathers has been able to model realistic feathers with three-dimensional features [186]. These works are orthogonal to our work, and could be used for generating our surface-based representation described in Section 5.6.2.

Regarding appearance modeling, Chen et al. [22] proposed to use data-driven appearance based on BTFs, which require the capture of the feather and has limited angular resolution. Haapaoja and Genzwürker [53] and Leaning and Fagnou [90] modeled the scattering from barbs using a hair BCSDF [103], but ignored the scattering from barbules. Harvey and colleagues [56] proposed a data-driven model for the African Emerald Cuckoo, based on measured data and expensive wave simulations. Closest to our work, Huang et al. [66] and Baron et al. [6] accounted for the scattering of both barbs and barbules, with the former modeled statistically. In particular, Huang and colleagues [66] focused on the iridescent appearance of plumaceous rock dove neck feathers, proposing a BSDF for explicit barbs that simulates barbule scattering using a microfacet-like model with thin-film iridescence, while accounting for inter-barbule masking. In contrast, our work focuses on general non-iridescent pennaceous feathers. Baron et al. [6] focus on general feathers, representing barbs as curves where the BCSDF combines the scattering of both barbs and barbules, using Marschner's hair model [103]. In contrast, our model is a general, compact surface-based representation for pennaceous feathers, where the scattering of both barbs and barbules is modeled using a new BCSDF that accounts for elliptical cross-sections and inner scattering medulla allowing to represent a wider range of light-matter interactions occurring at barb and barbule scale.

MICROSTRUCTURE-BASED SURFACE SCATTERING Statistical aggregated representations of the detail at the microscopic level are the common choice for representing the scattering of small features. The most common approaches are microfacet models [25, 74, 158] that represent rough surfaces as statistical aggregates of tiny planar surfaces, generally assuming uncorrelation for computing the geometric attenuation [57]. Other approaches assume other microscopic scatterer shapes, including spherical scatterers [194], bumps and cavities [109], scratches [17], or micrograins [99], which allow computing specific geometric attenuation terms. Closer to our work, far-field models for woven cloth [71, 128] assume a particular structure between perpendicularly interwoven yarns with fiber-like scattering; this structure allows to derive a closed-form masking functions between the different yarns. Our model also models the scattering of each component using a BCSDF, but incorporates the additional complexity of the multiscale structure of barbs and barbules.

SCATTERING FROM FIBERS Cylinder-based scattering models based on the BCSDF have been proposed for realistic human hair for circular [23, 103, 195] and elliptical fiber cross sections [14, 65, 84]. Follow-up work extended hair models to fur, by adding a scattering medulla crucial for the soft look of fur [172, 173]. Cloth fibers and yarns have also been represented using the BCSDF, either measured with goniorreflectometers [128] or simulated from the microgeometry of the fibers [2, 168]. To reduce the cost of rendering individual fibers, aggregation techniques have been proposed to approximate the aggregated appearance in fur [190] and cloth fibers [83]. Our model for fiber scattering builds upon these models, but generalized to the specific structure of the barbs and barbules that compose the feather, combining elliptical cross-sections with a non-centered scattering medulla.

5.3 OVERVIEW

The scattering of each barb and barbule is modeled as a BCSDF [191], which assumes that each fiber is an infinite locally-straight cylinder (Section 5.5). The aggregated appearance comes from combining such BCSDFs in their local frame, as obtained from the tangent map and the geometrical parameters of the BSDF. The scattering radiance from each BSDF is weighted based on the corresponding projected visible area as defined by our masking term (Section 5.6). Masking is computed on the fly when our feather BSDF is evaluated or sampled. The structural and optical parameters of our model can affect either particular BCSDFs (for barbs or barbules), the global BSDF or both. These are summarized in Table 5.1 and some of them are illustrated in Figure 5.2. The feather's geometry is encoded in a 2D texture applied on a plane or curved plane: The red channel encodes the barb orienta-

tion and the blue channel stores a flag identifying rachis, vane, and background. We manually designed the texture to roughly match the feathers' silhouette based on feather photographs. More details about the authoring process can be found in the Appendix B.

Parameter	Definition
β_m	Longitudinal roughness of cortex
β_n	Azimuthal roughness of cortex
$\sigma_{c,a}$	Absorption coefficient in cortex
η_c	Refractive index of cortex
a_c	Cortex semi-major axis
b_c	Cortex semi-minor axis
$\sigma_{m,a}$	Absorption coefficient in medulla
d_m	Diffuse reflectance of medulla
η_m	Refractive index of medulla
a_m	Medulla semi-major axis
b_m	Medulla semi-minor axis
$(c_{m,a}, c_{m,b})$	Medulla center (w.r.t. to cortex center)
ϕ_b	Azimuthal barb angle
ϕ_{bb}	Azimuthal barbule angle
θ_{bb}	Longitudinal barbule angle
δ_{bb}	Barbule separation
l_{bb}	Barbule length

Table 5.1: Parameters of our Feather BSDF. The angles (ϕ_b, ϕ_{bb}, θ_{bb}) are expressed in degrees. The sub-index b refers to barbs, while the bb refers to barbules. l_{bb} and δ_{bb} are measured in number of barb and barbules per length unit respectively. The eccentricity for e_b and barbules cross section e_{bb} are computed from the cortex axes a_c and b_c of the corresponding internal structure.

We introduce the following assumptions:

1. No wave-optical effects are present between barbs and barbules, and all scattering can be considered in the ray-optics regime. Wave optics is particularly significant for iridescent feathers such as the hummingbird and peacock feathers. In this work, we focus on pennaceous non-iridescent feathers which extend a large group of feathers.

2. As previous work [66], we assume an elliptical cross-section of both barbs and barbules. While this is mostly accurate for barbs, barbules come in different shapes, which are specially relevant for iridescent feathers [56].

3. Multiple scattering only occurs inside the fibers (accounted by the BCSDF), but not among barbs and barbules on the same surface. When rendering (path tracing), multiple scattering emerges from the interactions among different surfaces.

4. We assume that shadowing has a negligible effect, which allows our model to compensate for energy loss due to the lack of multiple scattering among barbs and barbules.

5. The microstructure of the feather's vane is locally regular: In a differential surface patch, barbs are parallel, proximal barbules are parallel and distal barbules are parallel. This removes the need of explicitly modeling the geometry of all barbs and barbules.

In the following, we first define our new BCSDF that supports some of the observed structural properties of both barbs and barbules; then, we define our surface BSDF that leverages the BCSDFs for modeling the aggregated scattering at the feather's vane.

5.4 ON THE APPEARANCE OF FEATHERS

The appearance of feathers is the result of a complex light-matter interactions at multiple scales. It depends on both internal structure and chemical composition. The structure and type of feather affect its appearance at a high level, while the chemical composition and micro-nanoscale structure fundamentally change its coloration, opacity and reflectance.

5.4.1 *Structure*

Although feathers are incredibly diverse in shape and size, they are all composed primarily of keratin, a protein present in all epidermal structures of all vertebrates. Unlike the epidermal structures of mammals (e.g. hair or nails) whose main component is *α-keratin*, the structures of birds and reptiles are based on *β-keratin*, which makes them more rigid. This protein is present in all the epidermal structures of birds (beak, claws, feathers ...) in different ways depending on the corresponding biological functions. The microstructure of *β-keratin* on feathers is, biomechanically, more flexible, providing unique properties required for flight [122].

Feather structure. The main components of a typical feather consist of a long and central axis in which two parts are considered: the lower and wider part, which is inserted into the skin (**calamus**) and the rest of the axis (**rachis**). On both sides of the rachis, the **vane** grows as a lamina and is formed by **barbs**, which grow along the

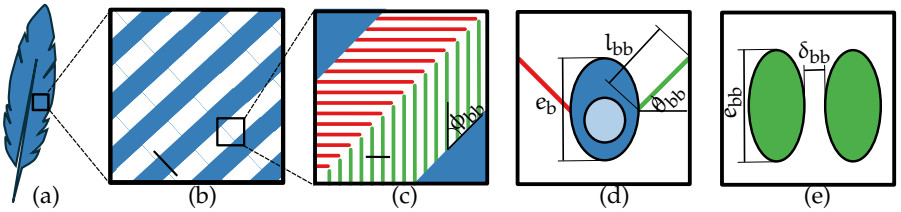

Figure 5.2: (a) The appearance of the feather's vane (a) depends on its underlying structure. (b) Parallel barbs emerge from the rachis. (c) Each barb branches into two sets of barbules, proximal and distal. (d) Barbs are modeled as infinite cylinders with elliptical cross section, with an inner medulla with elliptical cross section. Barbules' thickness is negligible so at this level they are modeled as the plane in which they lie. (e) At a smaller scale, barbules are also cylinders with elliptical cross section, and can occlude each other. They have some spacing between them that at a larger level is treated as partial transparency that is considered at a larger (barb) scale. The microgeometrical parameters of our model are also represented.

entire rachis in a branching manner. Each barb consists of a central axis of tens of microns (**ramus**), which branches out on both sides in rows of hundreds of microscopic-sized **barbules** (**proximal** and **distal**), coupled by hooklets [56, 145]. Barbules are up to an order of magnitude smaller than barbs [66], and branch from their respective barb, often in a $\phi_{bb} = 45°$ angle to maximize their overlap, favoring the grip of the hooklets [33]. This ramification results in features at multiple scales (see Figure 5.2). Previous work [7] collected data from ornithological studies including barb density, barb angles or barbule length. There is an important variety of geometric structures and configurations for barb and barbules depending on the bird species and even sex [105]. For instance, some cross sections such as the barbule cross-section shapes of a peacock tail feather (see Figure 3 in Freyer et al.'s work [40]) or a Lawes' parotia breast feather (see Figure 3 in Stavenga et al.'s work [140]) with ridged forms. Nevertheless, the cross sections of these internal structures tend to be elliptical (see Figure 4 [105]) as we show in the scanning electron microscopic (SEM) images of the kingfisher feather (see Figure 5.3, c), with eccentricity up to 6 depending on the specie [69]. For this reason, as previous work [66], we approximate these cross sections as ellipses.

Feather taxonomy. Feathers can be classified according to size, shape, and type [143]. One of the main features is the type of vane: **plumulaceous** (fuffy, diffuse and soft) or **pennaceous** (mostly flat, firm and rigid, due to interlocked barbules). In this work, we focus on pennaceous feathers, as these ones can be modeled with a BSDF over a surface that represents the vain. A surface representation allows us to encode the feathers as texture, a representation quite effective especially

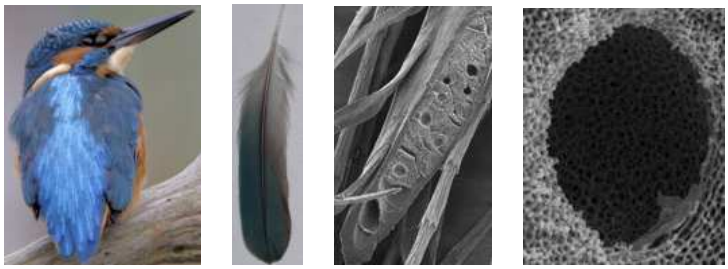

(a) (b) (c) (d)

Figure 5.3: (a) Kingfisher (*Alcedo atthis*). (b) Blue tail feather of a kingfisher. (c) Top-view SEM of a sectioned barb of the feather with several barbules (50 µm). (d) Cross section SEM of a cut vacuole and the surrounding spongy structures (2 µm). Notice the elliptical shape of the barb cross section and the presence of the medulla with an internal spongy structure (Source [141]).

for far field scenarios. On the other hand, plumulaceous feathers require the modeling of individual barbs over a volume. For a further discussion about the feather taxonomy and potential representations, we refer the reader to previous work specialized on feather geometry [8, 143].

5.4.2 *Coloration*

Feathers combine pigmentation and structural coloration to create extraordinary and diverse colors, more than for any mammal and most vertebrates [62]. The colors of the bird feathers play an essential role in a variety of biological functions such as camouflage, visual signaling or mating [127].

Pigmentation. Pigment-based coloration is the most common in vertebrates and is caused by the absorption of certain wavelengths as light traverses the pigments (Figure 5.4, left). Pigments are molecules that absorb and reflect each of the wavelengths of light, hence they can be associated with a particular color. These pigments are deposited between the keratin sheets that make up the barbs, barbules and rachis [127]. The most prevalent pigments in feathers are based on melanin, which is responsible for a wide range of colors, usually brown, gray and black tones [133]. or carotene, that produce more vivid colors such as reds, yellows, and oranges [107, 114, 127, 133].

Structural coloration. The structural coloration of bird feathers is caused by the scattering and interference of light with the feather nanoscopic structure [41]. This coloration does not depend entirely on absorption, but on the way the structure of the feathers disperses certain wavelengths. One source of such structural coloration are spe-

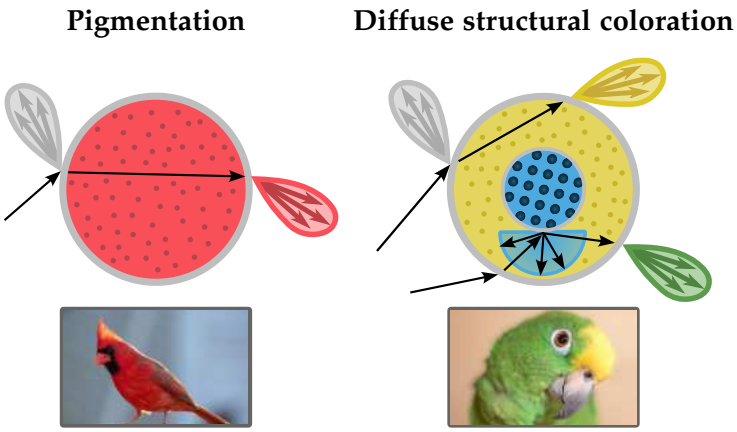

Figure 5.4: Cross-section fiber schematic of the coloration mechanisms in feathers supported by our appearance model. **Left**: Pigments-based coloration where some wavelengths are absorbed by the pigment granules located in the keratin matrix. **Right**: Diffuse structural coloration, where in addition to pigmentation, the medulla scatters colored light due to interference.

cialized keratin structures in the medulla of the barbs, which create a pseudo-ordered matrix of keratin and air bubbles, known as the spongy layer (see 5.3, d). These lead to non-iridescent tones of blue, violet and UV [126], as illustrated in 5.4, although in some cases they generate partial iridescence for highly directional illuminations [141], which disappears with lower frequency illuminations. We account for this effect with a diffuse medulla, that approximates the backscattering given by constructive interference in such quasi-ordered structures [118].

Hybrid coloration Some colors such as blues, greens and purples are created by the combination of the structure and the pigments. For instance, the green color is usually a combination of yellow pigmentation with a blue structural color [107] (5.4, right). Feather goniochromatism can occur from the partial occlusions between barbs and barbules of different colors at different view orientations, which we model through a masking expression.

5.5 SCATTERING FROM BARBS AND BARBULES

In this section, we model the scattering of the main individual components of the feather as a BCSDF. Then, we describe our structural model for barbs and barbules; then, we describe the BCSDF used for

modeling the three of them. Following the formulation from [103], we define the far-field BCSDF in polar coordinates, as

$$S(\phi_i, \theta_i, \phi_o, \theta_o, h^-, h^+) = \frac{D(\phi_i)\cos(\theta_i)^{-2}}{h^+ - h^-} \int_{h^-}^{h^+} S(\phi_i, \theta_i, \phi_o, \theta_o, h) dh, \tag{5.1}$$

where (ϕ_i, θ_i) and (ϕ_o, θ_o) parametrize in polar coordinates the incident and outgoing direction respectively, $D(\phi_i)$ is the projected fiber width on the incident direction, $\cos(\theta_i)^{-2}$ accounts for the projected solid angle of the specular cone, h^- and h^+ parametrize the limits of the visible fiber diameter (for a fully visible fiber, $h^- = -1$ and $h^+ = 1$), and $S(\phi_i, \theta_i, \phi_o, \theta_o, h)$ is

$$S(\phi_i, \theta_i, \phi_o, \theta_o, h) = \iint \mathcal{S}(\phi_i, \theta_i, \Phi, \Theta, h) G_M(\Theta - \theta_o | \beta_m) \\ G_N(\Phi - \phi_o | \beta_n) \cos(\Theta) d\Theta d\Phi, \tag{5.2}$$

where $G_M(\Delta\theta|\beta_m)$ and $G_N(\Delta\phi|\beta_n)$ are longitudinal and azimuthal Gaussian detector functions respectively [195], that regularize the scattered field accounting for surface roughness (parametrized by β_m and β_n, respectively). Finally, $\mathcal{S}(\phi_i, \theta_i, \Phi, \Theta, h)$ models the transfer function inside the fiber, defined as the integral of paths starting at (ϕ_i, θ_i, h) and outgoing at direction (Φ, Θ) following the path integral [154]

$$\mathcal{S}(\phi_i, \theta_i, \Phi, \Theta, h) = \int_\Omega f(\mathbf{x}) d\mu(\mathbf{x}), \tag{5.3}$$

with Ω the space of paths $\mathbf{x}$ that start at (ϕ_i, θ_i, h) and end at (Φ, Θ), and $\mu(\mathbf{x})$ the measure of the integral. For purely absorbing fiber, the space of paths starting at (ϕ_i, θ_i, h) is a singular specular path, and thus $\mathcal{S}(\phi_i, \theta_i, \Phi, \Theta, h)$ is a sum of impulse functions, one per bounce inside the fiber, with amplitude the attenuation at each bounce.

5.5.1 *Fiber models*

We do not model the scattering from the rachis as a BCSDF; instead, we assume that the diffuse scattering medulla is dominant and model it as a colored diffuse surface. We model **barbs** and **barbules** as cylindrical β-keratin cortex with elliptical cross section, with axes a_c and b_c. The interface is a rough dielectric, with roughness modeled as azimuthal and longitudinal 1D Gaussian detectors as described above), and index of refraction η_c. The β-keratin hosting medium is filled with absorbing pigments, leading to an exponential transmittance as predicted by Beer-Lambert law.

Additionally, the barb contains a **medulla**. As opposed to hair and fur models [173], the medulla is generally not aligned with the cortex

center, nor have the same eccentricity. We thus do not model cortex and medulla as concentric cylinders, but instead allow the medulla to position freely inside the cortex, with axes a_m and b_m and center $(c_{m,a}, c_{m,b})$. As anticipated before, we approximate the reflectance of the medulla as a diffuse surface. The albedo ranges from white (when there is no spongy layer) to blue, representing the non-iridiscent coloration of the spongy layer (as described before). We use measured reflectances for the blue tint, from the work by Noh et al. [118].

5.5.2 *Rendering*

Our model for barbs and barbules involves elliptical cross sections and a diffuse medulla (for the case of barbs), so our solution is not simple enough for a closed-form expression for Equation 5.1, especially as we account for higher-order bounces inside the fiber. Thus, we need to solve the integral numerically. Inspired on the work of Chiang et al. [23] we leverage the stochastic nature of modern renderers and compute the nested integrals in Equation 5.1 with a Monte Carlo estimate.

We implement a stochastic Monte Carlo-based path tracer from which we obtain a set of fixed number of *lobes*. In our experiments, we observed that five lobes seem to be accurate enough, as we shown in Figure 5.13. Each of these lobes consists of an outgoing radiance value (throughput) associated to an outgoing direction. Each interaction with each dielectric interface (cortex) deterministically generates two rays: one exiting the cortex, which we store as a lobe, and one entering the fiber, which keeps interacting and generating lobes until the final number is reached. The stochastic exploration of those sets of lobes comes from the integration variable of Equation 5.1 h and, in the case of barbs, the interactions with the medulla, from which we generate new rays using cosine sampling.

For **evaluating** the BCSDF, we go through all the lobes, evaluating the Gaussian detector functions $G_M(\Theta - \theta_o|\beta_m)$ and $G_N(\Phi - \phi_o|\beta_n)$ (see Equation 5.2) for the direction of the lobe (Θ, Φ), and $S(\phi_i, \theta_i, \Phi, \Theta, h)$ is a one-sample estimate of the lobe's throughput. For **sampling** the BCSDF, we follow a strategy similar to previous works [195] where we build a discrete pdf where the accumulated throughput of each lobe corresponds to the probability of such lobe.

5.6 OUR SURFACE APPEARANCE MODEL

Unlike previous works [66] that explicitly model the rachis and barbs as curves, we represent feathers using a surface-based representation, where the geometry explicitly model the rachis and vanes, while barbs and barbules in the vanes are modeled as microgeometry, using a BSDF defined in the local coordinate system of the barbs. As described before, we encode the feather parameters in texture space, using a mask to distinguish between rachis and vanes, and defining the local tangent direction on the surface using a rotation angle. This removes the need of modeling explicit geometry of the feather, resulting in a compact representation.

Our BSDF $f_s(\omega_i, \omega_o)$ is a linear combination of four different components: barb BCSDF S_b and proximal and distal barbules BCSDFs S_{bb} modeled using Equation 5.2 (below in Cartesian coordinates instead of polar), and transmittance through the vane. The BSDF is defined in the local coordinates of the barb, defined by the normal of the surface and the barb's tangent direction, following

$$\begin{aligned} f_s(\omega_i,\omega_o) = \Big[& w_b(\omega_o)\, S_b\left(\omega_i, \omega_o, h_b^-(\omega_o), h_b^+(\omega_o)\right) G(\omega_i) \\ & + w_{bp}(\omega_o)\, S_{bb}\left(\mathbf{T}_{bp}\omega_i, \mathbf{T}_{bp}\omega_o, h_{bp}^-(\omega_o), h_{bp}^+(\omega_o)\right) G(\mathbf{T}_{bp}\omega_i) \\ & + w_{bd}(\omega_o)\, S_{bb}\left(\mathbf{T}_{bd}\omega_i, \mathbf{T}_{bd}\omega_o, h_{bd}^-(\omega_o), h_{bd}^+(\omega_o)\right) G(\mathbf{T}_{bd}\omega_i) \\ & + w_t(\omega_o)\, \delta(1-\omega_i\cdot\omega_o)\Big] |\omega_i\cdot\mathbf{n}|^{-1}, \end{aligned} \tag{5.4}$$

where $\mathbf{n}$ is the surface normal, $w_b(\omega_o)$, $w_{bp}(\omega_o)$ and $w_{bd}(\omega_o)$ model the projected area of the barb, proximal barbule and distal barbule as viewed from ω_o, respectively, $w_t(\omega_o) = 1 - (w_b(\omega_o) + w_{bp}(\omega_o) + w_{bd}(\omega_o))$ is the amount of transparency, $\delta(\cdot)$ is the Dirac delta distribution, $\mathbf{T}_{bp}$ and $\mathbf{T}_{bd}$ transform the coordinate system to the frame of proximal and distal barbules, according to their rotation $\phi_{bb} = 45°$ and inclination θ_{bb} (parameter of our model), and $G(\omega_i) = \cos(\theta_i)$ the foreshortening over the fiber. The integration ranges for the corresponding BCSDFs are $[h_b^-(\omega_o), h_b^+(\omega_o)]$, $[h_{bp}^-(\omega_o), h_{bp}^+(\omega_o)]$ and $[h_{bd}^-(\omega_o), h_{bd}^+(\omega_o)]$. Both the projected areas $w(\omega_o)$ and the integration ranges (h^-, h^+) for barb and barbules are given by our masking term (Section 5.6.1). Finally, note that for all BCSDFs we set the fiber width $D = 1$, since it is accounted for by the projected areas w_b, w_{bp} and w_{bd}, respectively.

5.6.1 *Masking*

We do not explicitly model the feather's microgeometry, but instead devise an analytical masking expression that analyzes the visibility

among its components. Our masking expression works at two different scales: barbs and barbules. The critical insight for developing our masking components is that, at their respective local coordinate systems, all the microgeometrical elements are either ellipses or segments. Both are governed by implicit and parametric equations from which we can derive both projected areas within a parameter subrange. Furthermore, instead of stochastically explore the visibility, as the work by [66] does for barbules, we find analytical points that correspond to visibility discontinuities by tracing 2D rays at the analytical boundaries, and from the arcs/segments between the corresponding intersections we calculate projected areas.

We name $\omega'_o = \{\omega'_{ox}, \omega'_{oy}\}$ the two-dimensional direction in the local coordinate space (the longitudinal dimension is ignored) after transforming ω_o. For an ellipse (representing barb or barbule) with center $\mathbf{c} = \{c_x, c_y\}$ and axes a_x and a_y the visibility discontinuities as given by that ellipse are its tangent points, obtained as:

$$\mathbf{p}_{t0} = \begin{pmatrix} c_x + a_x \cos(\alpha) \\ c_y + a_y \sin(\alpha) \end{pmatrix} \qquad \mathbf{p}_{t1} = \begin{pmatrix} c_x + a_x \cos(\alpha + \pi) \\ c_y + a_y \sin(\alpha + \pi) \end{pmatrix} \tag{5.5}$$

where $\alpha = \tan^{-1}\left(\frac{-a_y \omega'_{ox}}{a_x \omega'_{oy}}\right)$.

For barbs, the corner among barbule segments $\mathbf{p}_c$ represents a visibility discontinuity too. These visibility boundary points are the origin of 2D rays traced towards the rest of the elements of the microgeometry at their specific scale. Once the visibility among the different geometrical elements, projected areas towards ω'_o are calculated through a simple cosine for the case of segments and for the case of ellipses, its projected area A is:

$$A(u_0, u_1) = \omega'_{ox} a_y (\sin(u_0) - \sin(u_1)) + \omega'_{oy} a_x (\cos(u_1) - \cos(u_0)) \tag{5.6}$$

where u_0 and u_1 are the starting and ending parameters from the ellipse's parametric equation, obtained by inverting the parametric equation for the intersection (visibility boundaries) points. The derivation of this inversion and of Equation 5.6 can be found in the supplemental material.

Barbule masking At a smaller scale, which we call *barbule masking* we align the reference frame at the local barbule frame. Given the cross section of barbules (ellipses) and a separation among them, we obtain the ratio between barbule visibility and transparency, as well as the casting segment range for the barbule (see Figures 5.2 and 5.5). This is done at the local coordinate system of proximal and distal barbules, and the result is used for the larger-scale barb masking. Note

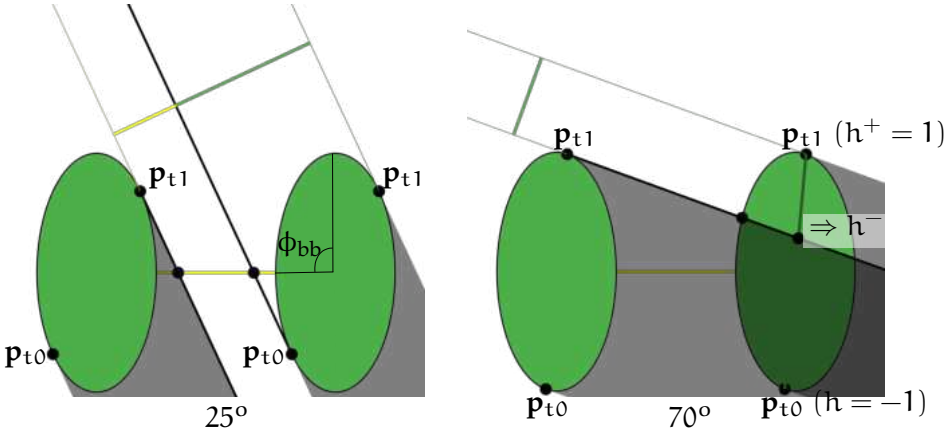

Figure 5.5: **Masking between two barbules at different view inclinations.** Barbules (and their projected area) are marked in green. The barbule separation and traced rays are shown as yellow and black segments respectively. We first trace a ray from the tangent point $\mathbf{p}_{t1}$, generating two cases: If it intersects the other ellipse (70° case) we need to intersect the ellipse's diameter to identify $\mathbf{p}_d$ and therefore h^-. The separation (transparency) cannot be seen ($w'_{bb} = 1$). If it does not intersect the other ellipse (25° case) then we need to intersect the separation segment with two tangent rays. We then calculate the local barbule weight w'_{bb} from the projected areas a_{bb} and a_s.

that previous work [66] models this masking term stochastically, and not analytically.

We explicitly model two barbules as ellipses while the separation between them is a segment (as represented in Figure 5.5. The barbule model parameters are, for reducing the number of parameters, the barbule axis ratio e_{bb} and the relative barbule separation δ_{bb}. We trace 2D rays from a tangent point at each ellipse towards each other and the separation segment. If there is occlusion between ellipses (ray has intersected) the lower limit of the integration range h^- ($h^-_{bp}(\omega_o)$ or $h^-_{bd}(\omega_o)$) requires tracing the same ray again towards the segment between $\mathbf{p}_{t0}$ and $\mathbf{p}_{t1}$ that represents the diameter of the ellipse. h^- is the parameter of the parametric equation of this diameter at the intersection point $\mathbf{p}_d$ (if there is no intersection, then $h^- = -1$). The other integration range limit is $h^+ = 1$. These geometrical elements can be visualized on Figure 5.5. This barbule masking term is applied twice, for both proximal and distal barbules, obtaining h^-_{bp}, h^+_{bp}, h^-_{bd}, h^+_{bd} and, from the projected areas, local weights w'_{bp} and w'_{bd}. As barbules are separated, there is also the possibility of local transparency with weights $1 - w'_{bp}$ and $1 - w'_{bd}$, respectively.

Barb masking At the upper scale, *barb masking*, we align the reference frame to the barb local frame. Hence the cross section of the barb is

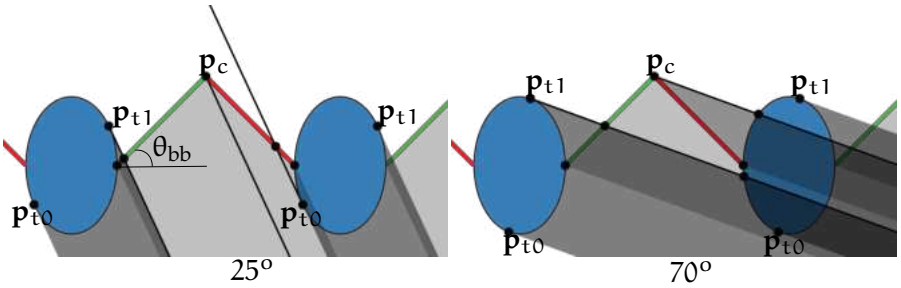

Figure 5.6: **Cross section of barbs, representing the masking between barbs at two different view inclinations.** Barbules (in red and green, respectively) are partially transmitting, depending on the view direction at their particular local coordinates (see Figure 5.5), while barbs (in blue) are considered to be opaque. Depending on the view direction, each element (barbs and barbules) totally or partially occludes the rest. The limits of such occlusions are identified by tracing 2D rays (marked in black). By considering all the particular intersection ranges we obtain the weights.

an ellipse, and the cross sections of the barbules are two segments (distal and proximal), with partial transparency obtained from the barbule masking component. Here, we compute the visibility ratios between barbs, barbules, and transmittance (see Figures 5.6 and 5.2, d). Note that previous work [66] does not provide a masking term that accounts for barbs and need to explicitly model the geometry of each individual barb.

Parameters are also relative with respect to the horizontal size of the barb, and include axis ratio e_b, barbule length l_{bb} and barbule inclination θ_{bb}. From these we obtain a representation of the microgeometry with two ellipses (barbs) and two pairs of segments (barbules). We trace rays from the visibility discontinuity points $\mathbf{p}_{t0}$, $\mathbf{p}_{t1}$ and $\mathbf{p}_c$ towards the rest of geometrical elements (segments and ellipses) and, from the ranges between intersection points, calculate the projected areas as before. Each interval correspond to total or partial occlusions (at this scale, barbules are partially transparent) so each projected area must be multiplied by $1 - w'_{bp}$ if it is occluded by the proximal barbule and by $1 - w'_{bd}$ if it is occluded by the distal barbule. We combine all projected areas and obtain w_b, w_{bp} and w_{bd}. We also obtain h_b^- and h_b^+ using the same procedure than for barbules. A detailed step-by-step procedure for obtaining these masking terms can be found in the Appendix B.

5.6.2 *Rendering*

For evaluating the BSDF as described by Equation (4.1), we simply calculate the weights from the masking expression and then evaluate

Figure	# Feathers	Resolution	Spp	Time
Figure 5.7	2500	512×256	1024	2.2 min
Figure 5.8	82	730×420	256	4.4 min
Figure 5.10	496	512×512	256	1.5 min
Figure 5.11	1	256×512	1024	1.5 min

Table 5.2: Rendering time for different scene complexities: single feather, feather pelt, feather wing and feather ball.

the corresponding BCSDFs at their local coordinate systems. For sampling it, we use a discrete distribution, similar to previous work [6] with four possible events (hit barb, hit proximal/distal barbules and delta transmittance) whose probabilities come from weights obtained from the analytical masking expression. The selected event is then sampled, deterministically if it is a delta transmittance or by using the BCSDF sampling routine of the specific fiber otherwise.

5.7 ANALYSIS AND RESULTS

In this section, we perform several experiments to show the capability of our feather BSDF, formal validation of our analytical masking term and comparison to previous work and photographs. We author each feather manually, by encoding the feathers geometry, including shaft, vane and barb orientation, on a 2D texture on top of a relatively simple geometry. Exploring more effective procedural tools for authoring (e.g., [8]) is left as an interesting future research direction.

We implemented our model in Mitsuba 0.6 [72] as a new BSDF. All our renders have been computed on an Intel Core i9-10900KF CPU with 20 cores. Table 5.2 reports the rendering time of all figures including scene with different complexity in terms of geometry (single feather, feather pelt, feather wing and feather balls), material (brown, black, blue, red and green feathers) and lighting conditions. Since our approach is surface-based, it is practical in terms of both rendering time and memory for fully feathered assets, which would be very expensive for curve-based feathers.

5.7.1 *Model analysis*

We perform ablation studies to analyze the impact of each component of our model. Figure 5.7 shows how increasing the complexity of the fiber cross section affects the final appearance produced by our fiber BCSDF in a significant manner. As previous work had already shown [84], an elliptical cross section with higher eccentricity increases the

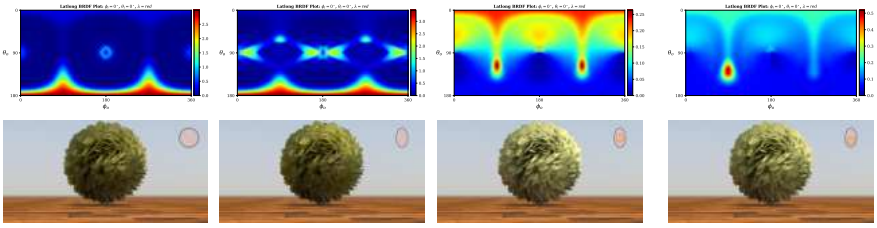

Circular Cortex | Elliptical Cortex | Concentric Medulla | Non-Concentric Medulla

Figure 5.7: Ablation studies of the Fiber BCSDF at ($\phi_i = 0^o$, $\theta_i = 45^o$): single cortex cylinder (first column), elliptical cortex cylinder (second column), nested cylinders with concentric medulla (third column) and nested cylinders with non-concentric medulla (last column). We show the latlong reflectance plots for the red wavelength. Fiber BCSDF parameters: $\sigma_{c,a} = (0.133, 1.967, 2.1)$, $\eta_c = \eta_m = 1.53$, $\beta_m = 0.13$, $\beta_n = 0.12$. The elliptical cross section is $e_b = 1.6$. Medulla is circular with radius 0.6 ($a_m = 0.6, b_m = 0.6$) and the non-concentric medulla is located at $c_x = -0.1$ and $c_y = 0.1$. Latlong reflectance plots are obtained with 10000 spp. Notice how the elliptical cortex increases the reflectance of the render, while the presence of the medulla makes the appearance softer. The latlong reflectance plots also reveals how each component affects the lobe patterns in a significant manner.

brightness of the specular lobes (see renders) and introduces new patterns as the elliptical blobs (see latlong reflectance plots). As we introduce a medulla, reflectance distribution gets more uniform and appearance gets smoother. When introducing a non-concentric medulla, reflectance distribution becomes asymmetric and the change in appearance with respect to the concentric case is important, showing a greater variation on appearance with respect to feather orientation.

Figure 5.8 shows the effect of both our masking and our BCSDF representing feathers, compared against using only hair barbs [53, 90] (first column), and against a more sophisticated feather structure with barbs and barbules modeled with a hair model (second column) and combined with a masking term, similar to the one proposed by Baron and colleagues [6]. As shown in the four examples, the medulla (third column) is essential to produce softer and non-iridescent structural colors such as green and blue tones. Notice that a closer appearance matching would require to match the lighting conditions and feather geometries more carefully. Nevertheless, the overall appearance produced by our full model better reproduces the real feathers' appearance than previous works.
Finally, in Figure 5.9 we validate our analytical masking term by comparison against a brute-force 100spp Monte-Carlo simulation of masking over explicit geometry (consisting of 100 barbs with 100 barbules each). Our masking expression yields similar weights to the reference,

Figure 5.8: Ablation studies of our feather BSDF for a feather pelt scene. **[Only hair barbs]:** Only barb with hair BCSDF [103]; **[Only masking]:** Barb and barbules with Hair BCSDF combined with our masking term similar to [6]; and **[Full]:** Adding a diffuse medulla inside the Barb BCSDF. Notice how our full model is capable of producing a wide variety of complex appearances that resemble closer the appearance of the photographs than previous works for several birds: From top to bottom, northern cardinal, blue-fronted amazon parrot (we reproduce the blue feathers in the face), eclectus parrot and Brewer's blackbird. In particular, the diffuse reflectance of the medulla is critical to achieve similar tones to the photographs, while the masking is important for goniochromatic and occlusions effects.

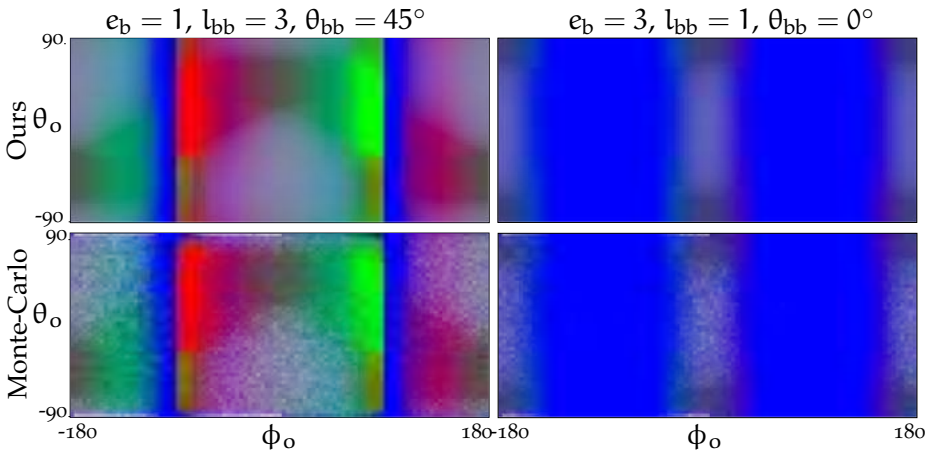

Figure 5.9: Comparison between our analytical masking expression (top) and a Monte-Carlo simulation (100spp) with ray tracing towards a full modeled microgeometry for the same parameters (bottom). Two different masking parametrizations have been explored (left and right columns), and the rest of the parameters are the same between the two: $e_{bb} = 1$, $\delta_{bb} = 1$. The horizontal and vertical axes per plot correspond to the view direction ω_o in polar coordinates (θ_o, ϕ_o). The colormap represents the weights of the different microgeometrical components: w_b, w_{bp} and w_{bd} are mapped to the blue, green, and red channels, respectively. Note how our analytical masking expression can obtain a noiseless result in a minimal fraction of the time (constant) while being accurate with respect to a fully modeled microgeometry.

but without any noise and in constant time.

5.7.2 *Appearance exploration*

In Figure 5.10 we analyze the feather expressivity of our appearance model by exploring the range of appearances that it can achieve. In particular: 1) Increasing the relative barbule separation (δ_{bb}) increases feather transparency as less transmitted rays are blocked by barbules. 2) Increasing barb axis ratio (e_b) increases the frequency of the highlights. Finally, 3) increasing the medulla size changes the hue of the feather, as well as the distribution of reflectance towards a more diffuse one. We provide a more thorough parameter exploration in Appendix B.

5.7.3 *Appearance matching with photographs*

We photograph two feathers using a conventional smartphone under different light conditions and create an scene to roughly match lighting conditions, appearance and shape of the captures, while ignoring the plumulaceous regions of the feather. Figure 5.11 shows our re-

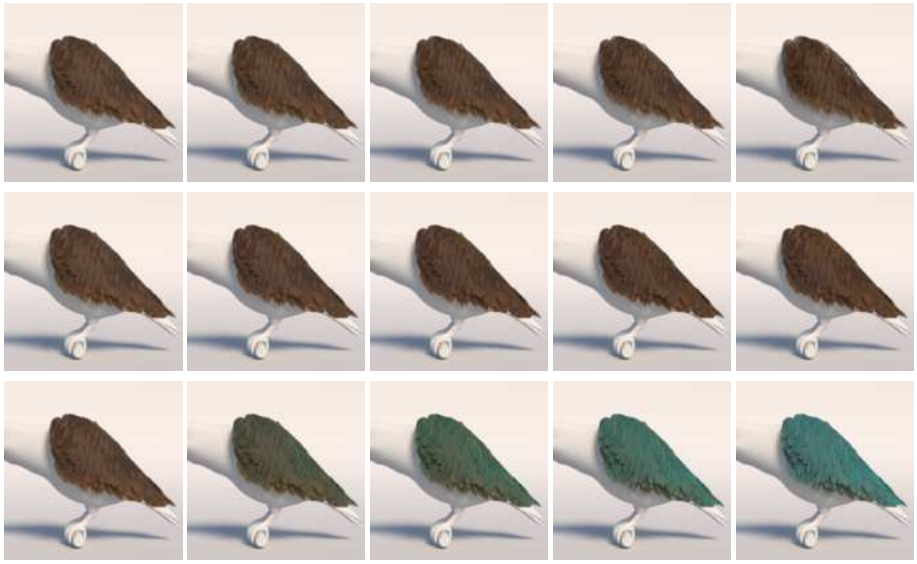

Figure 5.10: Parameter exploration of our model. **Top:** We vary the $\delta_{bb} = [0.1, 0.3, 0.5, 1.0, 3.0]$. Larger separation between the barbules increased the transmittance with high values showing prominent transparency effects. **Middle:** We show the effect of increasing the barb axis ratio $e_b = [1.0, 1.2, 1.4, 1.6, 1.8]$, progressively making the central highlight sharper. **Bottom:** We increase the size of the medulla $b_m = [0.0, 0.2, 0.4, 0.6, 0.8]$, for higher values, the color is mostly dominated by the color of the medulla and the appearance becomes more diffuse.

sults with the Amazon parrot, demonstrating that our masking can predict the view-dependent changes (top near frontal view, bottom rotated feather) of the final color due to different coloration between green barbs and yellow barbules.

Figure 5.12 shows a black goose feather lighted from behind. Similar to before, we capture the feather under varying rotation: Without masking, the transparency is independent of the rotation, while our masking predicts the loss on transparency as the feather rotates. In addition, this Figure demonstrates again the importance of the medulla to predict the blue tint of the feather due to structural coloration of feathers, which is not physically possible with a hair BCSDF as in previous works.

Note that we did not expect to perfectly match the photographs as they were taken under uncontrolled illumination conditions and the structural and optical parameters of the feather were unknown. In addition, near-field details such as visible individual barbs are not accounted by our model. Still, we show that the combination of our BCSDF and our masking term predict challenging appearance fea-

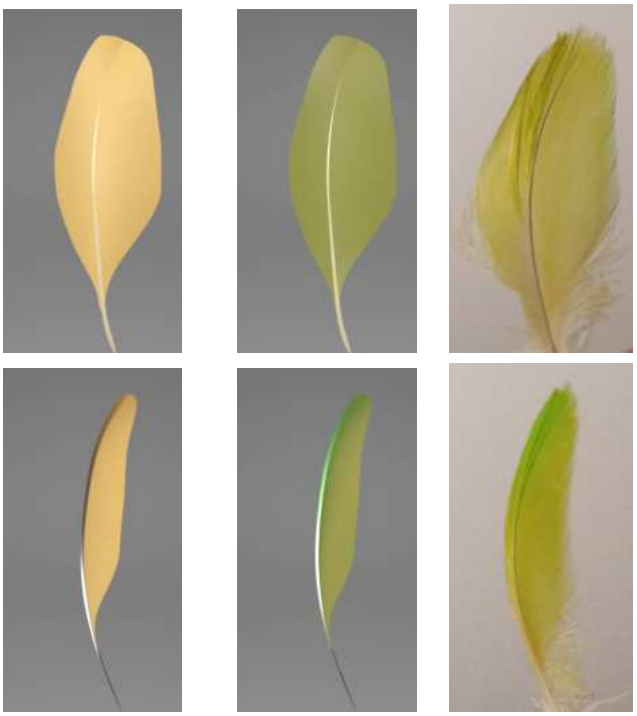

Without masking With masking Photograph

Figure 5.11: Qualitative appearance matching on an *Amazon parrot* feather, for a frontal (top) and lateral (bottom) views. As the feather rotates, view dependent changes on the feather's color become apparent: These are produced by visibility changes between barbs (yellow) and barbules (green). Our masking model is roughly able to predict these changes. Please see the supplemental video for a dynamic example of this goniochromism effect.

tures observed in feathers.

5.8 DISCUSSION

FAR-FIELD VS NEAR-FIELD Our model assumes far-field rendering of feathers, and thus is not able to capture the high-frequency details of visible barbs, which are naturally handled by curve-based methods, which in the far field suffer aliasing. Extending our method to near-field appearance would require more sophisticated authored maps and redefining the masking terms to support per-point masking. Deriving a proper filtering technique for such a near-field model is also left as future work.

SHADOWING To simplify our BSDF we decided to omit the shadowing term, which intuitively has little effect in natural lighting conditions. This allows us to use a far-field integration of the BCSDF, instead of requiring integrating both the input and outgoing visible

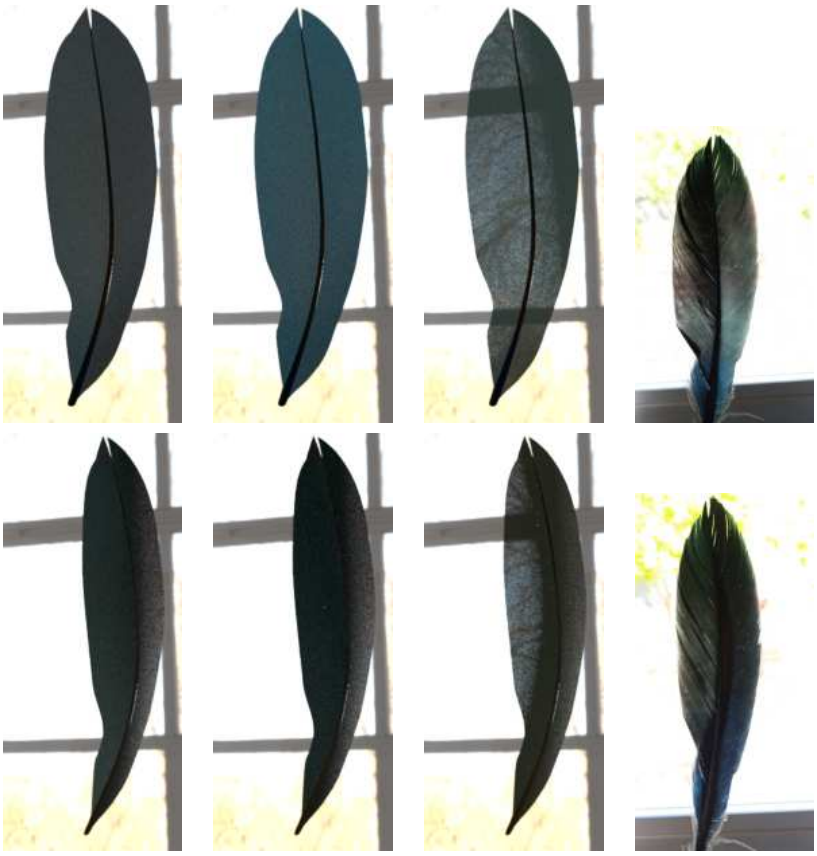

Figure 5.12: Qualitative appearance matching on a *black goose* feather, for a frontal (top) and lateral (bottom) views, under strong backlighting. Our masking term can reproduce view-dependent transparency. Note that the bluish appearance can only be achieved by the inclusion of a blue medulla.

surfaces of the fibers, at the cost of removing some physical plausibility.

ENERGY CONSERVATION Given the lack of shadowing, our BSDF is energy preserving without the need of multiple scattering simulations, except for the potential energy loss in the BCSDF, which might be significant when introducing elliptical cross-sections and an inner scattering medulla. However, as shown in Figure 5.13, we found that limiting light transport inside the fiber to five lobes results in a minimal energy loss.

WAVE OPTICS Our model omits important wave optical behavior, except for the structural coloration of the medulla, which we approximate as a diffuse reflection. Other effects such as the iridescence due to the grating-like structure of barbs and barbules, or the thin-film-like structure in barbules are omitted. The thin-film interference approach introduced in Section 3.3.2, replacing the Fresnel term with an Airy reflectance term (see Equation 3.1), can be a reasonable approximation for some iridescent barbules such as rock dove feathers [66]. Incorporating iridescent effects, as well as a more principled definition of the medulla's noniridescent structural coloration, is an interesting avenue for future work.

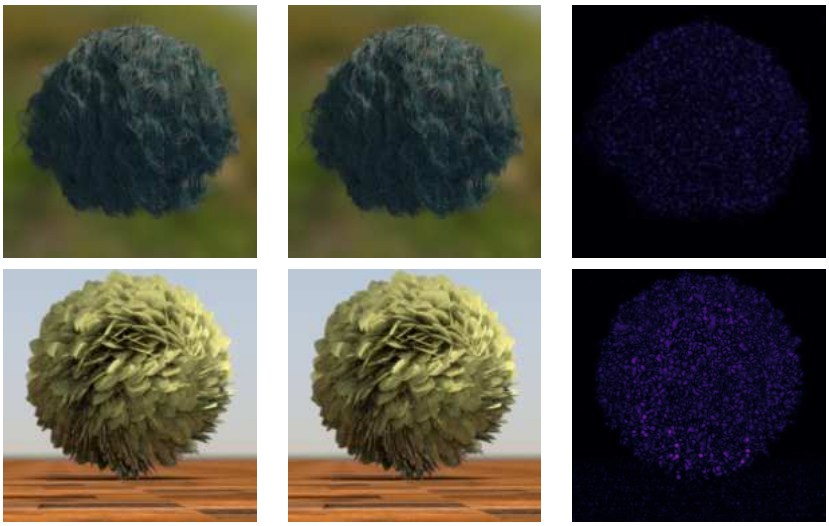

1000 lobes 5 lobes Error

Figure 5.13: Energy conservation validation of the BCSDF. For a five-bounces evaluation of our BCSDF we observe minimal differences with respect to a 1000-bounces counterpart, in both fiber-only, single scattering test (top) and inside our feathers BSDF with multiple scattering (bottom). Error is computed using the FLIP metric [4].

OTHER TYPES OF FEATHERS An important limitation of our surface-based approach is that it is not particularly suitable for plumulaceous feathers, where the vane is not as structured and is therefore more suitable for curve-based representations. Still, our BCSDF could be applied directly to curve-based representations [6], and hybrid approaches, where curve-based barbs encode flyaway and plumulaceous feathers, are probably the best choice for a general model covering the whole spectrum of feather appearances.

NON-ELLIPTICAL BARBS AND BARBULES An additional assumption of our work is the use of elliptical cross sections for barbs and barbules, which is a coarse approximation for both, especially barbules that appear in a wide variety of cross sections. We made this choice for limiting the space of parameters of our model into something manageable; however, our methodology for computing the BCSDF based on path tracing is very general, so fibers with arbitrary cross-section could be used, in the same spirit as the work of Aliaga et al. [2] for cloth fibers.

PARAMETER SPACE Our model is parametrized by a total of 23 parameters including the masking parameters (5 geometrical parameters), BCSDF barb parameters (12 parameters for cortex and medulla) and BCSDF barbule parameters (6 parameters for the cortex), with absorption coefficients and diffuse reflectance defined by RGB values. The model is expressive as shown in our experiments and the parameter space might seem challenging. However, these parameters all have an intuitive meaning, either structurally or appearance-wise, and the general appearance features of feathers (goniochromatism, view-dependant transmittance, highlights...) emerge naturally. We selected some of the parameter values based on the structural and optical properties observed on feathers in previous works [69, 105, 149] and we found the rest empirically. However, targeting a specific feather's appearance required several iterations of parameter editing in our experience. A more example-based automatic parameter selection would definitely be an interesting next step on this research path. Introducing a length-dependent barb radius would probably produce more realistic results.

CONCLUSION We have presented a practical surface-based far-field appearance model for feathers, in which we model the complex microgeometry of a feather as a light-weight texture and an analytical masking term that accounts for the angular-dependent visibility conditions, which previous curve-based models handled explicitly via curve visibility. On the core of our model is a new fiber BCSDF that supports elliptical cross sections and (potentially-colored) scat-

tering medulla, which is crucial for representing a wide variety of real-world feathers.

Part III

CONCLUSIONS

6 CONCLUSIONS

In this dissertation, we study how the multi-scale structure of two complex organic materials like scales and feathers and one intricate inorganic material such as cosmetics foundations affect their macro-scale appearance. In reptile skin and makeup foundations both materials can be represented as layered structures with multiple particle types, where the morphology, optical properties and the interaction between these particles play a major role in the main visual effects observed in these materials. In feathers, the multi-scale structure consists of an assembly of fibers organized in a hierarchical manner from the feather macro-scale to microscopic barbules. The challenge is then how to represent the shape and optical properties of the different fiber types (shaft, barbs and barbules) and account for the correct aggregated appearance rising from the light transport simulation.

6.1 CONTRIBUCIONS

Our first contribution discussed in Chapter 3 is a novel appearance model for rendering *snake skin* that takes into account the chromatophores inside snake scales responsible for their overall color patterns. Our solution is a two-layered material where the reflective and iridescent patterns produced by the iridophores (iridescent platelets) are approximated with a thin-film interference lobe, while the black and brown appearances from melanophores are modeled as diffuse high-absorbing participating media. We run the light transport simulation using the position-free Monte Carlo formulation [52] as this formulation supports arbitrary BSDF layers. We show the potential of our layered material to reproduce the most prominent visual features in snake skin and qualitatively match the striking iridescent patterns and dark appearance of a *Xenopeltis Unicolor* specimen. In contrast to previous work on diffraction from biological nanostructures [28], our appearance model is compact (only 7 global parameters)and it does not require the surface nanostructures by atomic force microscopy (AFM) or an expensive precomputation of the diffraction simulation on these nanostructures.

In the context of cosmetic rendering, we presented a new reflectance model in Chapter 4 inspired by the microscopic particles found in *cosmetic foundations* that can be integrated in a layered material framework in order to support the stacking of multiple cosmetic layers on top of human skin. Each individual cosmetic layer is modeled as a

stochastic participating medium filled with two types of scatterers: diffuse scatterers and specular platelets. We used a mixture of two Henyey-Greenstein phase functions to reproduce the matte appearance produced by diffuse scatterers inspired by a previous work in scattering of sunscreen lotions [117] and measurements of titanium dioxide particles suspended in a fluid [161]. For the platelets, we used the specular SGGX phase function without the Fresnel term to generate the glossy reflections. Similarly to our snake skin reflectance model, we used the position-free Monte Carlo frameworks that support multiple scattering and arbitrary BSDF layers. In contrast to data-driven approaches, our approach offers a higher degree of control and it is not entangled to other attributes of the scene like illumination or skin type. We validate our reflectance model against measure data for matte and dewy foundation products and show its potential for practical applications like matching the skin color type and stacking of multiple cosmetic products.

Finally, we introduced a novel practical appearance model for *pennaceous feathers* in Chapter 5. In this model, the feather BSDF is the result of a weighted linear combination of the individual BCSDF representing the scattering of the different barb and barbule fibers. We derive an analytical masking term to compute the weights and relatively visibility between barb and barbules given by the corresponding differential projected areas. Leveraging the regular and near-planar structure of pennaceous feathers, the underlying surface geometry of a single feather is efficiently represented using a compact two-dimensional texture encoding the angles and lengths of the feather barbs. Our reflectance model for the first time accounts for the noniridescent structural coloration with a diffuse approximation of the scattering from the spongy structures inside the medulla of barbs. This approximation is reasonable as previous studies [118] have found that the scattering of these spongy structures is predominantly dominated by backward scattering. We show the capabilities of our approach to reproduce several of the most important visual features in pennaceous feathers such as pigmentation, noniridescent structural coloration, view-dependent transmittance and goniochromatic effects.

6.2 FUTURE WORK

One of the open questions in this dissertation is up to what extent our reflectance models could be applied and adapted to model materials with relatively similar structures like other animal skin (amphibian, fishes or reptiles), cosmetic product types (bronzers, lipsticks, eye shadows or mascaras), feather types, or even other regular aggregation of fibers such as textiles, paper, or wood. Answering these

questions would require the study of the specific structures with SEM/TEM and collect reflectance measurements to understand the overall appearance behaviour and validate the reflectance models. Two important visual effects omitted in this dissertation are glittering for cosmetics and strong iridescence for feathers. In the case of cosmetics that exhibit glittering effects, multiple measurements might be required given the stochastic nature of these types of materials and a practical way to represent them in layered materials. For feathers, it is important to measure both the aggregated optical response of the entire feather (hierarchical collection of fibers) and the reflectance and absorption spectra from the individual components (barb fibers, barbule fibers and spongy structures inside the medulla) in isolation in order to understand better the contribution of each component and disambiguate the contribution from pigmentation from the contribution from structures.

Wave optics plays an important role in accurately reproducing the appearance of complex multi-scale materials especially in materials that exhibit strong structural coloration like some scales and feathers, and also to capture the subtle details of materials like cosmetics. In general, there are two main approaches to simulate wave optics and incorporate the information into the rendering process. Specialized solutions for specific structures and wave effects such as diffraction grating (Dhillon et al.'s work [28] for biological structures) or thin films (our solution for snake skin), or full-wave simulation of arbitrary microstructures or nanostructures using computational electromagnetic methods such as FTDT [112] or BEM [168]. Considering the variety of complex biological structures, the second approach coupled with procedural representations of the microstructures and nanostructures from measurements is an exciting direction for future work, as it was recently explored by Yu et al. [183] for iridescent barbules.

Studying the role of the different microstructures and nanostructures in the final appearance of materials, along with the light transport effects involved, presents a fascinating opportunity for future work in the long term in predictive rendering and the fabrication of complex multi-scale materials. Advances in this research could not only benefit computer graphics, but also contribute to other scientific and engineering fields, such as biology and materials science. Some of the key challenges are parameter selection, model simplification based on appearance, and model validation. Inverse rendering via the differentiable simulation of light transport [75] could play a crucial role in the robust validation of material models using calibrated material acquisition setups. It might also assist artists and users with appearance matching tasks. To address non-differentiable problems, learning local surrogate losses [39] or analysis by synthesis combined with neu-

ral networks could be explored. Model simplification is particularly important for layered materials [9], where reducing the number of layers while maintaining the target appearance remains a critical goal. Another potential direction for future work could be exploring Monte Carlo integration for solving multi-physics problems, such as coupled thermal-radiative transport [10] or fluid-structure interactions, leveraging, for example grid-free Monte Carlo methods [129, 130]. Finally, reflectance models parameterized directly by SEM/TEM data or their statistical aggregation could pave the way for a unified scattering model based on structure.

CONCLUSIONES

En esta disertación, estudiamos cómo la estructura múlti-escala de dos materiales orgánicos complejos, como las escamas y las plumas, y un material inorgánico intrincado, como las bases de maquillaje, afectan su apariencia a macroescala. Tanto en la piel de los reptiles como en las bases de maquillaje, ambos materiales pueden representarse como estructuras en capas con múltiples tipos de partículas, donde la morfología, las propiedades ópticas y la interacción entre estas partículas desempeñan un papel clave en los principales efectos visuales observados en estos materiales. En las plumas, la estructura múlti-escala consiste en un ensamblaje de fibras organizadas de manera jerárquica, desde la macroescala de la pluma hasta las bárbulas microscópicas. El desafío radica en cómo representar correctamente la forma y las propiedades ópticas de los distintos tipos de fibras (raquis, barbas y bárbulas) y en capturar la apariencia agregada correcta que surge de la simulación del transporte de luz.

CONTRIBUCIONES

Nuestra primera contribución, discutida en Chapter 3, es un modelo de apariencia novedoso para el renderizado de *piel de serpiente*, que tenga en cuenta los cromatóforos dentro de las escamas responsables de sus patrones de color. Nuestra solución es un material bicapa donde los patrones reflectantes e iridiscentes producidos por los iridóforos (plaquetas iridiscentes) se aproximan mediante un lóbulo de interferencia de capa fina, mientras que las apariencias negras y marrones de los melanóforos se modelan como un medio participante altamente absorbente y difuso. La simulación del transporte de luz se realiza utilizando la formulación de Monte Carlo de posicionamiento libre [52], ya que esta formulación permite manejar capas de materiales arbitrarios. Mostramos el potencial de nuestro material en capas para reproducir las características visuales más prominentes de la piel de serpiente y validamos cualitativamente con los patrones iridiscentes llamativos y la apariencia oscura de un espécimen de la *Xenopeltis Unicolor*. A diferencia de trabajos previos sobre difracción en nanoestructuras biológicas [28], nuestro modelo de apariencia es compacto (solo 7 parámetros globales) y no requiere el uso de microscopía de fuerza atómica (MFA) para caracterizar las nanoestructuras de la superficie ni una costosa precomputación de la simulación de difracción en estas nanoestructuras.

En el contexto de la renderización de cosméticos, presentamos un nuevo modelo de reflectancia en Chapter 4 inspirado en las partículas microscópicas presentes en la *bases de maquillaje*, que puede integrarse en una estructura de materiales laminados para el apilamiento de múltiples capas de cosméticos sobre la piel humana. Cada capa de cosmético individual se modela como un medio participante estocástico lleno de dos tipos de dispersores: dispersores difusos y plaquetas especulares. Utilizamos una mezcla de dos funciones de fase de Henyey-Greenstein para reproducir la apariencia mate generada por los dispersores difusos, inspirándonos en trabajos previos sobre dispersión en cremas de protección solar [117] y mediciones de partículas de dióxido de titanio suspendidas en un fluido [161]. Para las plaquetas, empleamos la función de fase especular SGGX sin el término de Fresnel para generar los reflejos brillantes. De manera similar a nuestro modelo de reflectancia de piel de serpiente, utilizamos Monte Carlo de posicionamiento libre, que permite manejar dispersión múltiple y materiales arbitrarios en las capas. A diferencia de los enfoques basados en datos, nuestro método ofrece un mayor grado de control y no está enmarañado con otros atributos de la escena, como la iluminación o el tipo de piel. Validamos nuestro modelo de reflectancia frente a datos medidos para productos de bases de maquillaje mate y rresplandeciente demostrando su potencial para aplicaciones prácticas como la adecuación al tipo de color de piel y el apilamiento de múltiples productos cosméticos.

Finalmente, introdujimos un modelo práctico de apariencia novedoso para *plumas pennáceas* en Chapter 5. En este modelo, la BSDF de la pluma es el resultado de una combinación lineal ponderada de las BCSDF individuales que representan la dispersión de las diferentes fibras de la pluma como barbas y bárbulas. Derivamos un término de enmascaramiento analítico para calcular los pesos y la visibilidad relativa entre barbas y bárbulas en función de las áreas proyectadas diferenciales correspondientes. Aprovechando la estructura regular y casi planar de las plumas pennáceas, la geometría de la superficie subyacente de una sola pluma se representa de manera eficiente mediante una textura bidimensional compacta que codifica los ángulos y longitudes de las barbas. Nuestro modelo de reflectancia, por primera vez, tiene en cuenta la coloración estructural no iridiscente mediante una aproximación difusa de la dispersión en las estructuras esponjosas dentro de la médula de las barbas. Esta aproximación es razonable, ya que estudios previos [118] han encontrado que la dispersión de estas estructuras esponjosas está dominada principalmente por la dispersión hacia atrás. Mostramos las capacidades de nuestro enfoque para reproducir varias de las características visuales más importantes en plumas pennáceas, como la pigmentación, la coloración estructural no iridiscente, la transmitancia dependiente del ángulo de visión y

los efectos gonio-cromáticos.

TRABAJO FUTURO

Una de las preguntas abiertas en esta disertación es hasta qué punto nuestros modelos de reflectancia podrían aplicarse y adaptarse para modelar materiales con estructuras relativamente similares, como otras pieles de animales (anfibios, peces o reptiles), otros tipos de productos cosméticos (bronceadores, lápices labiales, sombras para ojos o máscaras de pestañas), diferentes tipos de plumas, o incluso agregaciones regulares de fibras como textiles, papel o madera. Responder a estas preguntas requeriría el estudio de estas estructuras específicas mediante SEM/TEM y la recopilación de mediciones de reflectancia para comprender el comportamiento de la apariencia general y validar los modelos de reflectancia. Dos efectos visuales importantes que se omitieron en esta disertación son el brillo intenso en cosméticos como escarchas y la iridiscencia intensa en plumas. En el caso de los cosméticos que presentan efectos de brillo intensos granulares, podrían ser necesarias múltiples mediciones debido a la naturaleza estocástica de estos materiales y una forma práctica de representarlos en materiales laminados. Para las plumas, es fundamental medir tanto la respuesta óptica agregada de la pluma completa (colección jerárquica de fibras) como los espectros de reflectancia y absorción de los componentes individuales (fibras de las barbas, fibras de las bárbulas y estructuras esponjosas dentro de la médula) por separado. Esto permitiría comprender mejor la contribución de cada componente y diferenciar el efecto de la pigmentación del efecto estructural.

La óptica de ondas desempeña un papel crucial en la reproducción precisa de la apariencia de materiales complejos a múltiples escalas, especialmente en aquellos que presentan una coloración estructural intensa, como algunas escamas y plumas, y también en la captura de detalles sutiles en materiales como los cosméticos. En general, existen dos enfoques principales para simular la óptica de ondas e incorporar los resultados en el proceso de renderización: soluciones especializadas para estructuras y efectos de onda específicos, como rejillas de difracción (como el trabajo de Dhillon et al. [28] para estructuras biológicas) o capas finas (nuestra solución para la piel de serpiente), y la simulación completa de ondas en microestructuras o nanoestructuras arbitrarias mediante métodos electromagnéticos computacionales, como FTDT [112] o BEM [168]. Considerando la variedad de estructuras biológicas complejas, el segundo enfoque, combinado con representaciones procedurales de las microestructuras y nanoestructuras basadas en mediciones, es una dirección prometedora para trabajos futuros como lo exploraron recientemente Yu et

al. [183] para bárbulas iridiscentes.

Estudiar el papel de las diferentes microestructuras y nanoestructuras en la apariencia final de los materiales, junto con los efectos del transporte de luz involucrados, representa una oportunidad fascinante para futuras investigaciones a largo plazo en renderización predictiva y fabricación de materiales complejos a múltiples escalas. Los avances en esta investigación podrían beneficiar no solo a la computación gráfica , sino también a otros campos científicos y de ingeniería, como la biología y la ciencia de materiales. Algunos de los principales desafíos incluyen la selección de parámetros, la simplificación de modelos basada en la apariencia y la validación de modelos. La renderización inversa mediante la simulación diferenciable del transporte de luz [75] podría desempeñar un papel crucial en la validación robusta de modelos de materiales utilizando configuraciones calibradas de adquisición de materiales, además de ayudar a artistas y usuarios en tareas de concordancia de la apariencia a una referencia. Para abordar problemas no diferenciables, se podrían explorar métodos como el aprendizaje local con costos subrogados [39] o el análisis por síntesis combinado con redes neuronales. La simplificación de modelos es particularmente importante para los materiales multicapas [9], donde reducir el número de capas manteniendo la apariencia objetivo sigue siendo un desafío crítico. Otra posible dirección de investigación futura sería explorar la integración de Monte Carlo para resolver problemas multi-físicos, como el transporte térmico-radiativo acoplado [10] o las interacciones fluido-estructura, aprovechando, por ejemplo, métodos de Monte Carlo libre de rejillas [129, 130]. Finalmente, los modelos de reflectancia parametrizados directamente por datos SEM/TEM o su agregación estadística podrían abrir el camino hacia un modelo unificado de dispersión basado en la estructura.

Part IV

APPENDIX

A

PRACTICAL APPEARANCE MODEL FOR FOUNDATION COSMETICS - APPENDIX

In this appendix, we include additional information about the optimization process and performance for the reflectance model introduced in Chapter 4 for cosmetic foundations. In Table A.1, we report the optimized parameters for the four foundation samples measured to validate the reflectance model. In Table, we present the renderings time for some of the figures in Chapter 4. Notice how our cosmetic layer only introduces a small overhead in terms of rendering time despite our work being more focused on rendering accuracy than computational performance. In fact, we do not perform any sophisticated performance optimization strategies.

Parameter	Dewy 1	Dewy 2	Matte 1	Matte 2
α_p	0.13	0.002	0.15	0.49
θp	1.47°	5.5°	2.01°	52.2°
Λ_p	(0.75,0.85,0.99)	(0.8,0.8,0.8)	(0.91, 0.89,0.85)	(0.93,0.83,0.71)
c_d	0.90	0.99	0.89	0.29
Λ_d	(0.99,0.98,0.95)	(0.97,0.93,0.87)	(0.95,0.94,0.91)	(0.9,0.9,0.84)
g_1	0.55	0.77	0.37	0.24
g_2	0.09	-0.23	-0.25	-0.22
w_g	1.0	0.79	0.62	0.51
t	16	16	16	16

Table A.1: Optimized parameters fit from our measured reflectance data using our cosmetic appearance model for several cosmetic products.

Figure	Resolution	SPP	Time	Thickness
7 (First row - Matte 1)	1223×1269	128	11.4 min	0.5
7 (First row - Matte 2)	1223×1269	128	11.0 min	0.5
7 (First row - Reference)	1223×1269	128	9.25 min	0.5
7 (First row - Dewy 1)	1223×1269	128	9.95 min	0.5
7 (First row - Dewy 2)	1223×1269	128	10.95 min	0.5
7 (Second row - Matte 1)	1332×1187	512	25.3 min	0.35
7 (Second row - Matte 2)	1332×1187	512	24.8 min	0.35
7 (Second row - Reference)	1332×1187	512	24.8 min	0.35
7 (Second row - Dewy 1)	1332×1187	512	24.2 min	0.35
7 (Second row - Dewy 2)	1332×1187	512	25.3 min	0.35
11 (First row - no foundation)	1332×1187	512	25.3 min	0.0
11 (First row - one layer)	1332×1187	512	25.3 min	0.25
11 (First row - two layers)	1332×1187	512	25.3 min	1.25

Table A.2: Rendering times for our reflectance model for cosmetics foundation for several experiments.

B

A SURFACE-BASED APPEARANCE MODEL FOR PENNACEOUS FEATHERS - APPENDIX

This is the appendix for the reflectance model for pennaceous feathers introduced in Chapter 5. In addition to this document, we include a supplemental video with an example of goniochromatism in feathers due to barbule masking and relighting examples from the main experiments in the project website (https://graphics.unizar.es/projects/FeathersAppearance_2024/). The content of this appendix is organized as follows:

- The derivation of the ray-ellipse intersection and projected area used for computing barbule and barb masking;
- The derivation of masking terms of the feather BSDF;
- Details on the authoring process of the feather's geometry;
- And additional results exploring the space of appearances achievable with the feather reflectance model.

B.1 ELLIPSE EQUATIONS

In this section of the appendix, we explore the different geometrical representations of the ellipse, as well as the properties and derivations of those representations that our reflectance model for feathers uses for ray intersections, tangent point detection, and projected area integrals.

An ellipse is characterized by its center $\mathbf{c} = c_x, c_y$ and its two axes a_x and a_y. Its **implicit equation** for a two-dimensional point $\mathbf{p} = p_x, p_y$ is:

$$\frac{(p_x - c_x)^2}{a_x^2} + \frac{(p_y - c_y)^2}{a_y^2} - 1 = 0 \quad . \tag{B.1}$$

We can obtain the **normal** $\mathbf{n} = n_x, n_y$ for each point from the gradient of the left part of the Equation B.1, which yields:

$$\mathbf{n} = \begin{pmatrix} n_x \\ n_y \end{pmatrix} = \begin{pmatrix} 2\frac{p_x - c_x}{a_x^2} \\ 2\frac{p_y - c_y}{a_y^2} \end{pmatrix} \tag{B.2}$$

which should be normalized afterwards.

The **parametric equation** of this same ellipse is based on an angular parameter $\theta \in [-\pi, \pi)$:

$$\mathbf{p} = \begin{pmatrix} p_x \\ p_y \end{pmatrix} = \begin{pmatrix} c_x + a_x \cos\theta \\ c_y + a_y \sin\theta \end{pmatrix}, \tag{B.3}$$

We can also obtain an expression for the **normal direction** according to this parametric version as described in Equation B.3 by calculating the direction perpendicular to the tangent (derivative), as:

$$\mathbf{n} = \begin{pmatrix} n_x \\ n_y \end{pmatrix} = \begin{pmatrix} -a_y \cos\theta \\ -a_x \sin\theta \end{pmatrix}, \tag{B.4}$$

which should be normalized afterwards.

We can also invert Equation B.3 to **obtain the parameter** θ from a point in the ellipse $\mathbf{p}$ as:

$$\theta = \operatorname{atan2}\left(\frac{p_y - c_y}{a_y}, \frac{p_x - c_x}{a_x}\right). \tag{B.5}$$

Another operation on ellipses we will need to do (for casing shadows / masking) is to find the points in the ellipse for which the tangent is a specific direction $\mathbf{d} = d_x, d_y$, which is equivalent to saying that the normal $\mathbf{n}$ is perpendicular to $\mathbf{d}$, which combined from Equation (B.4) yields:

$$\begin{aligned} \mathbf{n} \cdot \mathbf{d} &= 0 \\ -a_y \cos\theta_t d_x - a_x \sin\theta_t d_y &= 0 \\ a_y d_x + a_x \tan\theta_t d_y &= 0 \\ \tan\theta_t &= \frac{-a_y d_x}{a_x d_y} \\ \theta_t &= \tan^{-1}\frac{-a_y d_x}{a_x d_y} + k\pi \qquad k \in \mathbb{Z}. \end{aligned} \tag{B.6}$$

For the purpose of casting, the only solutions that we need for θ_t in Equation (B.6) are for $k \in \{0, 1\}$ because other solutions generate the same set of points from the parametric ellipse, as described in Equation B.3. Those two casting points are:

$$\begin{aligned} \mathbf{p}_0 &= \begin{pmatrix} c_x + a_x \cos\left(\tan^{-1}\frac{-a_y d_x}{a_x d_y}\right) \\ c_y + a_y \sin\left(\tan^{-1}\frac{-a_y d_x}{a_x d_y}\right) \end{pmatrix} \\ \mathbf{p}_1 &= \begin{pmatrix} c_x + a_x \cos\left(\tan^{-1}\frac{-a_y d_x}{a_x d_y} + \pi\right) \\ c_y + a_y \sin\left(\tan^{-1}\frac{-a_y d_x}{a_x d_y} + \pi\right) \end{pmatrix}. \end{aligned} \tag{B.7}$$

Also, it is common for fiber-based microgeometry modeling to use a projected diameter according to a casting direction $\mathbf{d}$, a rectilinear segment parametrized by $h \in (-1, 1)$ that generates ray origin points $\mathbf{o}$:

$$\mathbf{o}(h) = \mathbf{p_0}\frac{h-1}{2} + \mathbf{p_1}\frac{h+1}{2} - l\mathbf{d}, \tag{B.8}$$

where l is a distance large enough so that the segment does not intersect with the ellipse. In our case, we use $l = 10\max(a_x, a_y)/|\mathbf{d}|$. For the inverse operation (finding the parameter h of the projection of a given point in the ellipse) we trace a ray from the point towards direction $-\mathbf{d}$ and estimate the parameter h within the segment by inverting Equation B.8.

To calculate the **intersection with a 2d ray** we need to start from the implicit equation as described in Equation (B.1) and define a system of equations with the equation of the 2d ray with origin $\mathbf{o}$ and direction $\mathbf{d}$: $\mathbf{p} = \mathbf{o} + t\mathbf{d}$. By substituting the point in the implicit equation with the equation of the ray, we get:

$$\begin{aligned}
\frac{(o_x + td_x - c_x)^2}{a_x^2} + \frac{(o_y + td_y - c_y)^2}{a_y^2} - 1 &= 0 \\
\frac{t^2 d_x^2 + 2td_x(o_x - c_x) + (o_x - c_x)^2}{a_x^2} + \frac{t^2 d_y^2 + 2td_y(o_y - c_y) + (o_y - c_y)^2}{a_y^2} - 1 &= 0 \\
t^2\left(\frac{d_x^2}{a_x^2} + \frac{d_y^2}{a_y^2}\right) + t\left(\frac{2d_x(o_x - c_x)}{a_x^2} + \frac{2d_y(o_y - c_y)}{a_y^2}\right) + \left(\frac{(o_x - c_x)^2}{a_x^2} + \frac{(o_y - c_y)^2}{a_y^2} - 1\right) &= 0,
\end{aligned} \tag{B.9}$$

which is a second-degree equation that obtains all the t parameters (if any) of the intersections.

The last interesting operation to do with an ellipse is to calculate the integral of the **projected "area"** from a direction $\mathbf{d}$ within a parameter range $[\theta_0, \theta_1]$ with respect to the unnormalized normal direction (which corresponds to the area differential) in Equation (B.4):

$$\begin{aligned}
\int_{\theta_0}^{\theta_1} \mathbf{n}(\theta) \cdot \mathbf{d}\, d\theta &= \int_{\theta_0}^{\theta_1} -d_x a_y \cos\theta - d_y a_x \sin\theta\, d\theta \\
&= d_x a_y(\sin\theta_0 - \sin\theta_1) + d_y a_x(\cos\theta_1 - \cos\theta_0).
\end{aligned} \tag{B.10}$$

B.2 MASKING

In this section, we describe the mathematical and algorithmic details of our masking analytical expression at both levels (barbule and barb level), which were left out from Chapter 5 due to their level of detail. They are included here for reproducibility purposes.

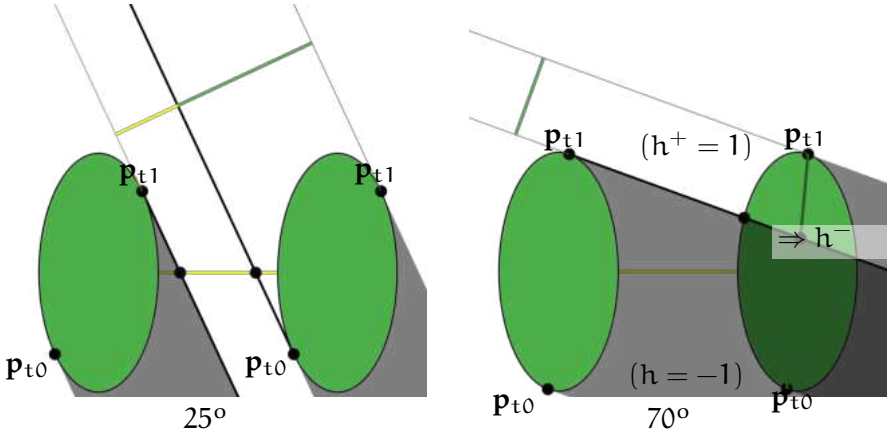

Figure B.1: **Masking between two barbules at different view inclinations.** Barbules (and their projected area) are marked in green. The barbule separation and traced rays are shown as yellow and black segments respectively. We first trace a ray from the tangent point $\mathbf{p}_{t1}$, generating two cases: If it intersects the other ellipse (70° case) we need to intersect the ellipse's diameter to identify $\mathbf{p}_d$ and therefore h^-. The separation (transparency) cannot be seen ($w'_{bb} = 1$). If it does not intersect the other ellipse (25° case) then we need to intersect the separation segment with two tangent rays. We then calculate the local barbule weight w'_{bb} from the projected areas a_{bb} and a_s.

B.2.1 *Barbule Masking*

The barbule masking expression is computed twice, for both proximal and distal barbules, at their respective local coordinate systems given by the transform matrices $\mathbf{T}_{bp}$ and $\mathbf{T}_{bd}$, respectively. We will name $\omega'_o = \{\omega'_{ox}, \omega'_{oy}\}$ the two-dimensional direction in the local coordinate space (the longitudinal dimension is ignored) after transforming ω_o. From this expression we will obtain the integration range limits for each barbule BCSDF ($h^-_{bp}(\omega_o)$,$h^+_{bp}(\omega_o)$, $h^-_{bd}(\omega_o)$ and $h^+_{bd}(\omega_o)$) and the local barbule (w'_{bp} and w'_{bd}, respectively) between 0 and 1, which are later used in the barb masking component. The local transmittances (visibility through the barbules) are $1 - w'_{bp}$ and $1 - w'_{bd}$, respectively.

We explicitly model two barbules as ellipses, while the separation between them is a segment (as represented in Figure B.1). The barbule model parameters are, for reducing the number of parameters, the barbule axis ratio e_{bb} and the relative barbule separation δ_{bb}.
To identify the visibility limits among the two barbules and the separation segment, we first cast a two-dimensional ray, following the local masking direction ω'_o. The origin point for such a ray is the visibility boundary of the ellipse, that is, the point in the ellipse that is

tangential to ω'_o. For an ellipse with center $\mathbf{c} = \{c_x, c_y\}$ and axes a_x and a_y, there are two tangent points:

$$\mathbf{p}_{t0} = \begin{pmatrix} c_x + a_x \cos(\alpha) \\ c_y + a_y \sin(\alpha) \end{pmatrix} \quad , \mathbf{p}_{t1} = \begin{pmatrix} c_x + a_x \cos(\alpha + \pi) \\ c_y + a_y \sin(\alpha + \pi) \end{pmatrix}, \tag{B.11}$$

where $\alpha = \tan^{-1}\left(\frac{-a_y \omega'_{ox}}{a_x \omega'_{oy}}\right)$.

We choose which ellipse is cast to the other one and which of the two points we use as a ray origin depending on the quadrant of ω'_o. If this ray intersects the other ellipse at the point $\mathbf{p}_{bb}$, there is no transmittance through the barbules: $w'_{bb} = 1$. The lower limit of the integration range h^- ($h^-_{bp}(\omega_o)$ or $h^-_{bd}(\omega_o)$) requires tracing a the same ray again towards the segment between $\mathbf{p}_{t0}$ and $\mathbf{p}_{t1}$ that represents the diameter of the ellipse. h^- is the parameter of the parametric equation of this diameter at the intersection point $\mathbf{p}_d$. The other integration range limit is $h^+ = 1$. These geometrical elements can be visualized in Figure B.1 (left).

If the ray does not intersect the other ellipse, then the barbule is fully visible ($h^- = -1$ and $h^+ = 1$) and we intersect this ray and the separation segment between both ellipses, obtaining an intersection point $\mathbf{p}_{s0}$. We also trace a new ray from the other tangent point of the other ellipse towards the same separation segment and find another intersection $\mathbf{p}_{s1}$. Then, the projected areas (a_{bb} for the barbule and a_s for the separation segment) are:

$$a_s = \omega'_o \cdot (\mathbf{p}_{s1} - \mathbf{p}_{s0})^\perp \qquad a_{bb} = A(\alpha, \alpha + \pi), \tag{B.12}$$

where $A(\beta_0, \beta_1)$ is the projected area of the barbule between two angles of its parametric form, calculated as:

$$A(\beta_0, \beta_1) = \omega'_{ox} a_y (\sin(\beta_0) - \sin(\beta_1)) + \omega'_{oy} a_x (\cos(\beta_1) - \cos(\beta_0)), \tag{B.13}$$

and the local barbule weight is then calculated as the relative projected area: $w'_{bb} = a_{bb}/(a_{bb} + a_s)$. A diagram representing these geometrical components is shown in Figure B.1 (right).

Ellipse intersections, tangent points, and projected areas are derived from the implicit and parametric equations of the ellipse. Such derivations can be found in section B.1.

B.2.2 *Barb Masking*

The barb masking term is similar to the barbule term, albeit slightly more complex. We model two barbs as ellipses, as well as two sets

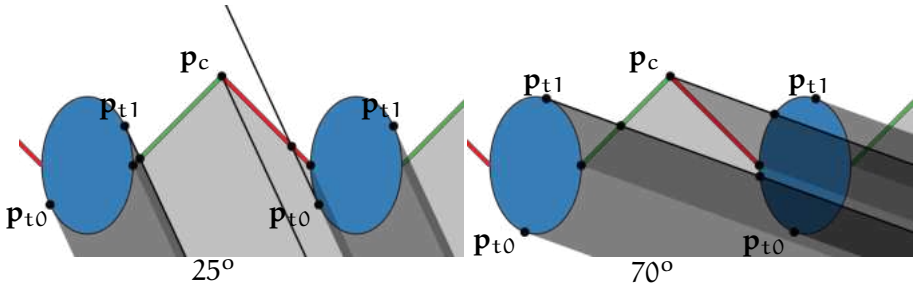

Figure B.2: **Cross section of barbs, representing the masking between barbs at two different view inclinations.** Barbules (in red and green, respectively) are partially transmitting, depending on the view direction at their particular local coordinates (see Figure B.1), while barbs (in blue) are considered to be opaque. Depending on the view direction, each element (barbs and barbules) totally or partially occludes the rest. The limits of such occlusions are identified by tracing 2D rays (marked in black). By considering all the particular intersection ranges we obtain the weights of each element.

of barbules as segments, symmetric with a specific inclination θ_{bb} (so we are actually considering the plane at which the barbules lie, regardless of their orientation). By doing so, we are assuming that barbules' thickness is negligible compared to barbs' thickness, which is often the case: they tend to be one order of magnitude thinner than the barbs [100]. As parameter models, and similar to barbules, all distance parameters are relative with respect to the horizontal size of barbs, including the barb axis ratio e_b and barbule length l_{bb} and inclination θ_{bb} (with respect to the horizontal plane). local barbule weights w'_{bp} and w'_{bd} from the barbule masking expression. Barbule segments are aligned with the horizontal axis of the plane, so we can obtain three significant points: the corner between the barbule segments ($\mathbf{p}_c$), the limit points of the proximal and distal barbules at the barb ($\mathbf{p}_{bp}$ and $\mathbf{p}_{bd}$, respectively).

Similarly to the barbule masking term, we cast rays from one of the tangent points of both ellipses, obtained as described by Equation B.11, towards the contiguous ellipse and both barbule segments. This gives the location of the boundary of the full occlusion for barbs ($\mathbf{p}_{b\to b}$) and barbules ($\mathbf{p}_{b\to bp}$ and $\mathbf{p}_{b\to bd}$, respectively). We also cast a ray from the corner $\mathbf{p}_c$ to the next barb and the next proximal barbule, obtaining the corresponding intersection points $\mathbf{p}_{c\to b}$ and $\mathbf{p}_{c\to bd}$, to identify the boundaries of partial occlusion: as there is separation between barbules (as obtained by the barbule masking expression), it is possible that there is some partial visibility through the barbules. All these points are shown for different cases in Figure B.2.

Then we obtain projected areas of the barb (a_b), proximal barbule (a_{bp}), distal barbule (a_{bd}) and transmittance (a_t, which represent the visibility through the vane). There are multiple combinations of cases regarding partial or global occlusions, from one or both barbules to the barb or to each other of the barbules, depending on whether each of the three different rays intersect each of the microgeometrical components.

If the ray from the barb does not intersect the proximal barbule, then $\mathbf{p}_{b\to bp}$ does not exist and it is fully occluded ($a_{bp} = 0$). Otherwise:

$$a_{bp} = w'_{bp} \max\left(0, \left(\omega_o \cdot (\mathbf{p}_c - \mathbf{p}_{b\to bp})^\perp\right)\right), \tag{B.14}$$

where $(\mathbf{p}_c - \mathbf{p}_{b\to bp})^\perp$ represents the perpendicular (unnormalized) direction of the visible part of the proximal barbule.

The distal barbule can be directly visible or visible through the proximal barbule depending on their orientation with respect to the view direction ω_o, so it is calculated as:

$$a_{bd} = \begin{cases} w'_{bd} \max\left(0, \left(\omega_o \cdot (\mathbf{p}_{bd} - \mathbf{p}_{b\to bd})^\perp\right)\right) & \text{if } \left(\omega_o \cdot (\mathbf{p}_{bd} - \mathbf{p}_c)^\perp\right) > 0 \\ (1 - w'_{bp}) w'_{bd} \max\left(0, \left(\omega_o \cdot (\mathbf{p}_c - \mathbf{p}_{b\to bd})^\perp\right)\right) & \text{otherwise,} \end{cases} \tag{B.15}$$

where the max function helps to identify whether the distal barbule is fully occluded by the barb ($\mathbf{p}_{b\to bd}$ is outside the segment that represents the distal barbule).

For the transmittance, if barbs occlude each other ($\mathbf{p}_{b\to b}$ exists) then $a_t = 0$. If not, if the distal barbule is visible, $\left(\omega_o \cdot (\mathbf{p}_{bd} - \mathbf{p}_c)^\perp\right) > 0$, then we trace a new ray for the other tangent point of the other ellipse towards the distal barbule, obtaining $\mathbf{p}_t$. Then:

$$\begin{aligned} a_t = {} & (1 - w'_{bp}) \max\left(0, \left(\omega_o \cdot (\mathbf{p}_c - \mathbf{p}_{b\to bp})^\perp\right)\right) \\ & + (1 - w'_{bd}) \max\left(0, \left(\omega_o \cdot (\mathbf{p}_t - \mathbf{p}_{b\to bd})^\perp\right)\right). \end{aligned} \tag{B.16}$$

Otherwise, only the proximal barbule contributes to transmittance, so this ray is traced towards the distal barbule, obtaining $\mathbf{p}_t$. Then:

$$a_t = (1 - w'_{bp}) \max\left(0, \left(\omega_o \cdot (\mathbf{p}_t - \mathbf{p}_{b\to bp})^\perp\right)\right). \tag{B.17}$$

For the barbs, we obtain h^- following the same procedure as with the barbules (ignoring barbule occlusion). The projected area is obtained by sorting all relevant points on the ellipse: $\mathbf{p}_{t0}$, $\mathbf{p}_{b\to b}$, $\mathbf{p}_{bd}$, $\mathbf{p}_{c\to b}$ and $\mathbf{p}_{t1}$ according to their parametrical angle (using the inverse of the parametric function). Depending on the ordering this leads to up to

three different parameter ranges (ignoring the part of the barb fully occluded by the other barb below $\mathbf{p}_{b\to b}$). The projected area of each of those ranges is calculated using Equation B.13, multiplied by a factor depending on the potential partial occlusions, $(1-w'_{bp})$ or $(1-w'_{bd})$, if the range is occluded by the proximal or distal barbule, respectively, $(1-w'_{bp})(1-w'_{bd})$ if occluded by both and 1 if unoccluded). The contribution of all those ranges is added into a_b.

The final weights for the BSDF ($w_b(\omega_o)$, $w_{bp}(\omega_o)$, $w_{bd}(\omega_o)$ and $w_t(\omega_o)$) are obtained by normalizing all the projected areas. For any particular weight i:

$$w_i(\omega_o) = \frac{a_i}{\sum_j a_j}. \tag{B.18}$$

There is a particular corner case that rarely happens, that has been omitted for the sake of simplicity and efficiency. When viewed at grazing angles, barbules could partially occlude not only the barb but the next barbules (one after the other) lead to an infinite sequence of partial occlusions that is approximated by a single occlusion in our case, with minimal effect on the final appearance.

B.3 FEATHER GEOMETRY

In our reflectance model for pennaceous feathers, we represent the feather geometry as a 2D texture and we only model the shaft and barbs. The barbules are considered in our appearance model. Figure B.3 shows a diverse group of feather geometries from our own collection manually authored using Inskape. We also create synthetic feathers in a similar fashion to the data-driven approach presented in previous work [8]. The overall goal is to derive the feather shape from real world photographs and the anatomy of individual feathers keeping the model as flexible as possible for further editions. In Figure B.4, we show an example of a feather texture of a red-crowned parrot feather from Feather Atlas [153] generated by our script.

We rely on Bezier Curves to represent and manipulate the anatomy of each feather, .ie., the shaft, left and right vane contours and barbs. The first step is background matting, separating the foreground (feather) from its background. The second step is the curve regressions to represent the main shape of the feather, namely the shaft, left vane and right vane with curves. A segmentation of the shaft can be tricky for traditional computer vision approaches. For this reason, we obtain the landmarks semi-automatically by manually picking them using ImageJ. For the left and right vane, we fit the Bezier curves to the set of landmarks by solving a least square optimization using Penrose pseudoinverse.

The Bezier curves can control the vane contours and the shaft. For the barb generation, additional parameters are required, such as the shaft width (base, tip), barb width, barb angles or barb numbers. These parameters can be obtained by measurements (image-based using ImageJ or physically-based using capture devices) or can be collected from previous biological studies. Once we have all these parameters, the shaft and barb generation are the next steps. The shaft generation consists of a Bezier curve interpolation from the shaft base width to the shaft base tip. Barbs are generated from the initial rachis location to the distal tip of the feather. For each barb, we compute the intersection between a rotated line based on the corresponding barb angle and the corresponding vane curve. Given the point in the rachis and the intersection points, the barb is represented as a Bezier curve going through those points. Two intermediate points of the line are slightly distorted to fit a cubic Bezier curve. Finally, the feather geometry is saved as a texture where the red channel stores the tangent angle of the curve, the green channel the barb curve length with respect to the rachis point and the blue channel the image masks (background, shaft, vanes).

For our implementation, we use the following Python libraries: (1) image manipulation (OpenCV), curve regression (numpy and scipy) and Bezier curve manipulation (bezier). We are planning to continue the development of the image-based generation scripts and the integration with strand-based representation of previous works.

B.4 APPEARANCE EXPLORATION

In this section of the appendix, we explore some of the potential appearances of the most interesting parameters of the reflectance model for feathers. For these experiment, we create a matrix of renders for a feather wing under sunlight conditions, where we vary only two parameters we are interested in and let the rest of parameters be fixed. In particular, we include experiments of the following configurations: (1) barb eccentricity vs barbule longitudinal angle, (2) barbule length vs barbule separation, (3) barb roughness vs barb eccentricity, (4) barb roughness vs barbule roughness and (5) barb eumelanin vs pheomelanin.

In Figure B.5, we explore the relationship in terms of appearance between the barbule inclination and the barb eccentricity. As we increase the barb eccentricity the feather becomes slightly brighter in some regions (close to the rachis) and darker in others (upper right vane). On the other hand, a larger barbule longitudinal angle (barbule inclination) results in a larger influence of the barbule BCSDF

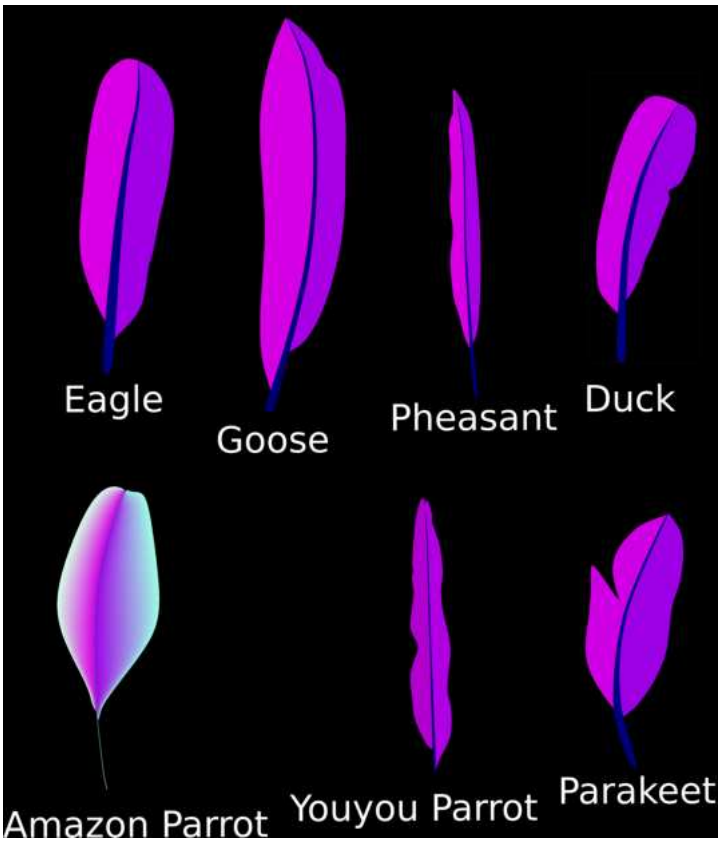

Figure B.3: Examples of feather geometries as 2D textures (1000 dpi) manually authored using Inskape. Please notice the variety of shapes, despite only considering pennaceous type of feathers.

for some regions of the barb depending on the barb angle given by the geometry texture.

In Figure B.6, we analyze how the different configurations between barbule length and barbule separation affect the masking term in terms of appearance. The larger the barbule separation, the more transparent the feather becomes. On the other hand, the larger the barbule length is, the more prominent the barbule appearance is.

In Figure B.7, the barb roughness parameter controls the transition between a specular surface and a matte surface, while higher barb eccentricity values increase the intensity at some specific regions and darker it at others.

In Figure B.8, we vary both the barb roughness and the barbule roughness and evaluate how they affect the final appearance of a single feather. The larger the roughness, the more matte and softer the final appearance becomes. At low roughness, the specular highlights from the barb and barbules are clearly noticeable and they can be a helpful setup to debug the contribution of each feather component in more

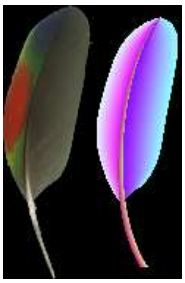

Figure B.4: Feather geometry example semi-automatically generated using the image-based generation Python script. **Left** Feather photograph of a red-crowned parrot feather (source: [153]). **Right** Feather geometry as a 2D texture (1000 dpi).

detail.

In Figure B.9, we perform an appearance parameter exploration for the two main pigments of our barb BCSDF. Please notice how the appearance of the single feather changes from white and yellowish appearance for low eumelanin and pheomelanin values to dark brown and black appearance for higher values.

Figure B.5: Appearance single feather exploration for two free model variables: the barb eccentricity parameter (rows) $b_c = [1.0, 1.3, 1.6, 1.8]$ and the barbule longitudinal angle parameter (columns) $\theta_{bb} = [0°, 10°, 15°, 30°, 45°]$.

Figure B.6: Appearance exploration of a feather wing for two free model variables under front point light source: the barbule length parameter (rows) $l_{bb} = [0.01, 0.1, 1.0, 2.0, 10.0]$ and the barbule separation parameter (columns) $\delta_{bb} = [0.01, 0.1, 0.5, 1.0, 2.0]$.

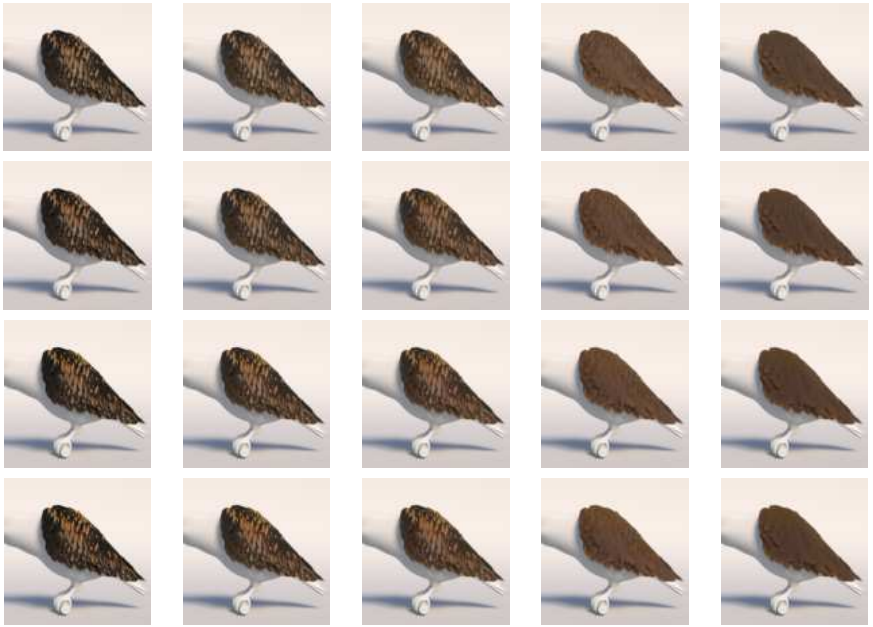

Figure B.7: Appearance exploration of a feather wing for two free model variables: the barb eccentricity (rows) $b_c = [1.0, 1.3, 1.6, 1.8]$ and the barb roughness parameter (rows) $\beta_b^m = [0.01, 0.05, 0.1, 0.5, 1.0]$.

Figure B.8: Appearance exploration of a feather wing for two free model variables: the barb roughness parameter (columns) $\beta_b^m = [0.01, 0.1, 0.5, 1.0, 2.0]$ and the barbule roughness roughness parameter (rows) $\beta_{bb}^m = [0.01, 0.1, 0.5, 1.0, 2.0]$.

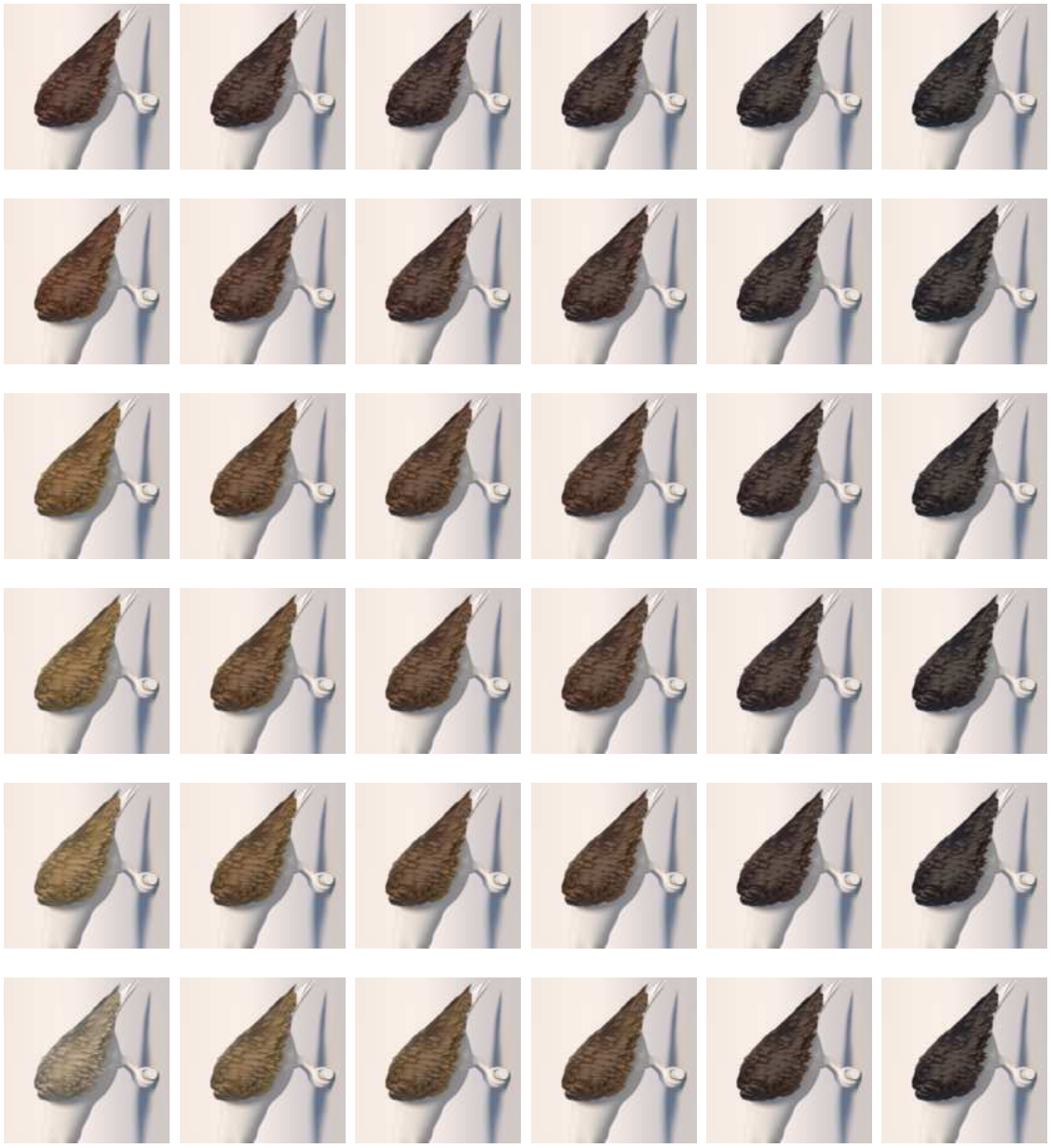

Figure B.9: Appearance exploration of a feather wing for two free model variables: the barb eumelanin parameter (rows) $\rho_{b,e} = [0.1, 0.5, 0.75, 1.0, 2.0, 3.0]$ and the barb pheomelanin (columns) $\rho_{b,p} = [0.1, 0.5, 0.75, 1.0, 2.0, 3.0]$.

C

SCATTERING MODELS - APPENDIX

In this Appendix, we describe fundamental scattering models used in the reflection models presented in Chapter 3, Chapter 4, and Chapter 5. Microfacet models statistically describe surface roughness, while the Henyey-Greenstein (HG) phase function models anisotropic light scattering in volumetric media. Fiber scattering captures anisotropic reflections in materials like hair, woven fabrics, and feathers, where cylindrical structures influence light behavior. Lastly, layered scattering models efficiently simulate light interaction in multi-layered materials such as biological tissues, coated surfaces, and stratified participating media.

C.1 MICROFACET MODEL

A fundamental problem in surface reflection is how to simulate the interaction of light with surfaces that are not perfectly smooth, surfaces with microscopic imperfections known as rough surfaces. Microfacet theory defines a rough surface as a surface with a large collection of microscopic perfect specular facets, where the distribution of the facet orientations is defined statically with respect to the normal of the surface. Intuitively, the larger the variation of these microfacets, the rougher the surface becomes, making the reflections blurrier. The Cook-Torrance reflectance model [25] is one of the most popular microfacet-based BRDFs:

$$f_r(x, \omega_i, \omega_o) = \frac{D(\omega_h)F(\omega_i)G(\omega_i, \omega_o)}{4\cos\theta_i \cos\theta_o}. \tag{C.1}$$

One of the main advantages of this reflectance model is the flexibility to pick different definitions for the different terms: microfacet distribution, the geometry term, and the Fresnel term. $D(\omega_h)$ is the microfacet distribution function specifying the probability that a microfacet is aligned with the half-angle vector h. Common normal distribution functions that can handle smooth to rough surfaces are the Beckmann [11] and GGX [158] distributions, where GGX has a longer tail usually found in real-world surfaces. θ_i and θ_o are the angle between the incident and view direction respectively with respect to the normal of the surface. $F(\omega_i, \omega_o$ is the fresnel term, describing how much light is reflected versus refracted at the incident direction ω_i depending on the index of refraction of the interface. $G(\omega_i, \omega_o)$ is the geometric attenuation term accounting for the masking and shadowing effects of the microfacets. Masking occurs when some microfacets obstruct the view (potential outgoing light) of other microfacets, while

shadowing happens when some microfacets block the incoming light potentially arriving to other microfacets. Two of the most common examples of geometric attenuation terms are the Smith's masking-shadowing function [135]and one of its approximations, the Schlick-Smith masking function [132]. In Chapter 5, we derive an analytical masking term for the particular microstructure of pennaceous feathers.

C.2 HENYEY-GREENSTEIN PHASE FUNCTION

The Henyey-Greenstein phase function [60] is a convenient parametric model designed to fit measured scattering data, in particular scattering by interstellar dust. This phase function is parametrized by the cosine of θ (the angle between ω_i and ω_o) and the asymmetry parameter g:

$$f_p(g, \cos\theta) = \frac{1}{4\pi} \frac{1 - g^2}{(1 + g^2 + 2g\cos\theta)^{3/2}}. \tag{C.2}$$

The asymmetry parameter $-1 \leqslant g \leqslant 1$ controls the scattering distribution from back-scattering ($g < 0$), isotropic ($g = 0$) to forward scattering ($g > 0$). In Figure C.1, we show three examples of the Henyey-Greenstein phase functions for the three scattering scenarios. In Chapter 4, we model the scattering from diffusers inside the cosmetics foundation layer using a mixture of two Henyey-Greenstein phase functions.

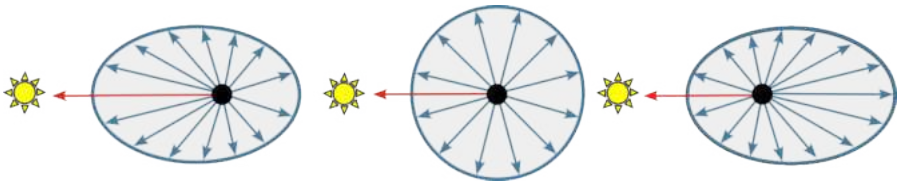

Figure C.1: A phase function describes the angular distribution of light scattering at any given point x inside a participating media. In an ideal scenario light is scattered equally in all directions (middle, isotropic scattering). In real scenarios, the scattering of light is dominated by backward (left, back scattering) or forward (right, forward scattering) directions.

C.3 FIBER SCATTERING

In a previous section, we introduced the concept of BRDF and how it defines the interaction of light with surfaces. Reflectance models

for fibers treat individual fibers as cylinders and introduce a new scattering function *Bidirectional Curve Scattering Function* (BCSDF):

$$L_r(\omega_r) = \int L_i(\omega_i) S(\omega_i, \omega_r) \cos(\theta_i) d\omega_i, \tag{C.3}$$

where S is the BCSDF. L_i is the incoming radiance coming from the incident direction ω_i, while L_r is the outgoing radiance from the outgoing direction ω_r.

The Marschner hair reflectance model [103] treats hair fibers as smooth dielectric cylinders with internal absorption. This model uses a longitudinal-azimuthal parametrization to factor the BCSDF S into a product of the longitudinal profile M and the azimuthal cross-section N contributions:

$$S(\theta_i, \theta_r, \phi_i, \phi_r) = \sum_p \frac{S(\theta_i, \theta_r, \phi_i, \phi_r)}{\cos^2 \theta_d} = \sum_p \frac{M_p(\theta_h) N_p(\phi_r - \phi_i, \eta)}{\cos^2 \theta_d}, \tag{C.4}$$

where $\theta_d = \frac{(\theta_r - \theta_i)}{2}$ and $\theta_h = \frac{(\theta_i + \theta_r)}{2}$ are the longitudinal difference angle and half angle respectively. The model only considers the first three light paths (R, TT and TRT) as illustrated in Fig. X, where R and T stand for reflection and transmission respectively. Khungurn and Marschner [84] study extensively the impact of the elliptical hair fibers and the different properties with respect to circular azimuthal cross sections.

In rendering is a common practice to divide the scattering models into near-field and far-field models, especially when the width of the hair fibers is so thin that it is smaller than a pixel. The near field scattering for the azimuthal cross section considers the actual incident position parametrized with the azimuthal fiber offset $h \in [-1, 1]$. On the other hand, the far field scattering assumes parallel light rays that cover the entire azimuthal cross section, .ie., the fiber's width. Therefore, the far-field approximation of the azimuthal scattering function can be computed by integrating the near-field scattering over all possible offsets h:

$$Np(\phi) = \frac{1}{2} \int_{-1}^{1} N_p(h, \phi) dh. \tag{C.5}$$

This integral for far-field approximation could be solved either analytically [103] for smooth dielectric cylinders or numerically [195] for rough dielectric cylinders using an expensive Gaussian quadrature. Chiang et al. [23] delegates this integration problem to the renderer and solve it with Monte Carlo integration. We adopted Chiang et al. strategy for the rendering of the internal fibers of our feather appearance model introduced in Chapter 5 as this strategy is accurate and

simple to integrate in a path tracing renderer.

In contrast to a human hair fiber, the size of the medulla inside a fur fiber is usually non-negligible and the internal structure is complicated. Based on this observation, Yan et al. [173] introduced a double cylinder model that models the anatomical structure of a single fur fiber more faithfully. The outer cylinder (cortex) is a dielectric cylinder similar to the Marschner hair reflectance, while the inner cylinder (medulla) scatters light inside. The medulla scattering is precomputed using a similar approach to the empirical BSSRDF for 2D scattering profiles given the factorization of the lobes into longitudinal and azimuthal lobes. Modeling the scattering of the medulla is essential for the soft look and diffusive appearance of fur. Later, a reflectance model was simplified drastically by unifying the index of refraction from the cortex and the medulla simplifying the light transport paths to 5 lobes. The unscattered lobes (R, TT, TRT) share the same paths as the hair reflectance model and the unscattered lobes for TT and TRT consider the interactions with the medulla.

Multiple fiber scattering (multiple light bounces among fibers) is essential for rendering light colored hair/fur fibers, but it might be computationally expensive as it requires simulating global illumination. Multiple scattering in hair fibers can be significantly accelerated with the dual scattering approximation [192]. Another strategy is reducing the number of individual fibers with aggregation appearance techniques that preserve the appearance. The aggregated BCSDF of Zhu et al. [189] extends the fur reflectance model for a single fiber to capture the multiple scattering of light between the individual fibers with three additional lobes.

In Chapter 5, we define the reflectance model of barb and barbules inside a feather with a BCSDF. We compute the multiple scattering between fibers without approximation and the light transport inside the fibers without precomputation with a diffuse medulla. Finally, we define the fibers implicitly instead of explicitly with strand-based hair geometry.

C.4 LAYERED MATERIALS

In Chapter 2, we considered two fundamental scenarios for light transport depending on whether the interaction happens with a surface or with a volume. Materials made of layers can be considered as a special scenario combining both types of interactions with custom solutions like the Kubelka-Munk model and the adding-doubling method for ray optics, or the transfer matrix method in the context of wave optics. Many real-world materials exhibit a layered struc-

ture from ceramics, metallic paints, colored plastics to biological tissues such as skin or wood. A layered BSDF model describes the reflectance properties of an object where its surface consists of a stack of planar layers with potential participating media separated by smooth or rough interfaces. Different configurations of the layers and interfaces can produce an extensive variety of material appearances from diffuse appearances and highly anisotropic reflections to complex spatially-varying patterns. Unfortunately, modeling and rendering layered materials can be complex and computationally expensive. For this reason, there has been significant attention by the computer graphics community to studying this problem from specialized models for the weathering metals, leaves [162] or human skin [31, 139] to general frameworks [52, 76, 166].

Several parametric reflectance models of layered structures have been derived for specific configurations. Human skin Stam [139] can be represented by stacking a dielectric surface on top of a bounding participating medium or a more complicated reflectance model with two heterogeneous media layers separated by a thin absorption layer considering the characteristic concentrations of chromatophores. Leaves also have a layered structure, and several approaches have been proposed from explicit 3D models of the internal structure of leaf tissues [Govaerts et al. 1996] to practical real-time single-layer BSDF simulations incorporating rough surface scattering and subsurface scattering. Layered structures can also be a practical representation of time-varying effects such as weathering of metals due to chemical reactions such as oxidation or corrosion that can be modeled using a layer operation like erosion. In recent years, the computer graphics community has focused more on general layered models making a trade -off between the approximation assumptions, computational cost, and rendering variance.

Several general solutions have been proposed, from fast analytical approximations to expensive numerical methods. One of the first general reflectance models for layered materials is the analytical microfacet-based model of Weidlich and Wilkie [166] where all microfacet BSDFs at the interfaces are combined into a single microfacet BSDF. This analytical model is fast, but ignores multi-scattering inside the layers. Multiple scattering between layers can be correctly incorporated using the adding-doubling method [67] as the numerical method introduced by LayerLab [76] proposed to handle both analytical and isotropic measured BSDF where the response of each BRDF of a given material to incident illumination is precomputed and stored using a harmonic representation that can be queried and sampled in rendering time. The subsequent work by Zelten and Jakob [184] extends this framework to support anisotropic interfaces by defining direc-

tional scattering operators. In addition, they introduced a subtraction operation that allows them to reconstruct the BSDF material from the indirect observation of another well-known material. These numerical methods are robust and accurate, but they require an expensive precomputation and large storage memory per material. Belcour [12] combines the idea of representing the final contribution of a layered material as a sum of GGX lobes and adapts the adding-doubling method to this statistical representation by tracking the low-order statistics of BSDFs at the interfaces for each event reflection, refraction, absorption, and forward scattering. This approximation enables interactive rendering but assumes that there is no surface and volume anisotropy. Later, the work of Weier et al. [167] extends the Belcour model to handle anisotropic microfacet models. By approximating anisotropic GGX distribution lobes with ellipsoidal distributions and utilizing a diagonal covariance matrix in the tangent space, the adding-doubling method can be applied independently to each ellipsoid axis.

The work of Guo and colleges [52] introduced a general, accurate and precomputation-free method to evaluate arbitrary layered BSDF with Monte Carlo simulation considering the special case of flat layers, where the position-free formulation significantly reduces the high variance from the geometry terms in the standard path-tracing formulation. The key advantage of this approach is its flexibility as it supports surface and volume scattering, spatially-varying parameters and anisotropic effects. The main limitation in comparison to non-stochastic layered models is the higher rendering time and higher variance. Xia et al. [169] developed a compact parametric Gaussian representation of the BSDF for individual layers that allows them to sample the product of two or more BSDFs at the same time. This new sampling strategy offered a substantial reduction in variance compared to the position-free framework [52] for isotropic layered surfaces.

In Chapter 3 and Chapter 5, we model reptile skin and stacking of cosmetic foundations applied on top of human skin as layered BSDFs taking into account its particular internal structure. Then, we use the position-free Monte Carlo formulation [52] to simulate the light transport inside them, as this formulation allows us to design arbitrary layer interfaces and internal media. In addition, it significantly reduces the high variance from the stochastic evaluation of these complex layered materials compared to brute-force volumetric path tracing. Finally, the internal structure of the barbs in feathers can also be considered a layered structure with cylindrical layers.

BIBLIOGRAPHY

[1] 9GAGGER. *Iridescent Sunbeam Snakes*. 2020. URL: https://9gag.com/gag/awBO1EB (visited on 09/04/2020).

[2] Carlos Aliaga, Carlos Castillo, Diego Gutierrez, Miguel Otaduy, Jorge Lopez-Moreno, and Adrian Jarabo. "An Appearance Model for Textile Fibers." In: *Computer Graphics Forum (Proc. EGSR 2017)* 36.4 (2017).

[3] Carlos Aliaga, Menqi Xia, Xao Xie, Adrian Jarabo, Gustav Braun, and Christophe Hery. "A Hyperspectral Space of Skin Tones for Inverse Rendering of Biophysical Skin Properties." In: *Computer Graphics Forum* 42.4 (2023), e14887. DOI: https://doi.org/10.1111/cgf.14887. eprint: https://onlinelibrary.wiley.com/doi/pdf/10.1111/cgf.14887. URL: https://onlinelibrary.wiley.com/doi/abs/10.1111/cgf.14887.

[4] Pontus Andersson, Jim Nilsson, Tomas Akenine-Möller, Magnus Oskarsson, Kalle Åström, and Mark D. Fairchild. "FLIP: A Difference Evaluator for Alternating Images." In: *Proceedings of the ACM on Computer Graphics and Interactive Techniques* 3.2 (2020), 15:1–15:23. DOI: 10.1145/3406183.

[5] Gladimir V. G. Baranoski and Jon G. Rokne. "Efficiently simulating scattering of light by leaves." In: *The Visual Computer* 17.8 (2001), pp. 491–505. DOI: 10.1007/s003710100126.

[6] Jessica Baron, Daljit Singh Dhillon, N. Adam Smith, and Eric Patterson. "Microstructure-based appearance rendering for feathers." In: *Computers & Graphics* 102 (2022), pp. 452–459. ISSN: 0097-8493. DOI: https://doi.org/10.1016/j.cag.2021.09.010. URL: https://www.sciencedirect.com/science/article/pii/S0097849321002028.

[7] Jessica Baron and Eric K. Patterson. "Computer-Aided Visual Analysis of Feathers." In: *Proceedings of the ICPR Workshop on Visual Observation and Analysis of Vertebrate and Insect Behavior (VAIB)*. Milan, Italy, Jan. 2021.

[8] Jessica Baron and Eric Patterson. "Procedurally Generating Biologically Driven Feathers." In: *Advances in Computer Graphics*. Springer International Publishing, 2019, pp. 342–348. ISBN: 978-3-030-22514-8. DOI: https://doi.org/10.1007/978-3-030-22514-8_29.

[9] Mégane Bati, Pascal Barla, and Romain Pacanowski. "An inverse method for the exploration of layered material appearance." In: *ACM Trans. Graph.* 40.4 (July 2021). ISSN: 0730-0301. DOI: 10.1145/3450626.3459857. URL: https://doi.org/10.1145/3450626.3459857.

[10] Mégane Bati, Stéphane Blanco, Christophe Coustet, Vincent Eymet, Vincent Forest, Richard Fournier, Jacques Gautrais, Nicolas Mellado, Mathias Paulin, and Benjamin Piaud. "Coupling Conduction, Convection and Radiative Transfer in a Single Path-Space: Application to Infrared Rendering." In: *ACM Trans. Graph.* 42.4 (July 2023). ISSN: 0730-0301. DOI: 10.1145/3592121. URL: https://doi.org/10.1145/3592121.

[11] Petr Beckmann and Andre Spizzichino. "The scattering of electromagnetic waves from rough surfaces." In: *Norwood* (1987).

[12] Laurent Belcour. "Efficient rendering of layered materials using an atomic decomposition with statistical operators." In: *ACM Trans. Graph.* 37.4 (July 2018). ISSN: 0730-0301. DOI: 10.1145/3197517.3201289. URL: https://doi.org/10.1145/3197517.3201289.

[13] Laurent Belcour and Pascal Barla. "A Practical Extension to Microfacet Theory for the Modeling of Varying Iridescence." In: *ACM Transactions on Graphics* 36.4 (2017).

[14] Alexis Benamira and Sumanta Pattanaik. "A combined scattering and diffraction model for elliptical hair rendering." In: *Computer Graphics Forum* 40.4 (2021), pp. 163–175. DOI: https://doi.org/10.1111/cgf.14349. eprint: https://onlinelibrary.wiley.com/doi/pdf/10.1111/cgf.14349. URL: https://onlinelibrary.wiley.com/doi/abs/10.1111/cgf.14349.

[15] Benedikt Bitterli, Srinath Ravichandran, Thomas Müller, Magnus Wrenninge, Jan Novák, Steve Marschner, and Wojciech Jarosz. "A Radiative Transfer Framework for Non-Exponential Media." In: *ACM Trans. Graph.* 37.6 (Dec. 2018). ISSN: 0730-0301. DOI: 10.1145/3272127.3275103. URL: https://doi.org/10.1145/3272127.3275103.

[16] Benedikt Bitterli and Eugene d'Eon. "A position-free path integral for homogeneous slabs and multiple scattering on Smith microfacets." In: *Computer Graphics Forum* 41.4 (2022), pp. 93–104. DOI: 10.1111/cgf.14589.

[17] Carles Bosch, Xavier Pueyo, Stéphane Mérillou, and Djamchid Ghazanfarpour. "A Physically-Based Model for Rendering Realistic Scratches." In: *Computer Graphics Forum* 23.3 (2004), pp. 361–370. DOI: https://doi.org/10.1111/j.1467-8659.2004.00767.x. eprint: https://onlinelibrary.wiley.com/doi/pdf/10.1111/j.1467-8659.2004.00767.x. URL: https:

//onlinelibrary.wiley.com/doi/abs/10.1111/j.1467-8659.2004.00767.x.

[18] Brent Burley, David Adler, Matt Jen-Yuan Chiang, Hank Driskill, Ralf Habel, Patrick Kelly, Peter Kutz, Yining Karl Li, and Daniel Teece. "The Design and Evolution of Disney's Hyperion Renderer." In: *ACM Trans. Graph.* 37.3 (July 2018). ISSN: 0730-0301. DOI: 10.1145/3182159. URL: https://doi.org/10.1145/3182159.

[19] J. Buzek and B. Ask. *Regulation (EC) No 1223/2009 of the European parliament and of the council of 30 November 2009 on cosmetic products*. https://www.eumonitor.eu/9353000/1/j9vvik7m1c3gyxp/vibn2mp7slr0. 2009.

[20] Subrahmanyan Chandrasekhar. *Radiative Transfer*. London: Dover Publications, 1960.

[21] Huiwen Chang, Jingwan Lu, Fisher Yu, and Adam Finkelstein. "PairedCycleGAN: asymmetric style transfer for applying and removing makeup." In: *Computer Vision and Pattern Recognition (CVPR)*. IEEE, 2018, pp. 40–48. DOI: 10.1109/CVPR.2018.00012.

[22] Yanyun Chen, Yingqing Xu, Baining Guo, and Heung-Yeung Shum. "Modeling and rendering of realistic feathers." In: *ACM Transactions on Graphics (TOG)* 21.3 (2002), pp. 630–636.

[23] Matt Jen-Yuan Chiang, Benedikt Bitterli, Chuck Tappan, and Brent Burley. "A Practical and Controllable Hair and Fur Model for Production Path Tracing." In: *Computer Graphics Forum* 35.2 (2016), pp. 275–283. DOI: https://doi.org/10.1111/cgf.12830. eprint: https://onlinelibrary.wiley.com/doi/pdf/10.1111/cgf.12830. URL: https://onlinelibrary.wiley.com/doi/abs/10.1111/cgf.12830.

[24] Per Christensen et al. "RenderMan: An Advanced Path-Tracing Architecture for Movie Rendering." In: *ACM Trans. Graph.* 37.3 (Aug. 2018). ISSN: 0730-0301. DOI: 10.1145/3182162. URL: https://doi.org/10.1145/3182162.

[25] R. L. Cook and K. E. Torrance. "A Reflectance Model for Computer Graphics." In: *ACM Trans. Graph.* 1.1 (Jan. 1982), 7–24. ISSN: 0730-0301. DOI: 10.1145/357290.357293. URL: https://doi.org/10.1145/357290.357293.

[26] Tom Cuypers, Tom Haber, Philippe Bekaert, Se Baek Oh, and Ramesh Raskar. "Reflectance model for diffraction." In: *ACM Transactions on Graphics (TOG)* 31.5 (2012), pp. 1–11.

[27] Han Deng, Chu Han, Hongmin Cai, Guoqiang Han, and Shengfeng He. "Spatially-invariant style-codes controlled makeup transfer." In: *Computer Vision and Pattern Recognition (CVPR)*. IEEE, 2021, pp. 6549–6557. DOI: 10.1109/CVPR46437.2021.00648.

[28] D. Dhillon, J. Teyssier, M. Single, I. Gaponenko, M. Milinkovitch, and M. Zwicker. "Interactive Diffraction from Biological Nanostructures." In: *Computer Graphics Forum* 33.8 (2014), pp. 177–188. DOI: https://doi.org/10.1111/cgf.12425. eprint: https://onlinelibrary.wiley.com/doi/pdf/10.1111/cgf.12425. URL: https://onlinelibrary.wiley.com/doi/abs/10.1111/cgf.12425.

[29] Daljit Singh J. Dhillon and Abhijeet Ghosh. "Efficient Surface Diffraction Renderings with Chebyshev Approximations." In: *SIGGRAPH ASIA 2016 Technical Briefs*. SA '16. New York, NY, USA: Association for Computing Machinery, 2016. ISBN: 97814-50345415. DOI: 10.1145/3005358.3005376. URL: https://doi.org/10.1145/3005358.3005376.

[30] Craig Donner and Henrik Wann Jensen. "Light Diffusion in Multi-Layered Translucent Materials." In: *ACM Trans. Graph.* 24.3 (July 2005), 1032–1039. ISSN: 0730-0301.

[31] Craig Donner, Tim Weyrich, Eugene d'Eon, Ravi Ramamoorthi, and Szymon Rusinkiewicz. "A layered, heterogeneous reflectance model for acquiring and rendering human skin." In: *ACM transactions on graphics (TOG)* 27.5 (2008), pp. 1–12.

[32] Marc Droske, Johannes Hanika, Jiri Vorba, Andrea Weidlich, and Manuele Sabbadin. "Path tracing in production: the path of water." In: *ACM SIGGRAPH 2023 Courses*. ACM, July 2023. ISBN: 9798400701450. DOI: 10.1145/3587423.3595519.

[33] A Ennos, J Hickson, and ANNA Roberts. "Functional morphology of the vanes of the flight feathers of the pigeon Columba livia." In: *The Journal of experimental biology* 198.5 (1995), pp. 1219–1228.

[34] S. Ergun, S. Önel, and A. Ozturk. "A general micro-flake model for predicting the appearance of car paint." In: *Proceedings of the Eurographics Symposium on Rendering: Experimental Ideas & Implementations*. EGSR '16. Dublin, Ireland: Eurographics Association, 2016, 65–71. ISBN: 9783038680192.

[35] Becca E. Ewing, Samuel D. Butler, and Michael A. Marciniak. "Improved grazing angle bidirectional reflectance distribution function model using Rayleigh–Rice polarization factor and adaptive microfacet distribution function." In: *Optical Engineering* 57.10 (2018), p. 105102. DOI: 10.1117/1.OE.57.10.105102.

[36] Viggo Falster, Adrian Jarabo, and Jeppe Revall Frisvad. "Computing the bidirectional scattering of a microstructure using scalar diffraction theory and path tracing." In: *Computer Graphics Forum* 39.7 (2020), pp. 231–242.

[37] Luca Fascione, Johannes Hanika, Mark Leone, Marc Droske, Jorge Schwarzhaupt, Tomáš Davidovič, Andrea Weidlich, and Johannes Meng. "Manuka: A Batch-Shading Architecture for Spectral Path Tracing in Movie Production." In: *ACM Trans. Graph.* 37.3 (Aug. 2018). ISSN: 0730-0301. DOI: 10.1145/3182161. URL: https://doi.org/10.1145/3182161.

[38] Li Feng, Fen Wang, Hongjie Luo, and Boxin Qiu. "Review of recent advancements in the biomimicry of structural colors." In: *Dyes and Pigments* 210 (2023), p. 111019. ISSN: 0143-7208. DOI: https://doi.org/10.1016/j.dyepig.2022.111019. URL: https://www.sciencedirect.com/science/article/pii/S014372082200941X.

[39] Michael Fischer and Tobias Ritschel. "ZeroGrads: Learning Local Surrogates for Non-Differentiable Graphics." In: *ACM Trans. Graph.* 43.4 (July 2024). ISSN: 0730-0301. DOI: 10.1145/3658173. URL: https://doi.org/10.1145/3658173.

[40] Pascal Freyer and Doekele G. Stavenga. "Biophotonics of diversely coloured peacock tail feathers." In: *Faraday Discuss.* 223 (0 2020), pp. 49–62. DOI: 10.1039/D0FD00033G. URL: http://dx.doi.org/10.1039/D0FD00033G.

[41] Pascal Freyer, Bodo D Wilts, and Doekele G Stavenga. "Reflections on iridescent neck and breast feathers of the peacock, Pavo cristatus." In: *Journal of the Royal Society Interface Focus* 9.1 (2019), p. 20180043.

[42] Jeppe Revall Frisvad, Niels Jørgen Christensen, and Henrik Wann Jensen. "Computing the Scattering Properties of Participating Media Using Lorenz-Mie Theory." In: *ACM Transactions on Graphics* 26.3 (July 2007), 60:1–60:10. DOI: 10.1145/1275808.1276452.

[43] Jeppe Revall Frisvad, Soeren A Jensen, Jonas Skovlund Madsen, António Correia, Li Yang, Søren Kimmer Schou Gregersen, Youri Meuret, and P-E Hansen. "Survey of models for acquiring the optical properties of translucent materials." In: *Computer Graphics Forum* 39.2 (2020), pp. 729–755.

[44] Luis E. Gamboa, Adrien Gruson, and Derek Nowrouzezahrai. "An efficient transport estimator for complex layered materials." In: *Computer Graphics Forum* 39.2 (2020), pp. 363–371. DOI: 10.1111/cgf.13936.

[45] Iliyan Georgiev et al. "Arnold: A Brute-Force Production Path Tracer." In: *ACM Trans. Graph.* 37.3 (Aug. 2018). ISSN: 0730-0301. DOI: 10.1145/3182160. URL: https://doi.org/10.1145/3182160.

[46] Ioannis Gkioulekas, Bei Xiao, Shuang Zhao, Edward H. Adelson, Todd Zickler, and Kavita Bala. "Understanding the role of phase function in translucent appearance." In: *ACM Trans. Graph.* 32.5 (2013). DOI: 10.1145/2516971.2516972.

[47] Jay S. Gondek, Gary W. Meyer, and Jonathan G. Newman. "Wavelength Dependent Reflectance Functions." In: *Proceedings of the 21st Annual Conference on Computer Graphics and Interactive Techniques*. SIGGRAPH '94. New York, NY, USA: Association for Computing Machinery, 1994, 213–220. ISBN: 0897916670. DOI: 10.1145/192161.192202. URL: https://doi.org/10.1145/192161.192202.

[48] Eugenia Guerra, Maria Celeiro, J. Pablo Lamas, Maria Llompart, and Carmen Garcia-Jares. "Determination of dyes in cosmetic products by micro-matrix solid phase dispersion and liquid chromatography coupled to tandem mass spectrometry." In: *Journal of Chromatography A* 1415 (Oct. 2015), pp. 27–37. ISSN: 00219673. DOI: 10.1016/j.chroma.2015.08.054.

[49] Eugenia Guerra, Maria Llompart, and Carmen Garcia-Jares. "Miniaturized matrix solid-phase dispersion followed by liquid chromatography-tandem mass spectrometry for the quantification of synthetic dyes in cosmetics and foodstuffs used or consumed by children." In: *Journal of Chromatography A* 1529 (Dec. 2017), pp. 29–38. ISSN: 00219673. DOI: 10.1016/j.chroma.2017.10.063.

[50] Ibón Guillén, Julio Marco, Diego Gutierrez, Wenzel Jakob, and Adrian Jarabo. "A General Framework for Pearlescent Materials." In: *ACM Transactions on Graphics* 39.6 (2020). DOI: 10.1145/3414685.3417782.

[51] Jie Guo, Zeru Li, Xueyan He, Beibei Wang, Wenbin Li, Yanwen Guo, and Ling-Qi Yan. "MetaLayer: a meta-learned BSDF model for layered materials." In: *ACM Transactions on Graphics* 42.6 (2023), 222:1–222:15. DOI: 10.1145/3618365.

[52] Yu Guo, Miloš Hašan, and Shuang Zhao. "Position-Free Monte Carlo Simulation for Arbitrary Layered BSDFs." In: *ACM Trans. Graph.* 37.6 (Dec. 2018). ISSN: 0730-0301. DOI: 10.1145/3272127.3275053. URL: https://doi.org/10.1145/3272127.3275053.

[53] Rasmus Haapaoja and Christoph Genzwürker. "Mesh-driven generation and animation of groomed feathers." In: *ACM SIGGRAPH 2019 Talks*. 2019.

[54] Pat Hanrahan and Wolfgang Krueger. "Reflection from Layered Surfaces Due to Subsurface Scattering." In: *Proceedings of the 20th Annual Conference on Computer Graphics and Interactive Techniques*. SIGGRAPH '93. New York, NY, USA: Association for Computing Machinery, 1993, 165–174. ISBN: 0897916018. DOI: 10.1145/166117.166139. URL: https://doi.org/10.1145/166117.166139.

[55] James Harvey. "Light-Scattering Characteristics Of Optical Surfaces." In: *Proceedings of SPIE - The International Society for Optical Engineering* 107 (July 1976). DOI: 10.1117/12.964594.

[56] Todd Alan Harvey and Kimberly S. Bostwick y Steve Marschner. "Directional reflectance and milli-scale feather morphology of the African Emerald Cuckoo, Chrysococcyx cupreus." In: *Journal of the Royal Society Interface* (2013).

[57] Eric Heitz. "Understanding the Masking-Shadowing Function in Microfacet-Based BRDFs." In: *Journal of Computer Graphics Techniques (JCGT)* 3.2 (June 2014), pp. 48–107. ISSN: 2331-7418. URL: http://jcgt.org/published/0003/02/03/.

[58] Eric Heitz, Jonathan Dupuy, Cyril Crassin, and Carsten Dachsbacher. "The SGGX microflake distribution." In: *ACM Transactions on Graphics* 34 (4 July 2015), 48:1–48:11. ISSN: 0730-0301. DOI: 10.1145/2766988.

[59] Eric Heitz, Johannes Hanika, Eugene d'Eon, and Carsten Dachsbacher. "Multiple-scattering microfacet BSDFs with the Smith model." In: *ACM Transactions on Graphics (TOG)* 35 (2016), pp. 1–14.

[60] Louis G. Henyey and Jesse Leonard Greenstein. "Diffuse radiation in the galaxy." In: *The Astrophysical Journal* 93 (1941), pp. 70–83.

[61] Geoffrey E Hill and Kevin J McGraw. *Bird coloration: function and evolution*. Vol. 2. Harvard University Press, 2006.

[62] Geoffrey E Hill and Kevin J McGraw. *Bird coloration: mechanisms and measurements*. Vol. 1. Harvard University Press, 2006.

[63] Nicolas Holzschuch and Romain Pacanowski. "A Two-Scale Microfacet Reflectance Model Combining Reflection and Diffraction." In: *ACM Trans. Graph.* 36.4 (July 2017). ISSN: 0730-0301. DOI: 10.1145/3072959.3073621.

[64] Cheng-Guo Huang, Tsung-Shian Huang, Wen-Chieh Lin, and Jung-Hong Chuang. "Physically based cosmetic rendering." In: *Computer Animation and Virtual Worlds* 24.3-4 (2013), pp. 275–283. ISSN: 15464261. DOI: 10.1002/cav.1523.

[65] Weizhen Huang, Matthias B Hullin, and Johannes Hanika. "A Microfacet-based Hair Scattering Model." In: *Computer Graphics Forum* 41.4 (2022), pp. 79–91.

[66] Weizhen Huang, Sebastian Merzbach, Clara Callenberg, Doekele Stavenga, and Matthias Hullin. "Rendering Iridescent Rock Dove Neck Feathers." In: *ACM SIGGRAPH 2022 Conference Proceedings*. SIGGRAPH '22. New York, NY, USA: Association for Computing Machinery, 2022. ISBN: 9781450393379. DOI: 10.1145/3528233.3530749. URL: https://doi.org/10.1145/3528233.3530749.

[67] Hendrik Christoffel van de Hulst. *Multiple Light Scattering*. Vol. 3. New York: Academic Press, 1980.

[68] Hendrik Christoffel van de Hulst. *Light Scattering by Small Particles*. Dover Books on Physics. Dover Publications, 1981. ISBN: 9780486642284. URL: https://books.google.es/books?id=6ivW_TgIdjIC.

[69] Branislav Igic, Liliana D'Alba, and Matthew D Shawkey. "Fifty shades of white: how white feather brightness differs among species." In: *The Science of Nature* 105.3 (2018), pp. 1–15.

[70] Jose A Iglesias-Guitian, Carlos Aliaga, Adrian Jarabo, and Diego Gutierrez. "A biophysically-based model of the optical properties of skin aging." In: *Computer Graphics Forum* 34.2 (2015), pp. 45–55.

[71] Piti Irawan and Steve Marschner. "Specular reflection from woven cloth." In: *ACM Trans. Graph.* 31.1 (Feb. 2012). ISSN: 0730-0301. DOI: 10.1145/2077341.2077352. URL: https://doi.org/10.1145/2077341.2077352.

[72] Wenzel Jakob. *https://www.mitsuba-renderer.org/*. 2014.

[73] Wenzel Jakob, Adam Arbree, Jonathan T. Moon, Kavita Bala, and Steve Marschner. "A Radiative Transfer Framework for Rendering Materials with Anisotropic Structure." In: *ACM Trans. Graph.* 29.4 (July 2010). ISSN: 0730-0301. DOI: 10.1145/1778765.1778790. URL: https://doi.org/10.1145/1778765.1778790.

[74] Wenzel Jakob, Miloš Hašan, Ling-Qi Yan, Ravi Ramamoorthi, and Steve Marschner. "Discrete Stochastic Microfacet Models." In: *ACM Transactions on Graphics (Proceedings of SIGGRAPH)* 33.4 (July 2014), 115:1–115:10. DOI: 10.1145/2601097.2601186.

[75] Wenzel Jakob, Sébastien Speierer, Nicolas Roussel, Merlin Nimier-David, Delio Vicini, Tizian Zeltner, Baptiste Nicolet, Miguel Crespo, Vincent Leroy, and Ziyi Zhang. *Mitsuba 3 renderer*. Version 3.0.1. https://mitsuba-renderer.org. 2022.

[76] Wenzel Jakob, Eugene d'Eon, Otto Jakob, and Steve Marschner. "A comprehensive framework for rendering layered materials." In: *ACM Transactions on Graphics* 33.4 (2014), pp. 1–14.

[77] Adrian Jarabo, Carlos Aliaga, and Diego Gutierrez. "A Radiative Transfer Framework for Spatially-Correlated Materials." In: *ACM Trans. Graph.* 37.4 (July 2018). ISSN: 0730-0301. DOI: 10.1145/3197517.3201282. URL: https://doi.org/10.1145/3197517.3201282.

[78] Wojciech Jarosz. "Efficient Monte Carlo Methods for Light Transport in Scattering Media." PhD thesis. UC San Diego, Sept. 2008.

[79] Henrik Wann Jensen. "Global illumination using photon maps." In: *Proceedings of the Eurographics Workshop on Rendering Techniques '96*. Berlin, Heidelberg: Springer-Verlag, 1996, 21–30. ISBN: 3211828834.

[80] Myung-Ok Jeon and Byung-Soo Chang. "Property of silica and fine structure of cosmetic white powders." In: *Applied Microscopy* 42 (2012), pp. 87–93. DOI: 10.9729/AM.2012.42.2.087.

[81] Wentao Jiang, Si Liu, Chen Gao, Jie Cao, Ran He, Jiashi Feng, and Shuicheng Yan. "PSGAN: pose and expression robust spatial-aware GAN for customizable makeup transfer." In: *Computer Vision and Pattern Recognition (CVPR)*. IEEE, 2020, pp. 5194–5202. DOI: 10.1109/CVPR42600.2020.00524.

[82] James T. Kajiya. "The rendering equation." In: *Proceedings of the 13th Annual Conference on Computer Graphics and Interactive Techniques*. SIGGRAPH '86. New York, NY, USA: Association for Computing Machinery, 1986, 143–150. ISBN: 0897911962. DOI: 10.1145/15922.15902. URL: https://doi.org/10.1145/15922.15902.

[83] Apoorv Khattar, Junqui Zhu, Emiliano Padovani, Jean-Marie Aurby, Marc Droske, Ling-Qi Yan, and Zahra Montazeri. "A Multi-scale Yarn Appearance Model with Fiber Details." In: *Computational Visual Media*. 2024.

[84] Pramook Khungurn and Steve Marschner. "Azimuthal Scattering from Elliptical Hair Fibers." In: *ACM Trans. Graph.* 36.2 (Apr. 2017). ISSN: 0730-0301. DOI: 10.1145/2998578. URL: https://doi.org/10.1145/2998578.

[85] S Kinoshita, S Yoshioka, and J Miyazaki. "Physics of structural colors." In: *Reports on Progress in Physics* 71.7 (2008), p. 076401. DOI: 10.1088/0034-4885/71/7/076401. URL: https://dx.doi.org/10.1088/0034-4885/71/7/076401.

[86] Marie-Christin G. Klein and Stanislav N. Gorb. "Epidermis architecture and material properties of the skin of four snake species." In: (2012).

[87] Andrey Krywonos. "Predicting Surface Scatter Using A Linear Systems Formulation Of Non-paraxial Scalar Diffraction." Ph.D. Dissertation. University of Central Florida, 2006.

[88] Eric P. Lafortune and Yves D. Willems. "Bi-directional path tracing." In: *Proc. International Conference on Computational Graphics and Visualization Techniques (Compugraphics '93)*. Dec. 1993.

[89] Dario Lanza, Juan Raúl Padrón-Griffe, Alina Pranovich, Adolfo Muñoz, Jeppe Revall Frisvad, and Adrián Jarabo. "Practical Appearance Model for Foundation Cosmetics." In: *Computer Graphics Forum* 43.4 (2024), e15148. DOI: https://doi.org/10.1111/cgf.15148. eprint: https://onlinelibrary.wiley.com/doi/pdf/10.1111/cgf.15148. URL: https://onlinelibrary.wiley.com/doi/abs/10.1111/cgf.15148.

[90] James Leaning and Damien Fagnou. "Feathers for mystical creatures: creating pegasus for Clash of the Titans." In: *ACM SIGGRAPH 2010 Talks*. 2010.

[91] Chen Li, Kun Zhou, and Stephen Lin. "Simulating makeup through physics-based manipulation of intrinsic image layers." In: *Computer Vision and Pattern Recognition (CVPR)*. 2015, pp. 4621–4629. DOI: 10.1109/CVPR.2015.7299093.

[92] Chen Li, Kun Zhou, Hsiang-Tao Wu, and Stephen Lin. "Physically-based simulation of cosmetics via intrinsic image decomposition with facial priors." In: *IEEE Transactions on Pattern Analysis and Machine Intelligence* 41.6 (2019), pp. 1455–1469. DOI: 10.1109/TPAMI.2018.2832059.

[93] Tingting Li, Ruihe Qian, Chao Dong, Si Liu, Qiong Yan, Wenwu Zhu, and Liang Lin. "BeautyGAN: instance-level facial makeup transfer with deep generative adversarial network." In: *Multimedia (MM '18)*. ACM, 2018, 645—653. DOI: 10.1145/3240508.3240618.

[94] Albert Julius Liu, Zhao Dong, Miloš Hašan, and Steve Marschner. "Simulating the structure and texture of solid wood." In: *ACM Transactions on Graphics* 35.6 (2016), 170:1–170:11. DOI: 10.1145/2980179.2980255.

[95] Si Liu, Wentao Jiang, Chen Gao, Ran He, Jiashi Feng, Bo Li, and Shuicheng Yan. "PSGAN++: robust detail-preserving makeup transfer and removal." In: *IEEE Transactions on Pattern Analysis and Machine Intelligence* 44.11 (2022), pp. 8538–8551. DOI: 10.1109/TPAMI.2021.3083484.

[96] Si Liu, Xinyu Ou, Ruihe Qian, Wei Wang, and Xiaochun Cao. "Makeup like a superstar: deep localized makeup transfer network." In: *International Joint Conference on Artificial Intelligence (IJCAI)*. AAAI Press, 2016, pp. 2568–2575. URL: https://www.ijcai.org/Proceedings/16/Papers/365.pdf.

[97] Louis Lorenz. *Lysbevægelsen i og uden for en af plane Lysbølger belyst Kugle*. na, 1890.

[98] Joakim Löw, Joel Kronander, Anders Ynnerman, and Jonas Unger. "BRDF Models for Accurate and Efficient Rendering of Glossy Surfaces." In: *ACM Trans. Graph.* 31.1 (Feb. 2012). ISSN: 0730-0301. DOI: 10.1145/2077341.2077350.

[99] Simon Lucas, Mickael Ribardiere, Romain Pacanowski, and Pascal Barla. "A Micrograin BSDF Model for the Rendering of Porous Layers." In: *Proceedings of SIGGRAPH Asia 2023*. 2023.

[100] Rafael Maia, Liliana D'Alba, and Matthew D Shawkey. "What makes a feather shine? A nanostructural basis for glossy black colours in feathers." In: *Proceedings of the Royal Society B: Biological Sciences* 278.1714 (2011), pp. 1973–1980.

[101] Rafael Maia, Regina H F Macedo, and Matthew D Shawkey. "Nanostructural self-assembly of iridescent feather barbules through depletion attraction of melanosomes during keratinization." In: *Journal of the Royal Society, Interface* 9.69 (Apr. 2012), 734—743. ISSN: 1742-5689. DOI: 10.1098/rsif.2011.0456. URL: https://europepmc.org/articles/PMC3284138.

[102] Frank J. Maile, Gerhard Pfaff, and Peter Reynders. "Effect pigments—past, present and future." In: *Progress in Organic Coatings* 54.3 (Nov. 2005), pp. 150–163. ISSN: 03009440. DOI: 10.1016/j.porgcoat.2005.07.003.

[103] Stephen R. Marschner, Henrik Wann Jensen, Mike Cammarano, Steve Worley, and Pat Hanrahan. "Light scattering from human hair fibers." In: *ACM Trans. Graph.* 22.3 (July 2003), 780–791. ISSN: 0730-0301. DOI: 10.1145/882262.882345. URL: https://doi.org/10.1145/882262.882345.

[104] Stephen R. Marschner, Stephen H. Westin, Adam Arbree, and Jonathan T. Moon. "Measuring and modeling the appearance of finished wood." In: *ACM Transactions on Graphics* 24.3 (2005), pp. 727–734. DOI: 10.1145/1073204.1073254.

[105] Dakota McCoy, Allison Shultz, Charles Vidoudez, Emma Heide, Jacqueline Dall, Sunia Trauger, and David Haig. "Microstructures amplify carotenoid plumage signals in tanagers." In: *Scientific Reports* 11 (Apr. 2021), p. 8582. DOI: 10.1038/s41598-021-88106-w.

[106] Maria E. McNamara, Patrick J. Orr, Stuart L. Kearns, Luis Alcalá, Pere Anadón, and Enrique Peñalver. "Reconstructing Carotenoid-Based and Structural Coloration in Fossil Skin." In: *Current Biology* 26.8 (2016), pp. 1075–1082. ISSN: 0960-9822. DOI: https://doi.org/10.1016/j.cub.2016.02.038. URL: https://www.sciencedirect.com/science/article/pii/S0960982216301208.

[107] Maria M. Mendes-Pinto, Amy M. LaFountain, Mary Caswell Stoddard, Richard O. Prum, and Harry A. Frank y Bruno Robert. "Variation in carotenoid–protein interaction in bird feathers produces novel plumage coloration." In: (2012).

[108] Johannes Meng, Marios Papas, Ralf Habel, Carsten Dachsbacher, Steve Marschner, Markus Gross, and Wojciech Jarosz. "Multi-Scale Modeling and Rendering of Granular Materials." In: *ACM Transactions on Graphics (Proceedings of SIGGRAPH)* 34.4 (July 2015). DOI: 10/gfzndr.

[109] Stéphane Mérillou, Jean-Michel Dischler, and Djamchid Ghazanfarpour. "A BRDF Postprocess to Integrate Porosity on Rendered Surfaces." In: *IEEE Transactions on Visualization and Computer Graphics* 6.4 (Oct. 2000), 306–318. ISSN: 1077-2626. DOI: 10.1109/2945.895876. URL: https://doi.org/10.1109/2945.895876.

[110] G. Mie. "Beitr age zur Optik tr uber Medien, speziell kolloidaler Metall osungen." In: *Annalen der Physik* 25.3 (1908), 377–445.

[111] Yusuke Moriuchi, Shoji Tominaga, and Takahiko Horiuchi. "Precise Analysis of Spectral Reflectance Properties of Cosmetic Foundation." In: vol. 5575 LNCS. 2009, pp. 138–148. DOI: 10.1007/978-3-642-02230-2_15.

[112] A. Musbach, G. W. Meyer, F. Reitich, and S. H. Oh. "Full Wave Modelling of Light Propagation and Reflection." In: *Computer Graphics Forum* 32.6 (2013), pp. 24–37. DOI: https://doi.org/10.1111/cgf.12012. eprint: https://onlinelibrary.wiley.com/doi/pdf/10.1111/cgf.12012. URL: https://onlinelibrary.wiley.com/doi/abs/10.1111/cgf.12012.

[113] Thomas Müller, Marios Papas, Markus Gross, Wojciech Jarosz, and Jan Novák. "Efficient Rendering of Heterogeneous Polydisperse Granular Media." In: *ACM Transactions on Graphics (Proceedings of SIGGRAPH Asia)* 35.6 (Dec. 2016), 168:1–168:14. DOI: 10/f9cm65.

[114] N.Walsh, J.Dale, K.J. McGraw, M.A. Pointer, and N.I. Mundy. "Candidate genes for carotenoid coloration in vertebrates and their expression profiles in the carotenoid-containing plumage and bill of a wild bird." In: (2011).

[115] Isaac Newton. *Opticks: Or, A Treatise of the Reflexions, Refractions, Inflexions and Colours of Light*. Royal Society, London, 1704.

[116] Tam V. Nguyen and Luoqi Liu. "Smart mirror: intelligent makeup recommendation and synthesis." In: *Multimedia (MM '17)*. ACM, 2017, pp. 1253–1254. DOI: 10.1145/3123266.3127926.

[117] Gunnar A. Niklasson, Sara L. Niklasson, Celina Notfors, Junxin Wang, Maria Strømme, and Cecilia Århammar. *Optics of sunscreen lotions: Preliminary results on scattering and absorption coefficients*. arXiv:2204.13507 [physics.med-ph]. 2022. DOI: 10.48550/arXiv.2204.13507.

[118] Heeso Noh, Seng Fatt Liew, Vinodkumar Saranathan, Simon G. J. Mochrie, Richard O. Prum, Eric R. Dufresne, and Hui Cao. "How Noniridescent Colors Are Generated by Quasi-ordered Structures of Bird Feathers." In: *Advanced Materials* 22.26-27 (2010), pp. 2871–2880. DOI: https://doi.org/10.1002/adma.200903699. eprint: https://onlinelibrary.wiley.com/doi/pdf/10.1002/adma.200903699. URL: https://onlinelibrary.wiley.com/doi/abs/10.1002/adma.200903699.

[119] Jan Novák, Iliyan Georgiev, Johannes Hanika, Jaroslav Křivánek, and Wojciech Jarosz. "Monte Carlo Methods for Physically Based Volume Rendering." In: *ACM SIGGRAPH 2018 Courses*. SIGGRAPH '18. New York, NY, USA: Association for Computing Machinery, 2018. ISBN: 9781450358095. DOI: 10.1145/3214834.3214880. URL: https://doi.org/10.1145/3214834.3214880.

[120] Juan Raúl Padrón-Griffe, Diego Bielsa, Adrián Jarabo, and Adolfo Muñoz. "A Biologically-Inspired Appearance Model for Snake Skin." In: *Spanish Computer Graphics Conference*. 2023.

[121] Juan Raúl Padrón-Griffe, Dario Lanza, Adrián Jarabo, and Adolfo Muñoz. "A Surface-based Appearance Model for Pennaceous Feathers." In: *Computer Graphics Forum* 43.7 (2024), e15235. DOI: https://doi.org/10.1111/cgf.15235. eprint: https://onlinelibrary.wiley.com/doi/pdf/10.1111/cgf.15235. URL: https://onlinelibrary.wiley.com/doi/abs/10.1111/cgf.15235.

[122] Yanhong Pan et al. "The molecular evolution of feathers with direct evidence from fossils." In: *Proceedings of the National Academy of Sciences* 116.8 (2019), pp. 3018–3023.

[123] Marios Papas, Krystle de Mesa, and Henrik Wann Jensen. "A Physically-Based BSDF for Modeling the Appearance of Paper." In: *Computer Graphics Forum* 33.4 (2014), pp. 133–142. DOI: 10.1111/cgf.12420.

[124] Fabio Pellacini, James A Ferwerda, and Donald P Greenberg. "Toward a psychophysically-based light reflection model for image synthesis." In: *Proceedings of SIGGRAPH 2000*. 2000, pp. 55–64.

[125] Matt Pharr, Wenzel Jakob, and Greg Humphreys. *Physically Based Rendering: From Theory to Implementation*. MIT Press, 2023.

[126] Richard O. Prum. "The anatomy and physics of avian structural colours." In: (1999).

[127] R. Riedler, C. Pesme, J. Druzik, M. Gleeson, and E. Pearlstein. "A review of color-producing mechanisms in feathers and their influence on preventive conservation strategies." In: *Journal of the American Institute for Conservation* 53.1 (2014), pp. 44–65.

[128] Iman Sadeghi, Oleg Bisker, Joachim De Deken, and Henrik Wann Jensen. "A Practical Microcylinder Appearance Model for Cloth Rendering." In: *ACM Trans. Graph.* 32.2 (Apr. 2013).

[129] Rohan Sawhney and Keenan Crane. "Monte Carlo geometry processing: a grid-free approach to PDE-based methods on volumetric domains." In: *ACM Trans. Graph.* 39.4 (Aug. 2020). ISSN: 0730-0301. DOI: 10.1145/3386569.3392374. URL: https://doi.org/10.1145/3386569.3392374.

[130] Rohan Sawhney and Bailey Miller. "Monte Carlo Geometry Processing." In: *SGP 2024 Graduate School Courses*. 2024.

[131] Kristina Scherbaum, Tobias Ritschel, Matthias Hullin, Thorsten Thormählen, Volker Blanz, and Hans-Peter Seidel. "Computer-suggested facial makeup." In: *Computer Graphics Forum* 30.2 (2011), pp. 485–492. DOI: 10.1111/j.1467-8659.2011.01874.x.

[132] Christophe Schlick. "An Inexpensive BRDF Model for Physically-based Rendering." In: *Computer Graphics Forum* 13.3 (1994), pp. 233–246. DOI: https://doi.org/10.1111/1467-8659.1330233. eprint: https://onlinelibrary.wiley.com/doi/pdf/10.1111/1467-8659.1330233. URL: https://onlinelibrary.wiley.com/doi/abs/10.1111/1467-8659.1330233.

[133] Matthew D Shawkey and Liliana D'Alba. "Interactions between colour-producing mechanisms and their effects on the integumentary colour palette." In: *Philosophical Transactions of the Royal Society B: Biological Sciences* 372.1724 (2017), p. 20160536.

[134] Peter Shirley, Samuli Laine, David Hart, Matt Pharr, Petrik Clarberg, Eric Haines, Matthias Raab, and David Cline. "Sampling Transformations Zoo." In: *Ray Tracing Gems: High-Quality and Real-Time Rendering with DXR and Other APIs*. Ed. by Eric Haines and Tomas Akenine-Möller. Berkeley, CA: Apress, 2019, pp. 223–246. ISBN: 978-1-4842-4427-2. DOI: 10.1007/978-1-4842-4427-2_16.

[135] B. Smith. "Geometrical shadowing of a random rough surface." In: *IEEE Transactions on Antennas and Propagation* 15.5 (1967), pp. 668–671. DOI: 10.1109/TAP.1967.1138991.

[136] Brian E. Smits and Gary W. Meyer. "Newton's Colors: Simulating Interference Phenomena in Realistic Image Synthesis." In: *Photorealism in Computer Graphics*. Ed. by Kadi Bouatouch and Christian Bouville. Berlin, Heidelberg: Springer Berlin Heidelberg, 1992, pp. 185–194. ISBN: 978-3-662-09287-3. DOI: 10.1007/978-3-662-09287-3_13. URL: https://doi.org/10.1007/978-3-662-09287-3_13.

[137] Stacey. *White Lipped Python Care, Diet, Habitat Setup and More for Beginners*. 2020. URL: https://reptile.guide/white-lipped-python/ (visited on 12/29/2020).

[138] Jos Stam. "Diffraction shaders." In: *Proceedings of the 26th Annual Conference on Computer Graphics and Interactive Techniques*. SIGGRAPH '99. USA: ACM Press/Addison-Wesley Publishing Co., 1999, 101–110. ISBN: 0201485605. DOI: 10.1145/311535.311546. URL: https://doi.org/10.1145/311535.311546.

[139] Jos Stam. "An illumination model for a skin layer bounded by rough surfaces." In: *Rendering Techniques 2001 (EGWR 2001)*. Springer, 2001, pp. 39–52. DOI: 10.1007/978-3-7091-6242-2_4.

[140] Doekele G Stavenga, Hein L Leertouwer, N Justin Marshall, and Daniel Osorio. "Dramatic colour changes in a bird of paradise caused by uniquely structured breast feather barbules." In: *Proceedings of the Royal Society B: Biological Sciences* 278.1715 (2011), pp. 2098–2104.

[141] Doekele G. Stavenga, Jan Tinbergen, Hein L. Leertouwer, and Bodo D. Wilts. "Kingfisher feathers – colouration by pigments, spongy nanostructures and thin films." In: *Journal of Experimental Biology* 214.23 (Dec. 2011), pp. 3960–3967. ISSN: 0022-0949. DOI: 10.1242/jeb.062620. eprint: https://journals.biologists.com/jeb/article-pdf/214/23/3960/1276925/3960.pdf. URL: https://doi.org/10.1242/jeb.062620.

[142] Shlomi Steinberg and Ling-Qi Yan. "A generic framework for physical light transport." In: *ACM Transactions on Graphics (TOG)* 40.4 (2021), pp. 1–20.

[143] L. Streit and W. Heidrich. "A Biologically-Parameterized Feather Model." In: *Computer Graphics Forum* 21.3 (2002), pp. 565–573. DOI: https://doi.org/10.1111/1467-8659.t01-1-00707. eprint: https://onlinelibrary.wiley.com/doi/pdf/10.1111/1467-8659.t01-1-00707. URL: https://onlinelibrary.wiley.com/doi/abs/10.1111/1467-8659.t01-1-00707.

[144] Lisa Marie Streit. "Modelling of Feather Coat Morphogenesis for Computer Graphics." PhD thesis. 2003, pp. 9–24.

[145] Tarah N. Sullivan, Bin Wang, Horacio D. Espinosa, and Marc A. Meyers. "Extreme lightweight structures: avian feathers and bones." In: *Materials Today* 20.7 (2017), pp. 377–391.

[146] Yinlong Sun. "Rendering Biological Iridescences with RGB-Based Renderers." In: *ACM Trans. Graph.* 25.1 (Jan. 2006), 100–129. ISSN: 0730-0301. DOI: 10.1145/1122501.1122506. URL: https://doi.org/10.1145/1122501.1122506.

[147] Zhaoyang Sun, Feng Liu, Wen Liu, Shengwu Xiong, and Wenxuan Liu. "Local facial makeup transfer via disentangled representation." In: *Asian Conference on Computer Vision (ACCV)*. Springer, 2020, pp. 8538–8551. DOI: 10.1007/978-3-030-69538-5_28.

[148] J. Teyssier, S. Saenko, D. van der Marel, and M. Milinkovitch. "Photonic crystals cause active colour change in chameleons." In: *Nature Communications* 6 (2015), p. 6368. DOI: 10.1038/ncomms7368. URL: \\https://www.nature.com/articles/ncomms7368.

[149] Jan Tinbergen, Bodo D. Wilts, and Doekele G. Stavenga. "Spectral tuning of Amazon parrot feather coloration by psittacofulvin pigments and spongy structures." In: *Journal of Experimental Biology* 216.23 (Dec. 2013), pp. 4358–4364. ISSN: 0022-0949. DOI: 10.1242/jeb.091561. eprint: https://journals.biologists.com/jeb/article-pdf/216/23/4358/1878601/4358.pdf. URL: https://doi.org/10.1242/jeb.091561.

[150] Shoji Tominaga and Yusuke Moriuchi. "Principal component analysis-based reflectance analysis/synthesis of cosmetic foundation." In: *Journal of Imaging Science and Technology* 53.6 (2009), pp. 60403–1–60403–8. DOI: 10.2352/J.ImagingSci.Technol.2009.53.6.060403.

[151] Kenneth E Torrance and Ephraim M Sparrow. "Theory for off-specular reflection from roughened surfaces." In: *Josa* 57.9 (1967), pp. 1105–1114.

[152] Loïc Tran, Philippe Lalanne, Benjamin Askenazi, and Kevin Vynck. "Physically based modeling of the colored appearance of complex media for cosmetics." In: *Proceedings of the 33rd IFSCC Congress*. Barcelona, Spain, Sept. 2023.

[153] U.S. Fish and Wildlife Service. *The Feather Atlas*. https://www.fws.gov/lab/featheratlas/.

[154] Eric Veach. *Robust Monte Carlo Methods for Light Transport Simulation*. Vol. 1610. Stanford University PhD thesis, 1997.

[155] Eric Veach and Leonidas J. Guibas. "Metropolis light transport." In: *Proceedings of the 24th Annual Conference on Computer Graphics and Interactive Techniques*. SIGGRAPH '97. USA: ACM Press/Addison-Wesley Publishing Co., 1997, 65–76. ISBN: 08979-18967. DOI: 10.1145/258734.258775. URL: https://doi.org/10.1145/258734.258775.

[156] Eric Veach and Leonidas Guibas. "Bidirectional estimators for light transport." In: *Photorealistic Rendering Techniques*. Springer, 1995, pp. 145–167. DOI: 10.1007/978-3-642-87825-1_11.

[157] Delio Vicini. "Efficient and Accurate Physically-Based Differentiable Rendering." PhD thesis. École Polytechnique Fédérale de Lausanne (EPFL), 2022.

[158] Bruce Walter, Stephen R. Marschner, Hongsong Li, and Kenneth E. Torrance. "Microfacet models for refraction through rough surfaces." In: *Proceedings of EGSR*. 2007, 195–206.

[159] Zhaoyi Wan, Haoran Chen, Jie An, Wentao Jiang, Cong Yao, and Jiebo Luo. "Facial attribute transformers for precise and robust makeup transfer." In: *Winter Conference on Applications of Computer Vision (WACV)*. IEEE, 2022, pp. 1717–1726. DOI: 10.1109/WACV51458.2022.00317.

[160] Beibei Wang, Wenhua Jin, Miloš Hašan, and Ling-Qi Yan. "SpongeCake: A Layered Microflake Surface Appearance Model." In: *ACM Trans. Graph.* 42.1 (Sept. 2022). ISSN: 0730-0301. DOI: 10.1145/3546940.

[161] Junxin Wang, Changgang Xu, Annica M. Nilsson, Daniel Luis Abreu Fernandes, and Gunnar A. Niklasson. "A novel phase function describing light scattering of layers containing colloidal nanospheres." In: *Nanoscale* 11.15 (2019), pp. 7404–7413. DOI: 10.1039/C9NR01707K.

[162] Lifeng Wang, Wenle Wang, Julie Dorsey, Xu Yang, Baining Guo, and Heung-Yeung Shum. "Real-time rendering of plant leaves." In: *ACM Trans. Graph.* 24.3 (July 2005), 712–719. ISSN: 0730-0301. DOI: 10.1145/1073204.1073252. URL: https://doi.org/10.1145/1073204.1073252.

[163] Gregory J Ward. "Measuring and modeling anisotropic reflection." In: *Proceedings of SIGGRAPH '92*. ACM, 1992, pp. 265–272. DOI: 10.1145/133994.134078.

[164] Eliza Wargala, Martyna Sławska, Agnieszka Zalewska, and Magdalena Toporowska. "Health effects of dyes, minerals, and vitamins used in cosmetics." In: *Women* 1.4 (2021). DOI: 10.3390/women1040020.

[165] Ian Watts. "Red ochre, body painting, and language: interpreting the Blombos ochre." In: *The cradle of language* 2 (2009), pp. 93–129.

[166] Andrea Weidlich and Alexander Wilkie. "Arbitrarily Layered Micro-Facet Surfaces." In: *Proceedings of the 5th International Conference on Computer Graphics and Interactive Techniques in Australia and Southeast Asia*. GRAPHITE '07. New York, NY, USA: Association for Computing Machinery, 2007, 171–178. ISBN: 9781595939128. DOI: 10.1145/1321261.1321292. URL: https://doi.org/10.1145/1321261.1321292.

[167] Philippe Weier and Laurent Belcour. "Rendering Layered Materials with Anisotropic Interfaces." In: *Journal of Computer Graphics Techniques* 9.2 (June 2020), pp. 37–57. URL: http://jcgt.org/published/0009/02/03/.

[168] Mengqi (Mandy) Xia, Bruce Walter, Eric Michielssen, David Bindel, and Steve Marschner. "A Wave Optics Based Fiber Scattering Model." In: *ACM Trans. Graph.* 39.6 (Nov. 2020). ISSN: 0730-0301. DOI: 10.1145/3414685.3417841. URL: https://doi.org/10.1145/3414685.3417841.

[169] Mengqi Xia, Bruce Walter, Christophe Hery, and Steve Marschner. "Gaussian product sampling for rendering layered materials." In: *Computer Graphics Forum* 39.1 (2020), pp. 420–435. DOI: 10.1111/cgf.13883.

[170] Lin Xu, Yangzhou Du, and Yimin Zhang. "An automatic framework for example-based virtual makeup." In: *International Conference on Image Processing (ICIP)*. IEEE, 2013, pp. 3206–3210. DOI: 10.1109/ICIP.2013.6738660.

[171] Ling-Qi Yan, Miloš Hašan, Bruce Walter, Steve Marschner, and Ravi Ramamoorthi. "Rendering specular microgeometry with wave optics." In: *ACM Transactions on Graphics (TOG)* 37.4 (2018), pp. 1–10.

[172] Ling-Qi Yan, Henrik Wann Jensen, and Ravi Ramamoorthi. "An Efficient and Practical near and Far Field Fur Reflectance Model." In: *ACM Trans. Graph.* 36.4 (2017).

[173] Ling-Qi Yan, Chi-Wei Tseng, Henrik Wann Jensen, and Ravi Ramamoorthi. "Physically-Accurate Fur Reflectance: Modeling, Measurement and Rendering." In: *ACM Trans. Graph.* 34.6 (Oct. 2015). ISSN: 0730-0301. DOI: 10.1145/2816795.2818080. URL: https://doi.org/10.1145/2816795.2818080.

[174] Qixin Yan, Chunle Guo, Jixin Zhao, Yuekun Dai, Chen Change Loy, and Chongyi Li. "BeautyREC: robust, efficient, and component-specific makeup transfer." In: *Computer Vision and Pattern Recognition (CVPR)*. IEEE, 2023, pp. 1102–1110. DOI: 10.1109/CVPRW59228.2023.00117.

[175] Yuchun Yan, Juhyun Lee, Jongin Hong, and Hyeon-Jeong Suk. "Measuring and describing the discoloration of liquid foundation." In: *Color Research and Application* 46.2 (2020), pp. 362–375. DOI: 10.1002/col.22584.

[176] Chenyu Yang, Wanrong He, Yingqing Xu, and Yang Gao. "EleGANt: Exquisite and locally editable GAN for makeup transfer." In: *European Conference on Computer Vision (ECCV)*. Springer, 2022, pp. 737–754.

[177] Xingchao Yang, Takafumi Taketomi, and Yoshihiro Kanamori. "Makeup extraction of 3D representation via illumination-aware image decomposition." In: *Computer Graphics Forum* 42.2 (2023), pp. 293–307. DOI: 10.1111/cgf.14762.

[178] Pochi Yeh. *Optical waves in layered media*. Wiley, 2005. ISBN: 9780471731924.

[179] Mehmet Yenmiş, Yunus Bayrakcı, and Dinçer Ayaz. "Hierarchical microstructure of the scales in grass snake (*Natrix natrix*) and dice snake (*Natrix tessellata*)." In: *Biologia* 77 (2022), pp. 765–774. DOI: 10.1007/s11756-022-01034-6. URL: https://doi.org/10.1007/s11756-022-01034-6.

[180] Kenichiro Yoshida and Natsuko Okiyama. "Estimation of reflectance, transmittance, and absorbance of cosmetic foundation layer on skin using translucency of skin." In: *Opt. Express* 29.24 (Nov. 2021), pp. 40038–40050. DOI: 10.1364/OE.442219.

[181] Shuichi Kinoshita; Shinya Yoshioka. "Structural Colors in Nature The Role of Regularity and Irregularity in the Structure." In: (2005).

[182] Thomas Young. "II. The Bakerian Lecture. On the theory of light and colours." In: *Philosophical Transactions of the Royal Society of London* 92 (1802), pp. 12–48. DOI: 10.1098/rstl.1802.0004. URL: https://royalsocietypublishing.org/doi/abs/10.1098/rstl.1802.0004.

[183] Yunchen Yu, Andrea Weidlich, Bruce Walter, Eugene d'Eon, and Steve Marschner. "Appearance Modeling of Iridescent Feathers with Diverse Nanostructures." In: *ACM Trans. Graph.* 43.6 (Nov. 2024). ISSN: 0730-0301. DOI: 10.1145/3687983. URL: https://doi.org/10.1145/3687983.

[184] Tizian Zeltner and Wenzel Jakob. "The Layer Laboratory: A Calculus for Additive and Subtractive Composition of Anisotropic Surface Reflectance." In: *Transactions on Graphics (Proceedings of SIGGRAPH)* 37.4 (July 2018), 74:1–74:14. DOI: 10.1145/3197517.3201321.

[185] Fucheng Zhang, Stuart Kearns, Patrick Orr, Michael Benton, Zhonghe Zhou, Diane Johnson, Xing Xu, and Xiaolin Wang. "Fossilized melanosomes and the colour of Cretaceous dinosaurs and birds." In: *Nature* 463 (Feb. 2010), pp. 1075–8. DOI: 10.1038/nature08740.

[186] Jiajun Zhang and Takashi Kanai. "Biological Modeling of Feathers by Morphogenesis Simulation." In: *2020 International Conference on Cyberworlds (CW)*. 2020, pp. 63–70. DOI: 10.1109/CW49994.2020.00017.

[187] Shuang Zhao, Wenzel Jakob, Steve Marschner, and Kavita Bala. "Building volumetric appearance models of fabric using micro CT imaging." In: *ACM Transactions on Graphics* 30.4 (2011), 44:1–44:10. DOI: 10.1145/2010324.1964939.

[188] Junqiu Zhu, Adrian Jarabo, Carlos Aliaga, Ling-Qi Yan, and Matt Jen-Yuan Chiang. "A realistic surface-based cloth rendering model." In: *ACM SIGGRAPH 2023 Conference Proceedings*. 2023, 5:1–5:9. DOI: 10.1145/3588432.3591554.

[189] Junqiu Zhu, Sizhe Zhao, Lu Wang, Yanning Xu, and Yan Ling-Qi. "Practical Level-of-Detail Aggregation of Fur Appearance." In: *ACM Transactions on Graphics (Proceedings of SIGGRAPH 2022)* 41.4 (2022).

[190] Junqiu Zhu, Sizhe Zhao, Lu Wang, Yanning Xu, and Ling-Qi Yan. "Practical level-of-detail aggregation of fur appearance." In: *ACM Trans. Graph.* 41.4 (2022).

[191] Arno Zinke and Andreas Weber. "Light Scattering from Filaments." In: *IEEE Transactions on Visualization and Computer Graphics* 13.2 (2007), pp. 342–356. DOI: 10.1109/TVCG.2007.43.

[192] Arno Zinke, Cem Yuksel, Andreas Weber, and John Keyser. "Dual scattering approximation for fast multiple scattering in hair." In: *ACM Trans. Graph.* 27.3 (Aug. 2008), 1–10. ISSN: 0730-0301. DOI: 10.1145/1360612.1360631. URL: https://doi.org/10.1145/1360612.1360631.

[193] Eugene d'Eon. *A Hitchhiker's Guide to Multiple Scattering*. https://eugenedeon.com/hitchhikers. 2016.

[194] Eugene d'Eon. "An analytic BRDF for materials with spherical Lambertian scatterers." In: *Computer Graphics Forum* 40.4 (2021), pp. 153–161. DOI: 10.1111/cgf.14348.

[195] Eugene d'Eon, Guillaume François, Martin Hill, Joe Letteri, and Jean-Marie Aubry. "An Energy-Conserving Hair Reflectance Model." In: *Computer Graphics Forum* 30 (2011).